

# Salinity intrusion and tidal propagation in estuarine channel networks with different channel lengths

An idealised model study using Delft3D



Master Thesis Physical Geography  
Name: Rinse de Swart (3631982)  
Faculty of Geosciences  
Department of Physical Geography  
Supervisor: Dr. Maarten van der Vegt

Final version

30/09/2015



**Universiteit Utrecht**



# Acknowledgements

The idea for doing a master thesis about salt intrusion and tidal propagation in estuarine channel networks originated during the course Morphodynamics of Tidal Systems. Particularly the Matlab exercises and the lectures about tidal propagation intensified my interest into estuarine environments. When it was time to choose a subject for the master thesis, I decided to pursue my still existing interest in estuarine systems and combine this with my strong interest in computer modelling.

As with all major projects, this master thesis could not have been completed without the help of others. I therefore wish to express my thanks to a number of persons. To start with my supervisor Maarten van der Vegt. When I contacted him if it would be possible to do a master thesis under his supervision, he responded immediately and presented a few very interesting subjects to me. I want to thank you your supervision and the many meetings we had, particularly during the research period (September 2014-March 2015). I can still remember many interesting discussions ('Rinse, why are you always so critical?') we had in your office. When I was stuck, you thought of new ideas and tried to help me whenever I was reaching a dead end. I also want to thank you for allowing me to use your office as an additional modelling room, whenever you were absent. Secondly, I would like to thank Frans Buschman for all the work he did during his PhD and allowing me to expand his model from 2D without salt to 3D including salt. Also the many grids you generated and the different grid-generation codes you wrote proved to be very useful. I also would like to thank Maarten Kleinhans for the discussions we had and for inventing the grid generation code that was used by Frans Buschman and myself. Apart from that, Nynke Velinga is thanked for her interest in my research project and the useful suggestions she gave to improve the model calibration. Wim Ridderinkhof is thanked for his help in setting up the Domain Decomposition simulation in Delft3D and the assistance he provided in modifying the existing Delft3D grids. Other members of the coastal research group of the department of physical geography (Anouk, Jantien, Joost, Timothy and Jasper) are thanked for their interest and the nice conversations we had in the coffee corner or in the corridor.

Furthermore, I would like to thank a lot of my study friends. To start with Peter Bartels, who always managed to make me laugh, even when things did not go as planned. I really enjoyed our conversations in the basement of the Zonneveld Wing, where your tilting flume proved to be a source of inspiration for both of us. Furthermore, I thank my other friends, being Florian van der Steen, Lars Killaars, Machteld Caspers, Renske Visser, Koos Bok, Willem-Jan Dirx, Laura Brakenhoff, David Maas, Fionna Heuff and Renée Heijenk for the nice lunch meetings and the gatherings at Thursday evening. Last but not least, I would like to thank my parents for their interest in my research project and for cheering me up whenever I was stuck. Without all your support, this thesis would not have been written.

# Contents

Acknowledgements	I
Contents	II
List of figures	IV
List of tables	VII
List of symbols and units used	VII
1. Abstract	1
2. Introduction	2
2.1 Estuaries in general	2
2.2 Salt intrusion and density gradient	3
2.3 Tidal network	4
2.4 General aim	6
2.5 Thesis outline	6
3. Literature study	7
3.1 Definition and classification of estuaries	7
3.2 Mixing and density-driven circulations	10
3.3 Mixing due to secondary flow	13
3.4 Mixing due to tides	15
3.5 Salt balance	16
3.6 Salt balance models	18
3.7 Salt intrusion in multi-channel estuaries	22
3.8 Objectives of the present study	24
3.9 Methodology	25
4. Model set-up	26
4.1 Model set-up	26
4.2 Model calibration	27
4.3 Sensitivity to turbulence closure models	29
4.4 Finding the right boundary conditions	31
5. Modelling the effect of length differences	34
5.1 Delft3D model results	34
5.2 Harmonic analysis	35
5.3 Salinity distribution and intrusion length	45
5.4 Salt transport	54

6. Discussion	63
6.1 Tidal patterns	63
6.2 Salinity distribution and salt balance	64
6.3 Quantifying salt intrusion length	70
6.4 Model recommendations	72
6.5 Suggestions for further research	73
7. Conclusions	74
8. References	75

## List of figures

Figure	Title	Page
Front	Satellite image of the Berau estuarine channel network in Indonesia (Coastalresearch.nl)	FrontPage
Fig. 2.1	Top and side view of an idealised estuary (modified after Savenije, 2005).	2
Fig. 2.2	Idealised sketch of the vertical variation in salinity in a stratified (a), partially mixed (b) and well-mixed estuary (c) (Savenije, 2012)	3
Fig. 2.3	Conceptual sketch of a tidal network with multiple tidal junctions (Buschman, 2011).	4
Fig. 2.4	Schematic overview of the tidal action in a channel that connects a river to sea (Buschman, 2011)	5
Fig. 3.1	Estuarine classification based on the water balance (Valle-Levinson, 2010)	7
Fig. 3.2	Representation of a tidal wave entering three geometrically different estuaries (Nichols & Biggs, 1985)	8
Fig. 3.3	Estuarine classification based on the vertical salinity structure (modified after Valle-Levinson, 2010).	9
Fig. 3.4	Side-sketch of an ideal partially mixed estuary (MacCready & Geyer, 2010).	12
Fig. 3.5	Overview of the tidal-straining mechanism (Simpson et al. 1990, MacCready & Geyer, 2010).	13
Fig. 3.6	Schematic overview of secondary flow due to flow curvature (Chant, 2010).	14
Fig. 3.7	A demonstration of the importance of differential advection during the flooding tide and its influence on the lateral circulation (MacCready & Geyer, 2010).	14
Fig. 3.8	Sketch of the Stokes drift below a propagating wave (blogs.denison.edu).	15
Fig. 3.9	The dispersion coefficient in the Tay estuary at various distances from the estuary mouth for different river flows (West & Williams, 1972; as published in Dyer, 1997).	17
Fig. 3.10	Computed salinity intrusion length at high water slack for different methods (Savenije, 2005).	19
Fig. 3.11	Computed and measured salt intrusion length for 15 estuaries using the method of Brockway et al. (2005) and Savenije (1993). Published in Savenije (2006).	21
Fig. 3.12	The computed salt intrusion length using the modified predictive model of Savenije (2005), as described by Nguyen & Savenije (2006).	22
Fig. 3.13	Example of the model grid, used in the study by Gong et al. (2012).	24
Fig. 3.14	Top view of the Delft3D grid used by Buschman et al., (2010).	25
Fig. 4.1	Overview of the initial Delft3D grid.	26
Fig. 4.2	An example of wiggles in the water level and depth-averaged flow velocities.	28

Fig. 4.3	Results of water level and depth-averaged flow velocities for simulations with 10 and 25 layers.	28
Fig. 4.4	Salinity profiles in a simulation with 25 layers with the $k-\varepsilon$ and the $k-l$ turbulence closure model.	29
Fig. 4.5	Salinity profiles with the default parameter settings and with a reduced discharge and an increased tidal amplitude.	31
Fig. 4.6	Mean salt intrusion with normal and high horizontal diffusivity.	32
Fig. 4.7	Mean salinity in a domain decomposition simulation in which two equal seas are added to the downstream ends of the two branches.	33
Fig. 5.1	Fitted water level amplitudes for channel 1 at different locations downstream of the tidal junction.	37
Fig. 5.2	Fitted water level amplitudes for channel 2 at different locations downstream of the tidal junction.	37
Fig. 5.3	Difference in $M_2$ water level phase ( $\phi_{\eta M_2}$ ) between channel 1 and channel 2 (in hours) plotted as a function of the distance downstream from the tidal junction.	38
Fig. 5.4	Difference in $M_2$ water level phase ( $\phi_{\eta M_2}$ ) between channel 1 and channel 2 (in hours) at the tidal junction.	38
Fig. 5.5	Cross-sectionally averaged $M_2$ velocity amplitudes ( $U_{M_2}$ ) at various locations downstream of the tidal junction for channel 1.	39
Fig. 5.6	Cross-sectionally averaged $M_2$ velocity amplitudes ( $U_{M_2}$ ) at various locations downstream of the tidal junction for channel 2.	39
Fig. 5.7	Difference in $M_2$ velocity phase ( $\phi_{UM_2}$ ) between channel 1 and channel 2 (in hours) plotted as a function of the distance downstream of the tidal junction.	40
Fig. 5.8	Difference in $M_2$ velocity phase ( $\phi_{UM_2}$ ) between channel 1 and channel 2 (in hours) at the tidal junction.	40
Fig. 5.9	Relative phase difference between $\phi_{UM_2}$ and $\phi_{\eta M_2}$ for channel 1 as a function of different locations downstream from the tidal junction.	41
Fig. 5.10	Relative phase difference between $\phi_{UM_2}$ and $\phi_{\eta M_2}$ for channel 2 as a function of different locations downstream from the tidal junction.	41
Fig. 5.11	Tidally- and cross-sectionally averaged salinity amplitude ( $s_{mean}$ ) at various places downstream of the tidal junction in channel 1.	42
Fig. 5.12	Tidally- and cross-sectionally averaged salinity amplitude ( $s_{mean}$ ) at various places downstream of the tidal junction in channel 2.	42
Fig. 5.13	Cross-sectionally averaged $M_2$ tidal salinity amplitudes ( $s_{M_2}$ ) at various locations downstream of the tidal junction for channel 1.	43
Fig. 5.14	Cross-sectionally averaged $M_2$ tidal salinity amplitudes ( $s_{M_2}$ ) at various locations downstream of the tidal junction for channel 2.	43
Fig. 5.15	$M_2$ salinity phase ( $\phi_{sM_2}$ ) difference between channel 1 and channel 2 (in hours) plotted as a function of the distance downstream of the tidal junction.	44
Fig. 5.16	Calculated salinity phase ( $\phi_{sM_2}$ ) differences (in hours) between channel 1 and channel 2 at the tidal junction.	44
Fig. 5.17	Tidally and cross-sectionally averaged salinity versus the length of channel 1.	45
Fig. 5.18	Intrusion length as a function of the length of channel 1.	46

Fig. 5.19	Contour plot showing the tidally- and width-averaged salinity (psu) for all vertical layers in the section 50 km upstream of the tidal junction.	47
Fig. 5.20	Contour plot showing the tidally- and width-averaged salinity (psu) for all vertical layers in channel 1.	47
Fig. 5.21	Contour plot showing the tidally- and width-averaged salinity (psu) for all vertical layers in channel 2.	48
Fig. 5.22	Stratification parameter $\sigma$ for all simulations in the 50 km section just upstream of the tidal junction.	49
Fig. 5.23	Stratification parameter $\sigma$ for all simulations in channel 1.	49
Fig. 5.24	Stratification parameter $\sigma$ for all simulations in channel 2.	50
Fig. 5.25	Overview of the monitoring cross-sections in the grid.	51
Fig. 5.26	Cross-sectional contour plots of the tidally-averaged salinity $\langle S \rangle$ (top), tidally-averaged along-channel velocity $\langle u \rangle$ (middle) and the $U_{M2}$ amplitude (bottom) for the simulations when channel 1 is 20 km and 50 km long. Cross-section located 4 km upstream of the tidal junction.	52
Fig. 5.27	Cross-sectional contour plots of the tidally-averaged salinity $\langle S \rangle$ (top), tidally-averaged along-channel velocity $\langle u \rangle$ (middle) and the $U_{M2}$ amplitude (bottom) for the simulations when channel 1 is 20 km and 50 km long. Cross-sections located 4 km downstream of the tidal junction.	53
Fig. 5.28	Tidally-averaged, cross-sectional advective salt transport as a function of the length of channel 1	55
Fig. 5.29	Decomposition of the advective salt transport over the cross-section using the method of Díez-Minguito et al. (2013).	57
Fig. 5.30	Tidally-averaged, cross-sectional dispersive salt transports as a function of the length of channel 1.	58
Fig. 5.31	Tidally-averaged, cross-sectional advective freshwater transport as a function of the length of channel 1.	59
Fig. 5.32	Tidally-averaged, cross-sectional dispersive freshwater transport as a function of the length of channel 1.	60
Fig. 5.33	Tidally-averaged, cross-sectional instantaneous discharge as a function of the length of channel 1.	60
Fig. 5.34	Decomposition of the total advective freshwater transport over the cross-section in the terms of Uncles & Lewis (2001).	62
Fig. 6.1	Tidally averaged, cross-sectional advective and dispersive salt transport and the sum of both transports plotted at a few locations just upstream of the tidal junction.	66
Fig. 6.2	The cross-sectionally and tidally-averaged salinity versus the tidal running mean (moving average).	66
Fig. 6.3	Time-derivative of the cross-sectionally and tidally-averaged salinity plotted versus the tidal running mean (moving average).	67
Fig. 6.4	Tidally averaged, cross-sectional advective and dispersive salt transport and the sum of both transports plotted downstream of the tidal junction.	67
Fig. 6.5	Tidally averaged, cross-sectional advective and dispersive freshwater transport and the sum of both transports plotted upstream of the tidal junction.	69



Fig. 6.6	Tidally averaged, cross-sectional advective and dispersive freshwater transport and the sum of both transports plotted downstream of the tidal junction.	69
Fig. 6.7	Combined (weighted mean) intrusion length (computed using Delft3D modelling results and the theories) plotted versus the length of channel 1.	71
Fig. 6.8	The theoretical paired intrusion length (computed using the different theories) plotted versus the computed paired intrusion length (computed using the Delft3D modelling results).	72

## List of tables

Table	Title	Page
Table 4.1	Default parameter settings for the Buschman et al. (2010) setup and the first default parameters of this thesis.	27
Table 4.2	Overview of the first and final default settings of this thesis.	33
Table 5.1	Overview of the most important quantities which are stored in the present Delft3D model setting.	34

## List of symbols and units used

Symbol	Property	Units
$A$	Cross-sectional area	$\text{m}^2$
$A_0$	Cross-sectional area at estuary mouth	$\text{m}^2$
$a$	$e$ -folding length scale for area	$\text{m}$
$B$	Channel width	$\text{m}$
$B_0$	Channel width at estuary mouth	$\text{m}$
$B_1$	Channel width at inflection point	$\text{m}$
$B_{up}$	Channel width in the upstream part of the grid	$\text{m}$
$b$	$e$ -folding length scale for width	$\text{m}$
$c$	Amplitude belonging to the tidal component with angular frequency $\omega$ , used in harmonic analysis for determining total amplitude.	$\text{m} - \text{psu}$ $- \text{m s}^{-1}$
$c_d$	Constant relating mixing length, turbulent kinetic energy and dissipation in the $k-\epsilon$ model	-
$d$	Amplitude belonging to the tidal component with angular frequency $\omega$ , used in harmonic analysis for determining total amplitude.	$\text{m} - \text{psu}$ $- \text{m s}^{-1}$
$E$	Tidal excursion	$\text{m}$
$E_0$	Tidal excursion at the estuary mouth	$\text{m}$
$E_1$	Tidal excursion at the inflection point	$\text{m}$
$f$	Freshwater fraction	-
$g$	Acceleration of gravity	$\text{m s}^{-2}$
$H$	Tidal range	$\text{m}$
$H_0$	Tidal range at estuary mouth	$\text{m}$
$HW$	High water	-

<i>HWS</i>	High water slack	-
<i>h</i>	Flow depth/water depth	m
<i>h<sub>0</sub></i>	Flow depth/water depth at estuary mouth	m
$\langle h \rangle$	Tidally averaged water depth	m
<i>K<sub>x</sub></i>	Coefficient of longitudinal eddy diffusion	m <sup>2</sup> s <sup>-1</sup>
<i>K<sub>y</sub></i>	Coefficient of lateral eddy diffusion	m <sup>2</sup> s <sup>-1</sup>
<i>K<sub>z</sub></i>	Coefficient of vertical eddy diffusion	m <sup>2</sup> s <sup>-1</sup>
<i>k</i>	Kinetic energy	m <sup>2</sup> s <sup>-2</sup>
<i>L</i>	Salt intrusion length	m
<i>L<sub>HWS</sub></i>	Salt intrusion length at high water slack	m
<i>L<sub>e</sub></i>	Length salt can be transported by the exchange flow	m
<i>L<sub>K</sub></i>	Length salt can be transported by diffusion	m
<i>LW</i>	Low water	-
<i>LWS</i>	Low water slack	-
<i>l</i>	Mixing length	m
<i>M<sub>2</sub></i>	Semi-diurnal lunar tidal component	
<i>MEAN</i>	Mean water level	m
<i>N<sub>x</sub></i>	Coefficient of longitudinal eddy viscosity	m <sup>2</sup> s <sup>-1</sup>
<i>N<sub>y</sub></i>	Coefficient of lateral eddy viscosity	m <sup>2</sup> s <sup>-1</sup>
<i>N<sub>z</sub></i>	Coefficient of vertical eddy viscosity	m <sup>2</sup> s <sup>-1</sup>
<i>O</i>	Observed record of tidal data, for example that is taken from a tidal station	m – psu – m s <sup>-1</sup>
<i>Q<sub>cum</sub></i>	Cumulative discharge over the cross-section	m <sup>3</sup>
<i>Q<sub>cum_salt_adv</sub></i>	Cumulative advective transport over the cross-section	psu m <sup>3</sup>
<i>Q<sub>cum_salt_disp</sub></i>	Cumulative dispersive transport over the cross-section	psu m <sup>3</sup>
<i>Q<sub>fresh</sub></i>	Freshwater discharge.	m <sup>3</sup> s <sup>-1</sup>
<i>Q<sub>fresh_adv</sub></i>	Advective freshwater transport over the cross-sectional area.	m <sup>3</sup> s <sup>-1</sup>
<i>Q<sub>fresh_disp</sub></i>	Dispersive freshwater transport over the cross-sectional area.	m <sup>3</sup> s <sup>-1</sup>
<i>Q<sub>river</sub></i>	River discharge	m <sup>3</sup> s <sup>-1</sup>
<i>Q<sub>salt-adv</sub></i>	Advective salt transport over the cross-sectional area	psu m <sup>3</sup> s <sup>-1</sup>
<i>Q<sub>salt-disp</sub></i>	Dispersive salt transport over the cross-sectional area	psu m <sup>3</sup> s <sup>-1</sup>
<i>Q<sub>inst</sub></i>	Instantaneous transport over the cross-sectional area	m <sup>3</sup> s <sup>-1</sup>
<i>q<sub>tot adv</sub></i>	Total flow rate per unit width	m <sup>2</sup> s <sup>-1</sup>
<i>R</i>	Total amplitude that is computed while using harmonic analysis on tidal data	m – m s <sup>-1</sup> – psu
<i>Ri</i>	Gradient Richardson number	-
<i>Ri<sub>e</sub></i>	Estuarine Richardson number	-
<i>r<sub>s</sub></i>	Storage width ratio	-
<i>S</i>	Salinity, subscripts, superscripts etc., the same as for <i>u</i>	psu
<i>S<sub>0</sub></i>	Salinity at sea	psu
<i>s</i>	Tidal salinity amplitude	psu
<i>s<sub>mean</sub></i>	Tidally- and cross-sectionally averaged salinity amplitude	psu
<i>s<sub>M2</sub></i>	<i>M<sub>2</sub></i> tidal salinity amplitude	psu
<i>T</i>	Tidal period	s
<i>t</i>	Time	s
<i>U</i>	Tidal velocity amplitude	m s <sup>-1</sup>
<i>U<sub>0</sub></i>	Tidal velocity amplitude at estuary mouth	m s <sup>-1</sup>
<i>U<sub>1</sub></i>	Tidal velocity amplitude at inflection point	m s <sup>-1</sup>
<i>U<sub>M2</sub></i>	<i>M<sub>2</sub></i> tidal velocity amplitude	m s <sup>-1</sup>
<i>U<sub>sc</sub></i>	Along channel velocity scale	m s <sup>-1</sup>

$u$	Flow velocity in $x$ direction	$\text{m s}^{-1}$
$u_0$	Flow velocity at estuary mouth	$\text{m s}^{-1}$
$u_l$	Flow velocity at inflection point	$\text{m s}^{-1}$
$u'$	Turbulent flow velocity in $x$ direction	$\text{m s}^{-1}$
$\langle u \rangle$	Tidally averaged flow velocity in $x$ direction	$\text{m s}^{-1}$
$\frac{u}{b}$	Width-averaged flow velocity in $x$ direction	$\text{m s}^{-1}$
$\bar{u}$	Depth-averaged flow velocity in $x$ direction	$\text{m s}^{-1}$
$\tilde{u}$	Tidal variation of flow velocity in $x$ direction	$\text{m s}^{-1}$
$u_t$	Turbulent fluctuations in along channel velocity	$\text{m s}^{-1}$
$u_v$	Depth variation of flow velocity in $x$ direction	$\text{m s}^{-1}$
$ u $	Absolute flow velocity in $x$ direction	$\text{m s}^{-1}$
$v$	Flow velocity in $y$ direction, subscripts, superscripts etc., the same as for $u$	$\text{m s}^{-1}$
$w$	Flow velocity in $z$ direction, subscripts, superscripts etc., the same as for $u$	$\text{m s}^{-1}$
$x$	Longitudinal coordinate	$\text{m}$
$x_l$	Location inflection point	$\text{m}$
$y$	Lateral coordinate	$\text{m}$
$z$	Vertical coordinate	$\text{m}$
$\beta$	Coefficient of isohaline contraction	$\text{psu}^{-1}$
$\gamma$	Estuarine tapering factor for channel width (equivalent to the inverse $e$ -folding length scale for area)	$\text{m}^{-1}$
$\delta$	Molecular diffusion coefficient	-
$\varepsilon$	Dissipation in transport equation for turbulent kinetic energy	$\text{m}^2 \text{s}^{-3}$
$\zeta$	Van den Burgh's coefficient	-
$\eta$	Water level, subscripts, superscripts etc., the same as for $u$	$\text{m}$
$\eta_{M2}$	$M_2$ tidal water level	$\text{m}$
$\kappa$	Von Kármán constant	-
$\rho$	Water density	$\text{kg m}^{-3}$
$\rho_{fresh}$	Freshwater density	$\text{kg m}^{-3}$
$\Delta\rho$	Density difference between sea and river water	$\text{kg m}^{-3}$
$\sigma$	Stratification parameter	-
$\varsigma$	Vorticity vector	$\text{s}^{-1}$
$\phi$	Phase of tidal constituent	hours
$\omega$	Angular frequency	$\text{s}^{-1}$

# 1. Abstract

Estuaries are regions that form in the narrow boundary zone between the sea and the river. Consequently, they show a large variety of processes, including river flow, tidal processes and wave action. Many estuaries consist of multiple channels, which are together termed an estuarine channel network. A very important characteristic of estuaries is that salt from the sea often intrudes several tens of kilometres upstream. This is becoming an increasingly large problem, particularly in low-lying, urbanised estuaries. In the past decades, a lot of research has been conducted with regards to salinity intrusion in estuaries. However, these studies mostly focused on single-channel estuaries, whereas many estuaries consist of multiple channels.

This master thesis investigates the effect of different channel lengths on salt intrusion and tidal dynamics in a partially- to well-mixed estuarine channel network. An existing, depth-averaged (2D), Delft3D model is extended to a 10-layer (3D) model and calibrated for the new setup. Using the new model, the effect of different channel lengths on salinity intrusion and tidal propagation in an ideal estuarine channel network is investigated. This is done by using harmonic analysis, extensively analysing salt and tidal dynamics and examining the several transport mechanisms. The results suggest that with increasing length differences, tidal energy from the shorter channel is transferred to the longer channel. This affects the water level amplitudes and water level gradients in the shorter channel, causing the freshwater discharge to be concentrated in the shorter channel. As a result, salt can easily intrude upstream through the longer channel, causing vast quantities of salt to be transported upstream. The larger the length differences, the more pronounced this effect gets. The final result is a drastic increase in salt intrusion length for larger differences in channel length.

Nowadays, many large estuaries around the globe are facing large problems, such as climate change (rising sea level), subsidence and increased salinity intrusion. Currently, more and more attention is given to sustainable management of such estuaries. A key requirement for successful management is a sound understanding of the hydrodynamic processes, such as salinity intrusion and tidal propagation. This study shows that the salinity intrusion and tidal propagation in multi-channel estuaries differ considerably from single-channel estuaries. As many large estuaries around the globe consist of multiple channels, the results of this study have both economic and ecological implications for the management of estuaries. Apart from that, there are also scientific implications as this study contributes to a further understanding of salt, tide and hydrodynamics in multi-channel estuaries.

Keywords: Delft3D, Numerical modelling, Estuary, Estuaries, Estuarine channel network, Multi-channel estuary, Tides, Hydrodynamics, Tidal hydrodynamics, Salt, Salt balance, Salinity intrusion, Intrusion length, Estuarine circulation, Estuarine mixing, Advection, Dispersion, Harmonic analysis.

## 2. Introduction

### 2.1 Estuaries in general

Estuaries are semi-enclosed regions where sea and river-water meet and mix, giving rise to the formation of unique habitats with characteristic flora and fauna. Despite this rather simple statement, over 40 different definitions of estuaries exist (Dyer, 1997). The most accepted definition was introduced by Cameron & Pritchard (1963) and reads: ‘An estuary is a semi-enclosed coastal body of water which has free connection to the open sea and within which sea water is measurably diluted with fresh water derived from land drainage’. Although each estuary is unique in its shape and dynamics, some general characteristics and processes apply to every estuary. An overview of these characteristics is given in Fig. 2.1. Every estuary is characterised by a source of fresh water (often a river, here denoted by  $Q_{fresh}$ ), a width  $B$  that is a function of the  $x$  coordinate, a tidal range (here denoted with  $H$ ) and a flow depth (here denoted by  $h$ ). The tidal wave propagation generates a high water (HW) and low water (LW) envelope of the water level  $\eta$ . The water level in the estuary always stays in between these envelopes, where the mean of the high water and low water envelope is called the mean water level (denoted with MEAN). The tidal excursion  $E$  is the horizontal distance a water particle travels during one complete tidal cycle.

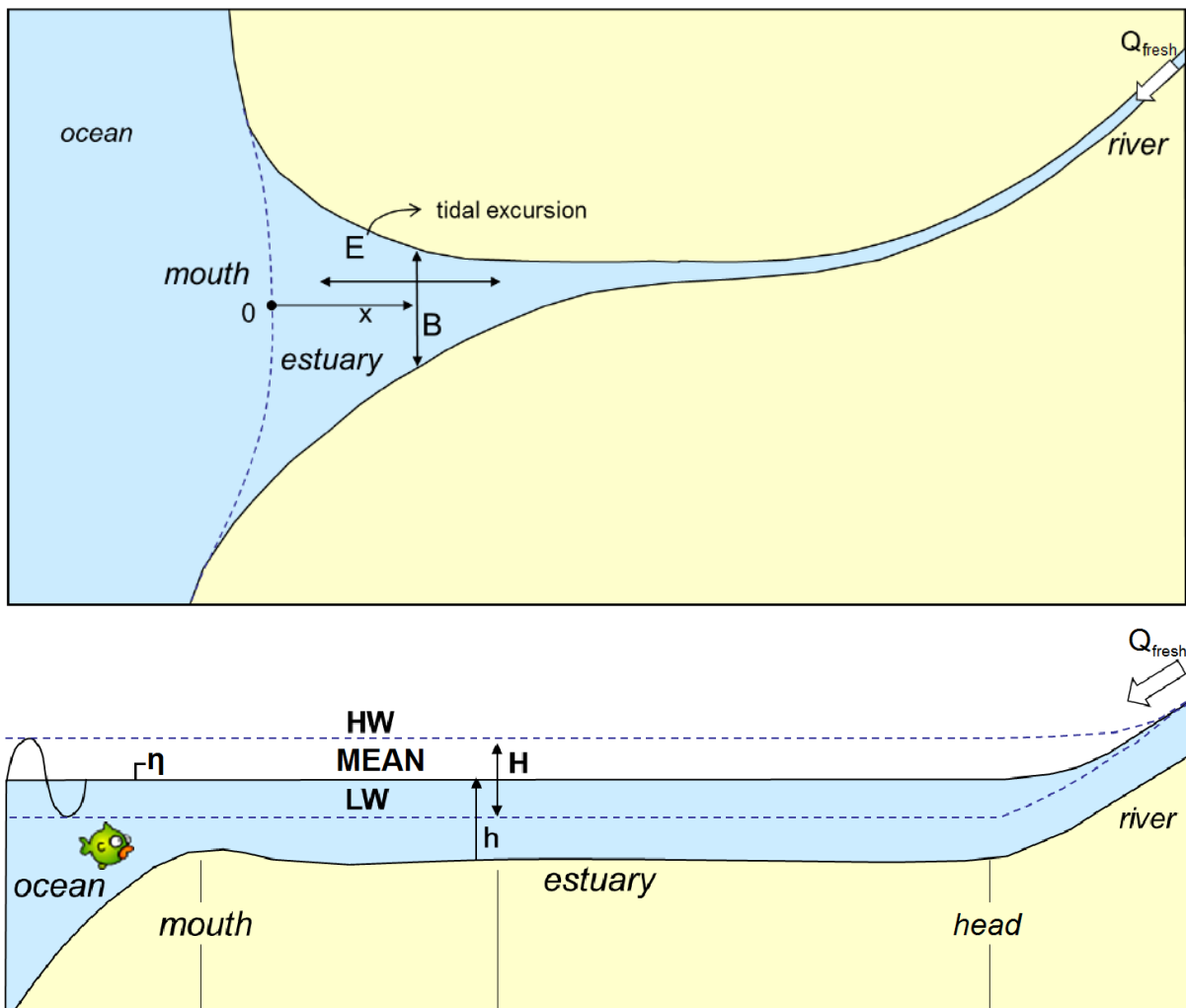


Fig. 2.1: Upper image = Top view of an idealised estuary. Bottom image = Side view of an idealised estuary. The symbols are explained in the text (modified after Savenije, 2005).

Estuaries often comprise of different segments, such as a segment where both tides and river flows are important, a section mostly dominated by tidal flow and a tidal inlet that connects the estuary to the open sea. The landward limit of the estuary (the region where fluvial processes are dominant over wave and tidal processes) is called the estuary head and the lower limit (where wave and tidal processes are dominant) is called the estuary mouth (Dyer, 1997; Savenije, 2005).

## **2.2 Salt intrusion and density gradient**

An important process in estuaries is upstream salt intrusion in the estuary due to tidal action. As a result, mixing of salt water from the sea and freshwater delivered by the river will take place, giving rise to horizontal and vertical gradients in salinity. These gradients are mostly determined by the joint action of river flow and tides in the estuary. Based on the density structure, four different types of estuaries can be distinguished: salt wedge, strongly stratified, partially mixed and well-mixed estuaries (Valle-Levinson, 2010; Savenije, 2012). Salt wedge and strongly stratified estuaries occur when the river discharge is much larger compared to the tidal flow. Logically, a well-mixed estuary forms when the river discharge is small compared to the tidal flow. There is no clear criterion to separate between a partially mixed and a well-mixed estuary, but an estuary is often classified as well-mixed when the stratification (difference in salinity between the upper and lower layer divided by the mean salinity) is below 10 percent (Savenije, 2012). An idealised sketch of the vertical salinity gradient in the different estuaries is given in Fig 2.2. Salt wedge and strongly stratified estuaries are characterised by a sudden increase in salinity over the depth. Partially mixed estuaries are marked by a smooth salinity gradient over the vertical whilst well-mixed estuaries often lack a gradient entirely (Savenije, 2012).

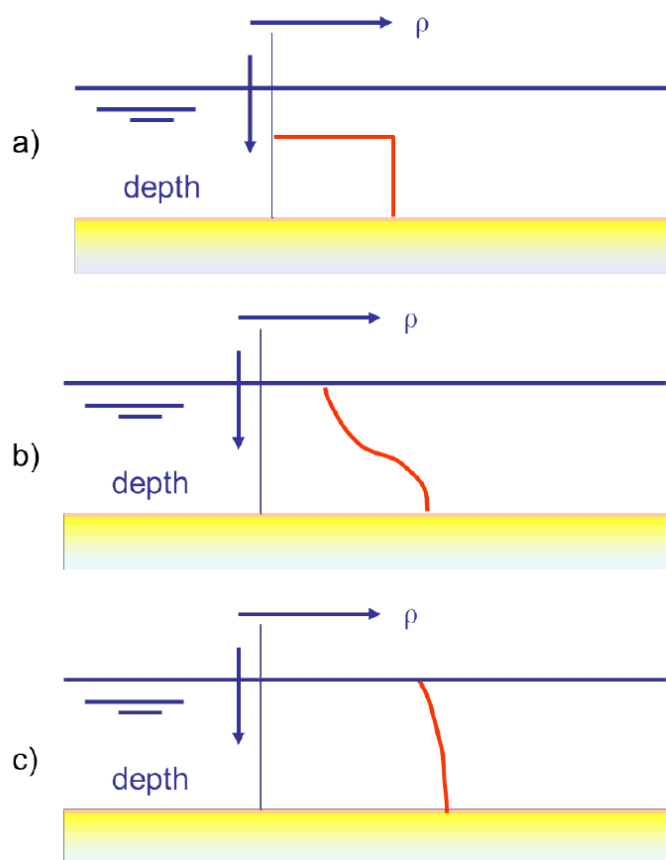


Fig. 2.2: Idealised sketch of the vertical variation in salinity in a stratified (a), partially mixed (b) and well-mixed estuary (c). Density is denoted by  $\rho$  (Savenije, 2012).

The tide that enters an estuary is mostly a mixture of different types of waves. Apart from transporting salt and other substances (such as nutrients) to and from the estuary, tides also mix these substances over the estuary. Salt water intrudes upstream due to the density difference between seawater and freshwater and due to tidal forcing. Knowledge about the salinity patterns in estuaries is important due to a number of reasons. Particularly with low river discharges, salt can intrude a large distance upstream (up to several tens of kilometres). During these times, water availability is low whilst the water requirements are high, as a result of which it is often very difficult to maintain an acceptable water quality. Often, the flora and fauna in estuaries have a certain salinity tolerance and small changes can cause strong alterations in nature development. In addition, freshwater from the river is an important source for drinking water, agricultural purposes and industries. As a result, salt intrusion can have a major impact on flora, fauna and the people that live along the estuary (Savenije, 2012). Therefore, salt intrusion in estuaries has received much attention by the scientific community. This started with the pioneering studies of Pritchard (e.g. 1952a, 1955) in the Chesapeake Bay, focussing on the many processes that influence the salt balance in estuaries. In later years, this became the main focus of lots of other scientists, leading to major breakthroughs in our understanding of salinity dynamics in estuaries. As a result, new scientific models were developed and existing models were refined. A good overview of estuarine studies in the past decades is given in the books by Dyer (1997), Savenije (2005; 2012), Prandle (2009) and Valle-Levison (2010).

### **2.3 Tidal network**

Most of the existing studies focus on single channel estuaries in which there is only one source of freshwater at the head and one connection to sea. However, many estuaries consist of a dense tidal network with a large number of tidal channels and corresponding tidal junctions. These systems have multiple connections to the sea and the freshwater can take several pathways from the river to the sea (Fig. 2.3). Tidal junctions play a critical role in the distribution of freshwater over the network. When compared to bifurcations and confluences found in river networks, the processes at tidal junctions are much more complex because flow is bidirectional and density differences are important. This means that apart from river discharge, tides and salt also have to be taken into account. As a result, the distribution of water and salt at tidal junctions depends on both spatial and temporal changes in flow velocity, stratification induced by salinity differences and the related salt advection (Buschman, 2011).

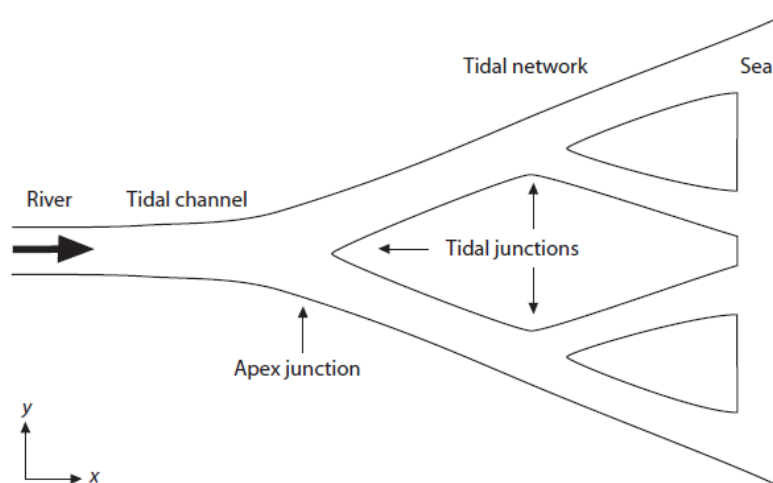


Fig. 2.3: Conceptual sketch of a tidal network with multiple tidal junctions (Buschman, 2011).

In estuarine channel networks, the tide can propagate a large distance upstream. Fig. 2.4 provides an overview of the different sections that can be distinguished. As soon as the daily variation in water level is larger than zero, the channel is called a tidal channel. Seaward of the point where there is no daily variation in water level (tidal rise limit), the water level is affected by the tidal action, but the flow is still directed seaward at all times. Somewhat further downstream, bidirectional flow patterns start to emerge seaward of the flood limit. Downstream of the flood limit, the water flows upstream during a part of the tidal cycle. Water level and flow variation within the same tidal period is called intratidal and variations averaged over the dominant tidal period are termed subtidal. The tidal channel can be subdivided in a tidal river and an estuary. The difference is that a tidal river contains fresh water at all times, whilst an estuary is characterised by a mixture of fresh and salt water. Tidal rivers and estuaries have often developed within a coastal plain, when alluvial channels cut into the flat coastal plain. The topography of these alluvial channels is mostly a funnel-shape, in which the width increases exponentially downstream and the depth is more or less constant.

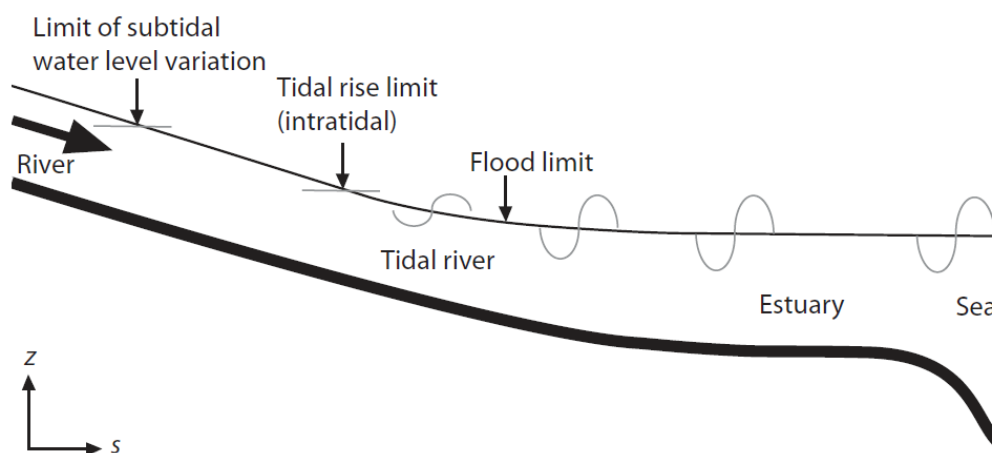


Fig. 2.4: Schematic overview of the tidal action in a channel that connects a river to sea (Buschman, 2011).

Previous studies have shown that flow and sediment division at river junctions is a function of the channel dimensions, the water level gradient and the bottom roughness in each channel (Kleinhans et al., 2013; Wang et al., 1995). In recent years, extensive research projects have been carried on the distribution of both flow and sediment at tidal junctions in Indonesian estuaries. Buschman et al. (2010) constructed a simple hydrodynamic model in Delft3D, which was to some extent related to the Berau Delta in Indonesia. This model comprised of a river channel that splits in two equivalent tidal channels that both end at sea. This model was used to gain understanding about fundamental mechanisms that determine subtidal flow division at estuarine channel junctions. By applying different values in one of the two channels for depth, length,  $e$ -folding length scale (the downstream exponential increase in channel width) and hydraulic roughness, the effect of these four parameters on the subtidal flow division was studied. It was found that in the situation with river flow and tides, varying the depth, length, and  $e$ -folding length scale led to the tide increasing the inequality in subtidal flow division at the tidal junction. On the contrary, the tides reduce the inequality in river flow division when the hydraulic roughness was varied. The study by Sassi et al. (2011) investigated subtidal flow division for the Indonesian Mahakam Delta. They concluded that close to the delta apex, subtidal flow division is hardly affected by tides but that the tidal effect becomes more pronounced closer towards the sea. Generally speaking, tidal action hampers the discharge division that would normally occur in the case with only river flow.



## **2.4 General aim**

Both the study of Buschman et al. (2010) and Sassi et al. (2011) showed that tides cannot be neglected in tidal networks, since they have a distinct effect on the river discharge distribution at bifurcations. However, both studies did not include the effects of density differences induced by the mixing of fresh and saline water. Taking this effect into account is important since the density differences will also affect the distribution of freshwater over the various channels. Therefore, the main aim of this master thesis is to investigate salt and tidal dynamics and the related processes in an estuarine channel network. This study will be limited to well-mixed conditions, as this simplifies the dynamics and salt intrusion is largest during these conditions. The focus will be on modelling salt water intrusion in an estuarine channel network using the model set-up of Buschman et al. (2010). In this study, the length of one of the seaward channels will be varied to study the effect of length differences on salinity intrusion and tidal propagation in an estuarine channel network. Special attention will be paid on the salt and tidal dynamics at tidal junctions, where model simulations can help to elucidate the 3-D flow and salt transport at these junctions.

## **2.5 Thesis outline**

This master thesis starts with a literature review that provides an overview on mixing, tides and salinity intrusion in estuaries (Chapter 3). To get a good overview of estuaries in general, the different estuarine classification schemes will be briefly discussed at first. After that, attention is paid to the flow patterns and mixing processes in estuaries. Next, the salt balance and different models that solve this balance will be discussed. Finally, the main research questions and methodology of the research project are explained. Chapter 4 treats the modifications that were made to the existing Delft3D model. It also describes the model settings and provides a motivation for the choice of many parameter settings. Finally, the different model runs that have been conducted are described briefly. The results of the model runs are described in Chapter 5, focussing on tidal characteristics (using harmonic analysis), salt distribution and the different transport terms. Chapter 6 (Discussion) compares the model results of this study with the results of previous research and provides possible explanations for some remarkable results. Lastly, the most important outcomes of this study are listed in Chapter 7 (Conclusions).

### 3. Literature study

#### 3.1 Definition and classification of estuaries

Estuaries are mostly described as a semi-enclosed area where both fresh and salt water strongly interact. Despite this plain description, many different definitions have been introduced (Dyer, 1997). As described in the introduction, the most common definition was established by Cameron & Pritchard (1963). Their definition reads: ‘an estuary is (a) a semi-enclosed and coastal body of water, (b) with free communication to the ocean, and (c) within which ocean water is diluted by freshwater derived from land.’

Estuaries exist in many different appearances, which is a result of large differences in tidal patterns, freshwater discharge and topography. Apart from these factors, salinity intrusion and the corresponding mixing between fresh and salt water also cause variation in estuarine dynamics. In order to distinguish between the many different types of estuaries, they are often classified based on certain characteristics. As a result, many different classification schemes have been developed in the past 60 years. One of the first classification schemes was derived by Pritchard (1952a), and only distinguished between so called positive and negative estuaries (Fig. 3.1).

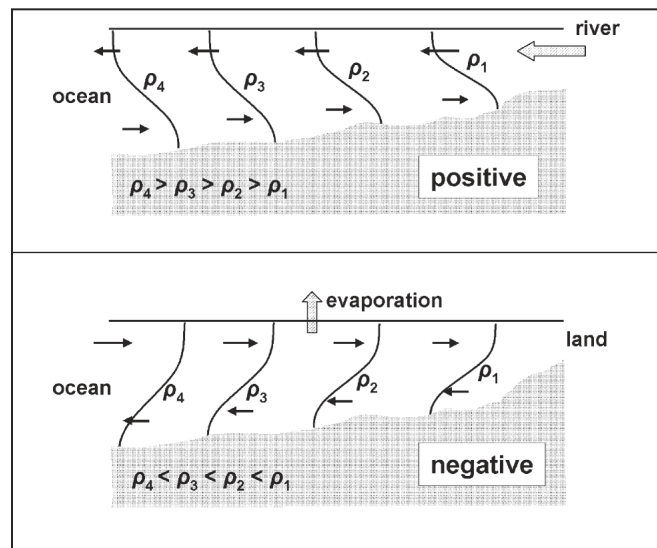


Fig. 3.1: Estuarine classification based on the water balance (Valle-Levinson, 2010). The arrows denote the average estuarine inflow and outflow whilst  $\rho$  indicates density.

In this scheme, a positive estuary is an estuary in which the fresh water inflow and precipitation input is larger than the evaporation output. The freshwater flow creates a longitudinal density gradient, which in turn drives a net volume flow towards the ocean. This is indicated by a stronger outflow near the surface than the inflow near the bottom (Valle-Levinson, 2010). The circulation that develops due to the addition of freshwater to the basin is referred to as the estuarine circulation. Salinity in a positive estuary is much lower compared to the sea (Dyer, 1997; Valle-Levinson, 2010). Negative estuaries are mostly found in dry regions, where the evaporation exceeds the input by precipitation and river flow. As a result, the longitudinal density gradient is the opposite of that in positive estuaries. This means that the water density increases in the landward direction. Negative estuaries show a stronger inflow at the surface than the outflow near the bottom (Dyer, 1997; Valle-Levinson, 2010).

The focus of this thesis is on positive estuaries. However, the appearance of these systems widely differs and depends on tidal action, freshwater discharge and geometry. Based on tidal range, estuaries have been subdivided in four regimes (Davies, 1964): microtidal (tidal range  $\leq 2$  m), mesotidal ( $2 \text{ m} < \text{tidal range} \leq 4$  m), macrotidal ( $4 \text{ m} < \text{tidal range} \leq 6$  m) and hypertidal (tidal range  $> 6$  m). Estuaries with a high tidal range are often characterised by a large tidal prism (the volume of water leaving an estuary at ebb tide). However, this is not always the case since the geometry of the estuary also plays an important role. When the tidal wave enters an estuary, it will interact with the estuarine morphology, resulting in deformation of the tidal wave. As the estuary width decreases and the friction effect is overcompensated by the convergence of energy, the tidal wave will be compressed and the tidal range will increase. Friction will play a major role in shallow water, resulting in a lowering of the tidal range. Nichols & Biggs (1985) distinguished three different estuarine conditions based on the relative importance of convergence and friction in an estuary. These estuary regimes have been classified as hypersynchronous, synchronous and hyposynchronous estuaries (Fig. 3.2).

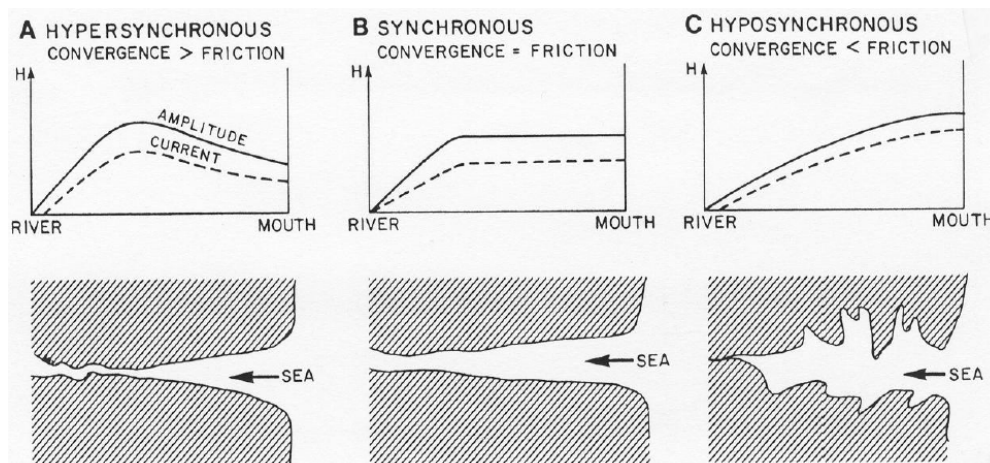


Fig. 3.2: Representation of a tidal wave entering three geometrically different estuaries, thereby showing the modification of the tidal range and current velocity amplitude (Nichols & Biggs, 1985).

Hypersynchronous estuaries are characterised by a strong convergence that exceeds friction. The result is that the tidal range and tidal currents become larger towards the head of the estuary until the convergence effect ceases and friction becomes dominant. This takes place in the riverine section and as a result the tidal amplitude and current eventually reduce. Synchronous estuaries are characterised by a balance between friction and convergence, leading to a constant tidal range in the estuary which only decreases in the riverine section. In hyposynchronous estuaries, the effect of friction on tidal range is large compared to channel convergence. The result is that as soon as the tide enters the estuary, the amplitude decreases. Such estuaries typically consist of a narrow mouth (with high flow velocities) and a wide estuary where the water effectively spreads out (Dyer, 1997).

Since mixing plays an important role in estuaries, a classification scheme based on the stratification and patterns of salinity distribution within an estuary has also been developed (Pritchard, 1955; Cameron & Pritchard, 1963). This scheme separates between highly stratified, partially mixed and well-mixed estuaries (Fig. 3.3). This classification scheme is based on the competition between mixing due to tidal forcing and buoyancy input due to river discharge (Valle-Levinson, 2010). The mixing due to tidal forcing is proportional to the tidal prism. Microtidal conditions combined with a large river discharge result in salt wedge or highly stratified estuaries. These estuaries are characterised by two distinct layers. The upper

water layer consists of fresh water and the lower layer is saline. The fresh water is situated on top because fresh water is less dense than salt water. The interface between fresh and salt water (called the halocline), is horizontal in this case and extends up the estuary as a level surface. Due to friction (in the form of eddy viscosity), a shear will develop in the fluid flow near the interface, creating friction both on the fresh water layer and the salt wedge (Dyer, 1997). When the shear gets large enough, waves will form that break on the interface between fresh and salt water. This causes mixing of fresh and salt water in the water layer at the surface, which is also called entrainment (Dyer, 1997). Highly stratified conditions are often found in estuaries with large freshwater discharges and weak tidal forcing (Valle-Levinson, 2010). Since the focus of this thesis is on partially mixed to well-mixed conditions, the stratified conditions will not be further treated.

A partially-mixed estuary develops due to more intense mixing of fresh and salt water. As a result, the salinity structure of a partially-mixed estuary differs substantially from that of highly stratified and salt wedge estuaries. Near the bottom, a horizontal salinity gradient is present. The transition from salt to fresh water occurs gradually, in contrast to the salt wedge estuary where a sudden transition exists between saline and fresh water. This means that there is a large section in the central part of the estuary where the horizontal salinity gradient decreases linearly in the landward direction. Also the vertical salinity profile does not change much along the estuary. Around mid-depth, the salinity gradient is mostly high, whilst the surface and bottom layers are more or less homogeneous (Dyer, 1997). Partially-mixed estuaries are found in areas with weak to moderate freshwater discharges, a large tidal prism and are mostly mesotidal (Dyer, 1997; Valle-Levinson, 2010). When keeping the river flow and tidal range constant, but increasing the width of the estuary, the ratio of tidal discharge and freshwater discharge is changed. This acts in a similar way as a relative reduction in river flow. The result will be the formation of a better mixed estuary (Dyer, 1997).

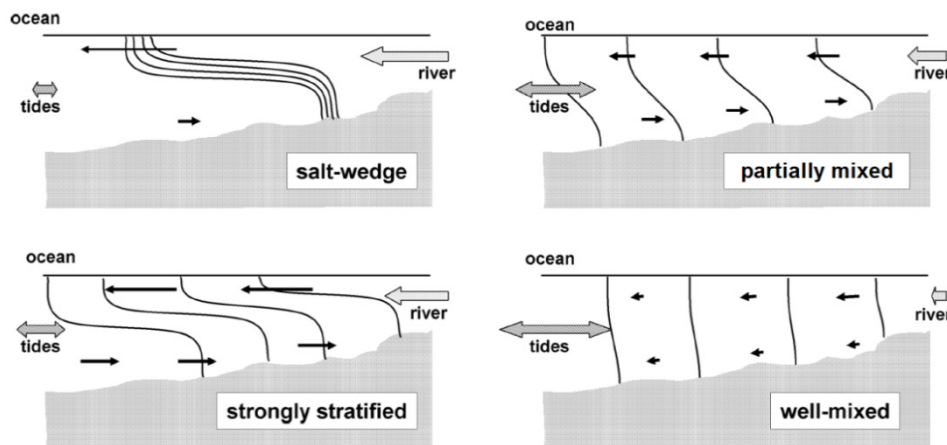


Fig. 3.3: Estuarine classification based on the vertical salinity structure (modified after Valle-Levinson, 2010).

A strong tidal forcing in combination with low river discharge will lead to a completely mixed water column (Dyer, 1997; Valle-Levinson, 2010). The result is a vertically homogeneous or well-mixed estuary. Tidal flow in these estuaries is much larger compared to the river flow, which requires mesotidal or macrotidal conditions (Valle-Levinson, 2010). Apart from that, large velocity shears are often also present in both the vertical and lateral directions. The mean salinity profile in well-mixed estuaries is nearly uniform, meaning that salt only penetrates up to a few tidal excursions (the horizontal distance a water particle travels during one complete tidal cycle). These excursions can be quite large due to the large tidal current.

In some estuaries, different estuarine regimes can be distinguished in each section (Dyer, 1997). Near the estuary head, the tidal amplitude is often lower, meaning that river flow can dominate. As a result, entrainment can take place and a highly stratified structure will be the result. When moving downstream, the tidal velocities and turbulent mixing increase, resulting in a partially mixed structure. Near the mouth of the estuary, the tidal currents are often strong enough to develop well-mixed conditions. Apart from that, width and depth are important factors which influence the flow patterns within an estuary (Pritchard, 1955).

There are also other methods to study the important competition between stratification and mixing. The relative importance of both mechanisms can be analysed with the gradient Richardson number. This number compares the stabilising forces of the density stratification to the destabilising influences of shear in the horizontal velocity and is defined as (Dyer, 1997)

$$Ri = -\frac{g}{\rho} \frac{\partial \rho}{\partial z} / \left( \frac{\partial u}{\partial z} \right)^2, \quad (\text{Eq. 3.1})$$

where  $g$  is the acceleration of gravity ( $\text{m s}^{-2}$ ),  $\rho$  is the water density ( $\text{kg m}^{-3}$ ),  $u$  is the longitudinal velocity ( $\text{m s}^{-1}$ ) and  $z$  is the vertical distance (m). Stratification is stable for  $Ri > 0$  and for  $Ri < 0$  the stratification is unstable. When  $Ri = 0$ , the stratification is neutral and the fluid is unstratified between the two depths. Above a certain stratification value, the turbulence and mixing will be greatly reduced and the flow will get essentially laminar. However, the flow can still be turbulent in the homogeneous layers situated above or below the stratified layer. Stratification will overpower mixing above a  $Ri$  of 0.25. Another type of Richardson number is the so called estuarine Richardson number (Fischer, 1972). This number expresses the ratio of the input of buoyancy per unit width of the channel to the mixing power of the tide. It is defined as (Nguyen, 2008)

$$Ri_e = -\frac{\Delta \rho}{\rho_{fresh}} \frac{g Q_{fresh}}{B U^3}, \quad (\text{Eq. 3.2})$$

where  $\Delta \rho$  is the density difference between seawater and river water ( $\text{kg/m}^3$ ),  $\rho_{fresh}$  is the density of fresh water ( $\text{kg m}^{-3}$ ),  $g$  is the gravitational acceleration ( $\text{m s}^{-2}$ ),  $Q_{fresh}$  is the freshwater discharge ( $\text{m}^3 \text{s}^{-1}$ ),  $B$  is the channel width (m) and  $U$  is the tidal velocity amplitude ( $\text{m s}^{-1}$ ). A high Estuarine Richardson number ( $Ri_e > 0.8$ ) means that the river discharge is more important compared to the tidal forcing. Consequently, a sharp interface exists between fresh and salt water and the estuary will be stratified. A low Estuarine Richardson number ( $Ri_e < 0.08$ ) means that the tidal currents are able to mix the fresh and salt water to such an extent that the estuary becomes well-mixed (Savenije, 2012). For  $0.8 > Ri_e > 0.08$ , the estuary is partially mixed.

### **3.2 Mixing and density-driven circulations**

In this thesis, some important terms are used that are related to the mixing process in estuaries. A short description is given below, following the definitions by Fischer et al. (1979) and Nguyen (2008):

- Turbulent viscosity is the term given to the resistance of a fluid to deformation by shear stress. It relates turbulent stress to velocity shear. Eddy viscosity coefficients express the viscosity of a current.
- Advection is the term given to the substitution of a substance (such as salt) at a certain location, which is due to an imposed current system, as in a river or coastal water.

- Dispersion is the phenomenon that particles or a cloud of contaminants are spread or scattered around due to turbulent mixing. This takes place both in the horizontal and the vertical dimension.
- Molecular diffusion is the phenomenon in which particles are scattered around due to molecular motions, which is often described by Fick's law (described later in this thesis) and the classical diffusion equation.
- Turbulent diffusion is the scattering of particles due to turbulent motion, which has a lot of similarities with molecular diffusion, but is characterised by an 'eddy' diffusion coefficient.
- Mixing is either dispersion or diffusion (as described above).

Mixing of fresh and salt water in estuaries is a result of intern and boundary generated turbulence, which is caused by a combination of winds, tidal currents and freshwater discharge (Pritchard, 1952b; MacCready, 1998; Nguyen, 2008). Since wind-driven mixing does not contribute much to salt dynamics in many estuary (Nguyen, 2008), we will not pay further attention to this. Tides and freshwater discharge are the main drivers that cause large differences in density stratification, circulation patterns and mixing processes. Different types of longitudinal circulation patterns have been recognised in the past, the most common of which is often referred to as the 'classical' estuarine circulation. Although the tidally averaged flow through cross-sections in estuaries is directed seaward due to the river flow (just like in the upper layer), the tidally averaged deeper water layer mostly flows landward. The cause for this is a tidally-averaged pressure gradient that is directed landward in the lower part of the water column. This results in the classical estuarine circulation or exchange flow (Fig. 3.4; MacCready & Geyer, 2010).

An important component of the estuarine circulation is the circulation that is driven by density gradients (Geyer & MacCready, 2014). This density-induced circulation is generated by river flow, resulting in salinity stratification and is therefore called the gravitational or density-driven circulation (Hansen & Rattray, 1966). Mostly, this circulation is accompanied by a vertically stratified salinity profile. However, lateral stratification can also contribute to density-driven mixing, particularly in wider estuaries (Fischer et al., 1979). The gravitational circulation will be largest in the central part of estuaries, as here the strongest salinity gradient exists (McCarthy, 1993; Nguyen, 2008). The gravitational circulation is driven by longitudinal pressure gradient forces which contain both barotropic (surface water slope) and baroclinic (density differences) components. An essential feature of this process is mixing between the different layers, since mixing affects the longitudinal density gradients, which in turn affect the gravitational circulation (Dyer, 1997; MacCready & Geyer, 2010).

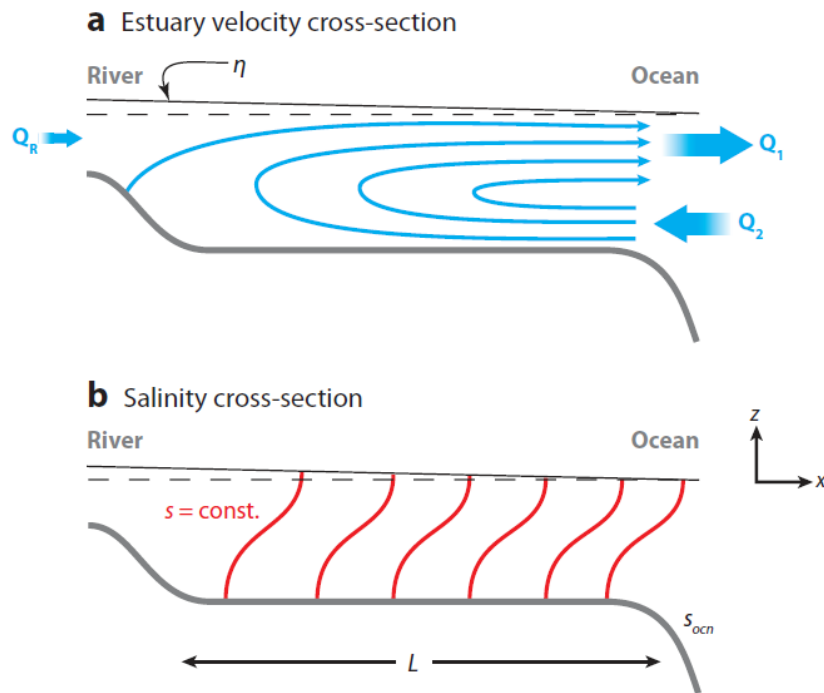


Fig. 3.4: Sketch of an ideal partially mixed estuary (MacCready & Geyer, 2010). Here (a) shows the tidally averaged circulation, with the exchange flow highlighted and (b) shows the isohalines.

During the tide,  $Ri$  can vary strongly, which affects the degree of turbulent mixing and causes asymmetry in mixing. As a result, substantial variation in stratification can take place. The cause for this is tidal straining (Fig. 3.5; Simpson et al., 1990). Due to shear in the velocity profile, the water does not flow at the same speed throughout the water column. The water near the surface travels faster compared to the water near the bed. During ebb, the fresher water is differentially displaced over the salt water layer situated near the bed and as a result the stratification increases. This leads to the situation that the salinity of the surface water decreases faster than the salinity near the bed. As a result, the salinity difference between surface and bed increases. During the flood tide, the stratification will tend to get reduced due to differential movement. Even without the presence of mixing, the entire stratification can be removed as soon as it is high water (convective instability; Nepf & Geyer, 1996). Overall, tidal straining can be a major factor regarding the strength of stratification resulting from buoyancy fresh water input. The ultimate degree of stratification depends on the horizontal density gradient and the tidal excursion length (Dyer, 1997).

In recent years, several studies showed that tidal straining can be an important contributor to estuarine circulation. Jay & Musiak (1994) demonstrated that tidal straining transports more momentum down to the bed during flood compared to ebb. This means that residual transport is generated that supports the estuarine and gravitational circulation. A numerical model study by Burchard & Baumert (1995) showed that excluding tidal straining reduced the estuarine circulation more substantially compared to excluding gravitational circulation. Another striking discovery was made by Burchard & Hetland (2010), who showed that tidal straining is the dominant process that drives the estuarine circulation in estuaries that are periodically stratified. Burchard & Hetland (2010) concluded that without wind straining and residual runoff taken into account, the contribution of tidal straining to the estuarine circulation is nearly twice that of the gravitational circulation.

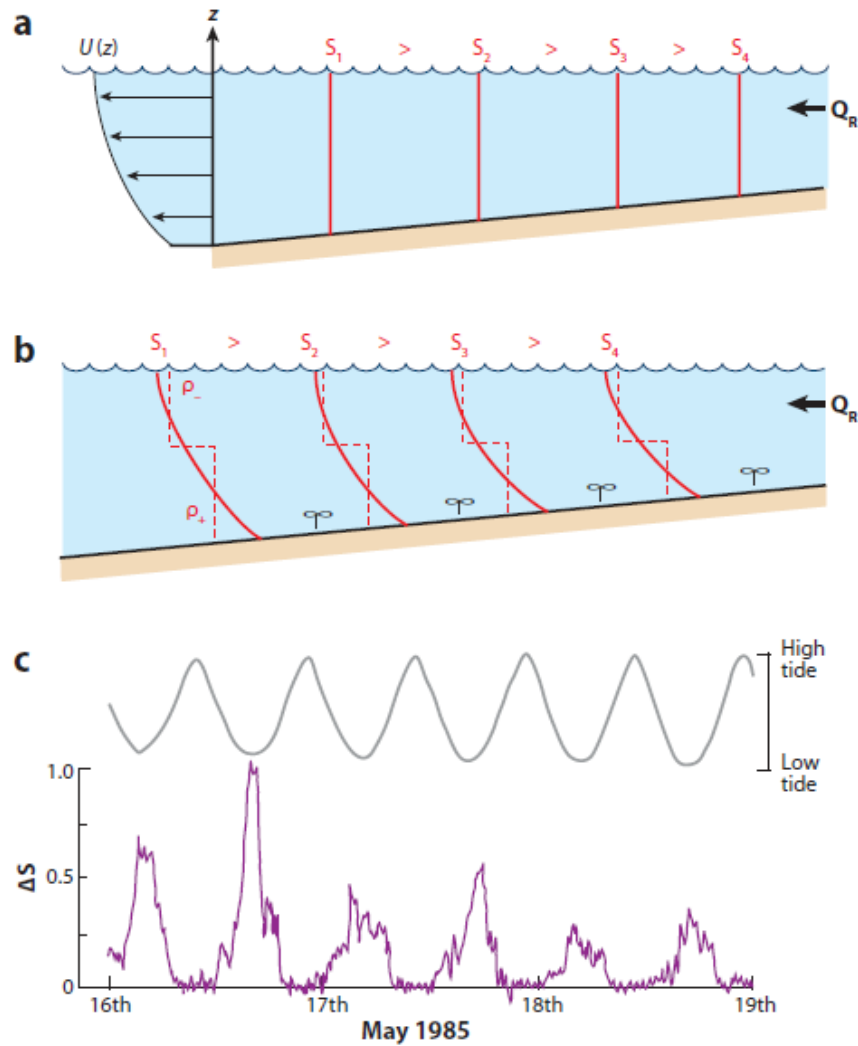


Fig. 3.5: Overview of the tidal straining mechanism (Simpson et al. 1990, MacCready & Geyer, 2010). The upper panel shows well-mixed conditions at the end of the flooding tide and the vertical ebb velocity profile. The second panel shows the salinity contour getting distorted during ebb, with the dashed lines indicating the influence of mixing. The bottom panel indicates the presence of well-mixed and stratified conditions, showing maximum stratification at the end of ebb.

### **3.3 Mixing due to secondary flow**

When water flows through a bend, it will experience a centrifugal force which forces the water to the outside of the bend. This causes a super-elevation of water on the outside of the bend and the formation of secondary flows. However, flow patterns are also affected by changes in cross-sectional area along the estuary. In estuaries, the secondary flow system is often opposite of that seen in rivers. Secondary circulation is caused by many processes, such as Ekman forcing (a dynamic balance between the Coriolis acceleration and friction), transverse baroclinic pressure gradients (also called differential advection) and channel curvature (Chant, 2010). Apart from rivers, where curvature causes helical flow (Kalkwijk & Booij 1986), this mechanism also drives secondary flows in estuaries (MacCready & Geyer, 2010). The way this takes place is conceptually explained in Fig. 3.6.



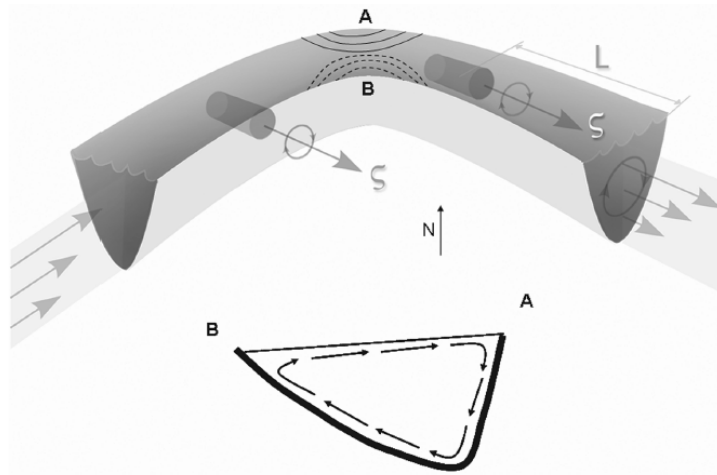


Fig. 3.6: Upper panel: a schematic set-up of secondary flows due to flow curvature. The entering flow is vertically sheared and is characterised by vorticity vector  $\zeta$  that is directed to the south-east. The lines in the channel bend depict sea level, in which elevated levels are depicted by solid lines and lower levels by dashed lines.  $L$  is an illustration of the length scale of the spin-down of secondary flows. Lower panel: cross-sectional structure of secondary flows in and downstream of channel bends (Chant, 2010).

The importance of the lateral or secondary circulation for generating transverse mixing was at first described by Smith (1976). This was the first study that recognised the importance of lateral or secondary circulation for generating transverse density gradients (nowadays known as differential advection; Fig. 3.7). Furthermore, Smith (1976) noted that these gradients induced lateral motion that could mix the transverse density variations (via transverse shear dispersion). The nonlinear interaction between the secondary circulation and the tidal shear flow can also be an important contributor to the estuarine circulation. In some estuaries, the denser water can be advected during the flood tide to the middle of the estuary whilst the less dense water will stay on the sides of the estuary. This lateral density gradient causes a baroclinic circulation which converges in the centre of the channel, resulting in the formation of the so called axial convergence front (yellow dashed line in Fig. 3.7; Nunes & Simpson, 1985).

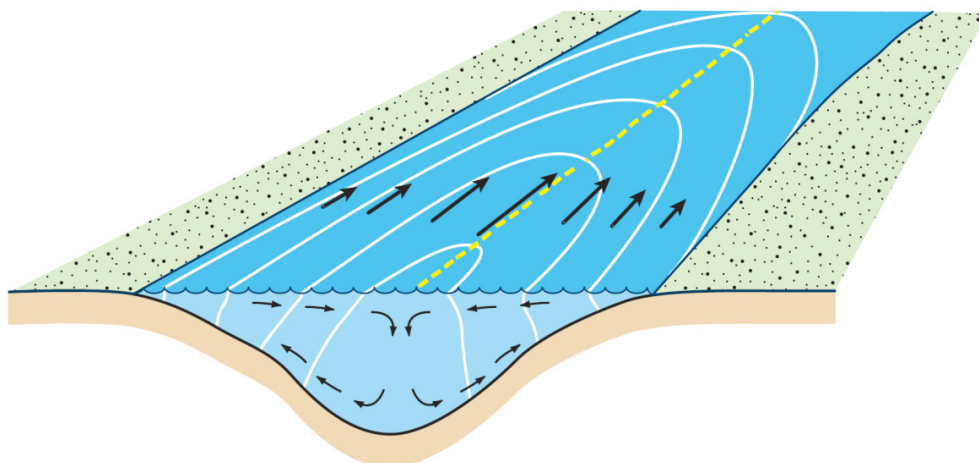


Fig. 3.7: A demonstration of the importance of differential advection during the flooding tide and its influence on the lateral circulation (MacCready & Geyer, 2010). The longshore velocities (black arrows) are stronger in the deep part of the estuary, causing increased advection of higher-salinity water (white contours) over there than on the flanks. The lateral density gradient results in the formation of a lateral baroclinic circulation with counter-rotating circulation cells. Surface convergence in the middle of the estuary forms the axial convergence front.

### 3.4 Mixing due to tides

Tides cause the entire estuary volume to fluctuate with the ebb and flood current. For this, only a small tidal range is required, which results in the development of a partially mixed estuary. The larger the tidal range, the better mixed the estuary will get (for a constant river discharge). An important large-scale mixing mechanism in this respect is ‘tidal pumping’ (Fischer et al., 1979). It is defined as ‘the energy available in the tide that drives steady circulations similar to what would happen if pumps and pipes were installed to move water about in circuits’ (Fischer et al., 1979; Nguyen, 2008). During flood, the current transports salt water landward, whilst during ebb fresh water is transported seaward. Hence, net effect is landward transport of salt. Tidal pumping is important in estuaries with a distinct ebb-flood channel system (Van Veen, 1950), in estuaries with irregular bathymetry (Nguyen, 2008) and near the mouth of a wide estuary (Savenije, 2012). The most striking difference from gravitational circulation is that the tidal pumping mechanism is proportional to the width of the estuary and does not depend on the salinity gradient (Savenije, 2012).

Another mechanism that transports mass upstream is the so called Stokes drift. It develops when the tidal wave in the estuary has a propagating character (zero degrees phase difference between water levels and flow velocities). In that case, a so called Stokes drift (Stokes, 1847) is generated which results in mass transport in the direction of wave propagation (Fig. 3.8). When the estuary has one channel and a closed end, this mass has to come out (otherwise the basin keeps on filling with water). This will generate a mean compensating current that is directed out of the basin. In a tidal network, this is not necessarily the case.

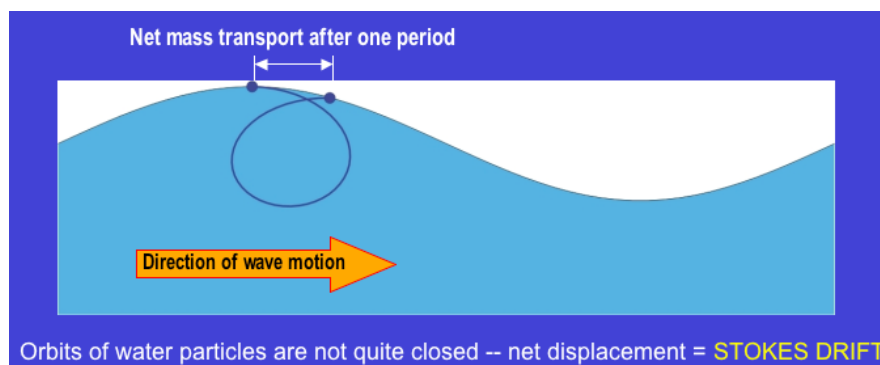


Fig. 3.8: Sketch of the Stokes drift below a propagating wave (blogs.denison.edu).

The amount of energy that is involved in the tidal movements is large, which is mainly dissipated by working against the frictional forces on the bottom. This leads to the formation of turbulent eddies, which cause the mixing of salt water upwards and fresh water downwards. The rate of mixing depends largely on the coefficients of eddy diffusion and eddy viscosity. The process in which fresh and salt water are mixed in estuaries is performed by turbulence processes generated by shear at the sea bed and the halocline. During the tidal cycle, these two processes vary both in timing and intensity, but they also vary over the different estuary types due to changes in stratification and tidal velocities. When  $Ri > 0.25$ , instabilities that are formed at the interface will transform into some kind of ‘cusps’ and entrainment will take place. When  $Ri < 0.25$ , turbulent diffusion instead of entrainment will take place. This process happens mostly with low  $Ri$  and results in the upward movement of water and salt into the overlying flow, as well as downwards into the underlying flow. The net mixing is therefore the sum of these two processes. Moreover, this turbulent mixing is a two-way process which exchanges equal volumes of water between the different layers. Even though there is no net flow of water, salt is still transported upwards and the potential energy of the water column therefore increases (Dyer, 1997).

### 3.5 Salt balance

For an accurate quantification of estuarine characteristics, it is essential to be able to quantify both the water circulation and mixing processes. The method to do this is to determine the salt budget within sections of the estuary. Also for determining the salt intrusion length, which is the distance salt intrudes upstream from the estuary mouth, it is important to determine the salt budget. The salt continuity equation for instantaneous values, valid in conditions without any salt creation reads (Dyer, 1997)

$$\frac{\partial S}{\partial t} = -\frac{\partial(uS)}{\partial x} - \frac{\partial(vS)}{\partial y} - \frac{\partial(wS)}{\partial z} + \delta \left( \frac{\partial^2 S}{\partial x^2} + \frac{\partial^2 S}{\partial y^2} + \frac{\partial^2 S}{\partial z^2} \right), \quad (\text{Eq. 3.3})$$

with  $S$  being the salinity (psu),  $t$  is time (s),  $u$  is the longitudinal velocity ( $\text{m s}^{-1}$ ),  $v$  is the lateral velocity ( $\text{m s}^{-1}$ ),  $w$  is the vertical velocity ( $\text{m s}^{-1}$ ),  $\delta$  is a molecular diffusion coefficient and  $x$ ,  $y$  and  $z$  are the longitudinal, lateral and vertical coordinates respectively. Averaging the left-hand side of Eq. (3.3) over a tidal cycle results in  $\partial\langle S \rangle / \partial t$  because the tidal fluctuation will be zero when averaged over a tidal cycle and this will also be the case for the turbulent salt component (mostly denoted with  $S'$ ). In many analyses, the cross-products of tidal fluctuation are neglected. This means that the salt balance for tidally-averaged cases without taking molecular diffusion into account can be given by (Dyer, 1997)

$$\frac{\partial\langle S \rangle}{\partial t} = -\frac{\partial(\langle u \rangle \langle S \rangle)}{\partial x} - \frac{\partial(\langle v \rangle \langle S \rangle)}{\partial y} - \frac{\partial(\langle w \rangle \langle S \rangle)}{\partial z} - \frac{\partial\langle u' S' \rangle}{\partial x} - \frac{\partial\langle v' S' \rangle}{\partial y} - \frac{\partial\langle w' S' \rangle}{\partial z}, \quad (\text{Eq. 3.4})$$

where the  $\langle \rangle$  denote a tidal average and the  $'$  denotes a short-period turbulent fluctuation. The first three terms on the right-hand side of Eq. 3.4 are the advection terms (salt flux due to mean flow), and the last three terms are the eddy diffusion terms (salt flux caused by short period turbulence). In most cases, the terms on the right-hand side of Eq. 3.4 will be nearly in equilibrium, resulting in a slow change in salt content over time. With steady-state conditions,  $\partial\langle S \rangle / \partial t$  will be zero and the diffusive and advective terms will balance.

As turbulence is difficult to measure (and impossible to model on estuarine scales), it is common to express it in terms that are easier to measure. This can be done by considering turbulent exchanges a gradient process, so that turbulence can be parameterised into so called eddy diffusion coefficients ( $K$ ) and eddy viscosity coefficients ( $N$ ). Their magnitude depends on the flow conditions and they do not have a constant value through time and space. For numerical modelling, the determination or chosen magnitude of these coefficients is an important issue. Rewriting the eddy diffusion terms in Eq. 3.4 leads to (Dyer, 1997)

$$\langle u' S' \rangle = -K_x \frac{\partial\langle S \rangle}{\partial x}, \quad \langle v' S' \rangle = -K_y \frac{\partial\langle S \rangle}{\partial y}, \quad \langle w' S' \rangle = -K_z \frac{\partial\langle S \rangle}{\partial z}, \quad (\text{Eq. 3.5})$$

with  $K_x$ ,  $K_y$  and  $K_z$  successively being the coefficient of longitudinal, lateral and vertical eddy diffusion ( $\text{m}^2 \text{s}^{-1}$ ). Substituting Eq. 3.5 in Eq. 3.4 yields (Dyer, 1997)

$$\frac{\partial\langle S \rangle}{\partial t} = -\frac{\partial(\langle u \rangle \langle S \rangle)}{\partial x} - \frac{\partial(\langle v \rangle \langle S \rangle)}{\partial y} - \frac{\partial(\langle w \rangle \langle S \rangle)}{\partial z} + \frac{\partial}{\partial x} \left( K_x \frac{\partial\langle S \rangle}{\partial x} \right) + \frac{\partial}{\partial y} \left( K_y \frac{\partial\langle S \rangle}{\partial y} \right) + \frac{\partial}{\partial z} \left( K_z \frac{\partial\langle S \rangle}{\partial z} \right). \quad (\text{Eq. 3.6})$$

This is called Fick's equation, which is a classic form of the continuity equation for salt. The eddy diffusion coefficients have the dimensions length squared divided by time. They represent the tidally-averaged mixing conditions and have a different physical meaning

compared to the coefficients that result from averaging over a shorter period. By using the equation of continuity, it is possible to write Eq. 3.6 as (Dyer, 1997)

$$\frac{\partial \langle S \rangle}{\partial t} = \langle u \rangle \frac{\partial \langle S \rangle}{\partial x} + \langle v \rangle \frac{\partial \langle S \rangle}{\partial y} + \langle w \rangle \frac{\partial \langle S \rangle}{\partial z} - \frac{\partial}{\partial x} \left( K_x \frac{\partial \langle S \rangle}{\partial x} \right) - \frac{\partial}{\partial y} \left( K_y \frac{\partial \langle S \rangle}{\partial y} \right) - \frac{\partial}{\partial z} \left( K_z \frac{\partial \langle S \rangle}{\partial z} \right). \quad (\text{Eq. 3.7})$$

This equation can be further simplified when salinities and velocities can be considered uniform in one or two axial directions (Pritchard, 1958). Different terms in Eq. 3.7 will dominate for the different estuarine types, whilst other terms will be negligible. In well-mixed one-dimensional estuaries, the distribution of properties is often considered to be dependent on  $x$  only. In these environments the main balance reduces to (Dyer, 1997)

$$\langle u \rangle \langle S \rangle = K_x \frac{\partial \langle S \rangle}{\partial x}. \quad (\text{Eq. 3.8})$$

This equation states that longitudinal downstream advection of salt on the sectional mean flow will be balanced by upstream horizontal diffusion. The mean sectional velocity is related if  $\langle u \rangle = Q_{fresh}/\langle A \rangle$  (with  $Q_{fresh}$  being the freshwater discharge in  $\text{m}^3 \text{s}^{-1}$  and  $\langle A \rangle$  the mean cross-sectional area in  $\text{m}^2$ ). This means that  $K_x$  can be written as (Dyer, 1997)

$$K_x = Q_{fresh} \langle S \rangle / \langle A \rangle \frac{\partial \langle S \rangle}{\partial x}. \quad (\text{Eq. 3.9})$$

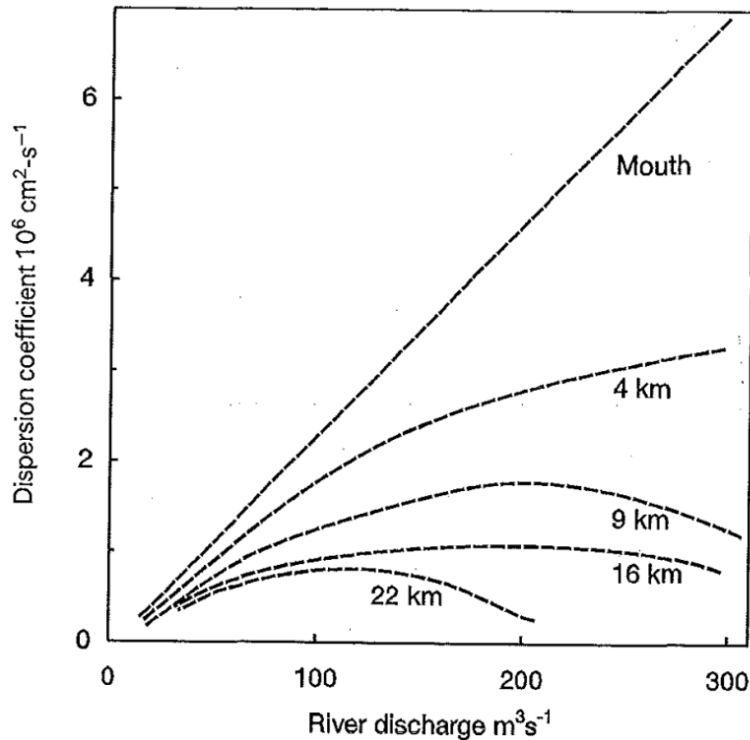


Fig. 3.9: The dispersion coefficient in the Tay estuary at various distances from the estuary mouth for different river flows (West & Williams, 1972; as published in Dyer, 1997).

As a result,  $K_x$  can be calculated at each location in the estuary when river flow, cross-sectional area and salinity distribution along the estuary are known. It is evident from Eq. 3.9 that  $K_x$  increases linearly with river flow. This approach was used in the Scottish Tay estuary by West and Williams (1972) to compare  $K_x$  with river discharge at different locations along the estuary (Fig. 3.9). It is clear that Eq. 3.9 holds for all conditions at the mouth and gives

reasonable results at other locations in the estuary for low river flow conditions. Near the head, Eq. 3.9 only gives reasonable results for very low flows, because the increased river flow forces the stratification downstream. This approach does not account for lateral or vertical variations in the mean flow. The effect of gravitational circulation, lateral processes and asymmetric mixing on salt transport will always show up in a diffusive term, even though it is not caused by a turbulent exchange. Thus, the coefficient is a dispersion coefficient.

### **3.6 Salt balance models**

In order to solve the salt balance equation (Eq. 3.7), the area, discharge, source term (input due to drainage or rainfall), and the diffusion coefficients have to be known (Savenije, 2012). The first three variables can be measured or obtained by solving the equations for mass and momentum conservation. The diffusion coefficients contain all diffusion mechanisms that counteract the advective salt transport. These coefficients are often computed using observed salinity characteristics in a real estuary or using an empirical theory (such as Savenije, 2005). To solve the salt balance equation, two types of models are often used, being steady-state and unsteady-state models. Steady state models are used to solve the salt balance equation for a state of equilibrium in the estuary and have been used extensively in the past (e.g. Van den Burgh, 1972; Savenije, 1993). Unsteady-state models are used for estuaries where a steady state does not occur. By using steady-state models, an empirical model for salinity intrusion in estuaries can be developed. By using such models, it is possible to quantify the salt intrusion length, which is defined as ‘the distance from the estuary mouth to the point where the salinity reaches the river salinity’ (Nguyen, 2008). The way to develop such a model is by calibrating the results of steady-state data to field observations. As a result, these models are often only applicable to the estuary on which the model has been calibrated. A number of such models exist (Van den Burgh, 1972; Rigter, 1973; Fischer, 1974; Van Os and Abraham, 1990; Savenije, 1993; 2005 and Prandle, 2004), which are briefly discussed by Nguyen (2008).

The drawback of all the above-mentioned models is that they were developed for single-channel estuaries. Moreover, the models of Rigter (1973), Fischer (1974) and Van Os and Abraham (1990) assume a constant cross-section whilst in reality this is mostly not the case. Estuaries are very often characterised by an exponential shape, such as  $A = A_0 \exp(-x/a)$  and  $B = B_0 \exp(-x/b)$ , in which  $A_0$  ( $m^2$ ) and  $B_0$  (m) are the area and width at the estuary mouth;  $a$ ,  $b$  are the convergence lengths or  $e$ -folding length scales of area and width (m) and  $x$  (m) is the distance from the estuary mouth. Of the above-mentioned models, only the model of Savenije (1993, 2005) takes into account this exponential shape. The model of Prandle (2004) determines the bathymetry using a power function, but this is not considered a realistic approximation as this kind of estuarine shape is not often observed in nature. The models of McCarthy (1993) and MacCready (2004) also take into account the variability in channel width. A comparison between some of the earlier mentioned models (Van den Burgh, 1972; Rigter, 1973; Fischer, 1974; Van Os and Abraham, 1990; Savenije, 1993; 2005) on 13 estuaries around the globe shows that the model of Savenije (1993, 2005) is by far the most accurate in computing the salinity intrusion length (Nguyen, 2008; Fig. 3.10).

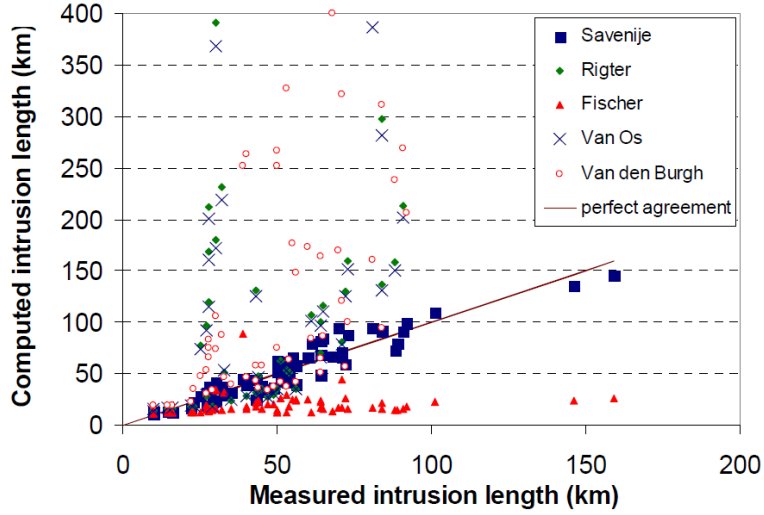


Fig. 3.10: Computed salinity intrusion length at High Water Slack for different methods (Savenije, 2005).

The theory of Savenije (2005) to compute the salt intrusion length reads

$$L_{HWS} = a \ln \left( 1400 \frac{h_0 E_0 U_0}{\zeta a^2 u_0} Ri_e^{0.5} + 1 \right), \quad (\text{Eq. 3.10})$$

where  $L_{HWS}$  is the intrusion length (m) at high water slack (the moment just before the tidal current reverses),  $a$  is the area convergence or  $e$ -folding length (m),  $h_0$  is the depth at the estuary mouth (m),  $E_0$  is the tidal excursion at the estuary mouth (m),  $U_0$  is the tidal velocity amplitude at the river mouth ( $\text{m s}^{-1}$ ),  $\zeta$  is the Van den Burgh's coefficient (which has a value between 0 and 1),  $u_0$  is the mean cross-sectional velocity at the estuary mouth ( $\text{m s}^{-1}$ ) and  $Ri_e$  is the estuarine Richardson number.

Recently, Gisen et al. (2015) revised the equations for salt intrusion length of Savenije (1993; 2005). This was done by including new, previously un-surveyed estuaries in this new analysis. As a result, three new equations for quantifying salt intrusion length at high water slack were proposed. These new equations read

$$L_{HWS} = x_1 + a \ln \left( 0.1167 \frac{E_1 U_1}{\zeta a u_1} Ri_e^{0.57} + 1 \right) + \frac{E_0}{2}, \quad (\text{Eq. 3.11})$$

$$L_{HWS} = x_1 + a \ln \left( 0.3958 \frac{E_1 U_1 g^{0.21}}{\zeta a u_1 C^{0.42}} Ri_e^{0.57} + 1 \right) + \frac{E_0}{2}, \quad (\text{Eq. 3.12})$$

$$L_{HWS} = x_1 + a \ln \left( 1.9474 \frac{E_1 U_1 g^{0.51}}{\zeta a u_1 C^{1.02}} Ri_e^{0.51} + 1 \right) + \frac{E_0}{2}, \quad (\text{Eq. 3.13})$$

where  $x_1$  (m) is the inflection point (the location where the estuarine geometry changes from wave-dominated to tide-dominated; Gisen et al., 2015),  $a$  is the area convergence (m),  $E_1$  is the tidal excursion at the inflection point (m),  $U_1$  is the tidal velocity amplitude at the inflection point ( $\text{m s}^{-1}$ ),  $\zeta$  is the Van den Burgh's coefficient (which has a value between 0 and 1),  $u_1$  is the mean flow velocity at the inflection point ( $\text{m s}^{-1}$ ),  $Ri_e$  is the estuarine Richardson number,  $g$  is gravity acceleration ( $\text{m s}^{-2}$ ) and  $C$  is the Chézy coefficient ( $\text{m}^{1/2} \text{s}^{-1}$ ).

The most challenging part of the theory of Savenije (2005) and Gisen et al. (2015) is to determine the Van den Burgh coefficient ( $\zeta$ ). Savenije (1993) came up with an empirical equation for  $\zeta$ , which reads

$$\zeta = 0.16 \times 10^{-6} \frac{h_0^{0.69} g^{1.12} T^{2.24}}{H_0^{0.59} b^{1.10} B_0^{0.13}}. \quad (\text{Eq. 3.14})$$

Here,  $h_0$  (m),  $H_0$  (m) and  $B_0$  (m) are the depth, tidal range and width at the estuary mouth. The tidal period (s) is denoted by  $T$ , the width convergence length (m) by  $b$  and  $g$  denotes the gravity acceleration ( $\text{m s}^{-2}$ ). Gisen et al. (2015) also revised the empirical equation for  $\zeta$ . The new equation reads

$$\zeta = 151.35 \times 10^{-6} \left( \frac{B_{up}^{0.30} H_1^{0.13} T^{0.97}}{B_1^{0.30} C^{0.18} U_1^{0.71} b^{0.11} h_1^{-0.15} r_s^{0.84}} \right), \quad (\text{Eq. 3.15})$$

where  $B_{up}$  is the upstream river width,  $C$  is the Chézy coefficient ( $\text{m}^{1/2} \text{s}^{-1}$ ) and  $r_s$  denotes the storage-width ratio (the ratio between storage width and stream width, which equals 1 in this case).

Brockway et al. (2005) came up with an easier expression for the intrusion length, based on measurements in the well-mixed Incomati estuary in Mozambique. Their equation reads

$$L = \left( \frac{1}{\gamma} \right) \ln \left( \frac{4.6 A_0 \gamma K_x}{Q_{fresh}} + 1 \right), \quad (\text{Eq. 3.16})$$

in which  $\gamma$  is an estuarine tapering factor (equivalent to the inverse  $e$ -folding length scale for area),  $K_x$  is a longitudinal mixing coefficient ( $\text{m}^2 \text{s}^{-1}$ ),  $Q_{fresh}$  is the river discharge ( $\text{m}^3 \text{s}^{-1}$ ) and  $A_0$  is the cross-sectional area at the estuary mouth ( $\text{m}^2$ ). This equation is based on the theory of Savenije (1986; 1993) and also includes the exponential shape of many estuaries. However, the horizontal diffusion coefficient was kept constant along the length of the estuary. This assumption was criticised by Savenije (2006), who showed that adding more parameters to the equation of Brockway et al. (2005) leads to a more generally applicable formulation. This equation bears a close resemblance to Eq. 3.10 and is defined as

$$L_{HWS} = \frac{1}{\gamma} \ln \left( 1400 \gamma^2 \frac{h_0 E_0 U_0 A_0}{\zeta Q_{fresh}} Ri_e^{0.5} + 1 \right). \quad (\text{Eq. 3.17})$$

A comparison of the method of Savenije (2006) and Brockway et al. (2005) on a dataset of 15 estuaries showed that the method of Brockway et al. (2005) mostly underestimates the salt intrusion length. Their method only gives reasonable results for the estuaries it was calibrated on (Fig. 3.11).

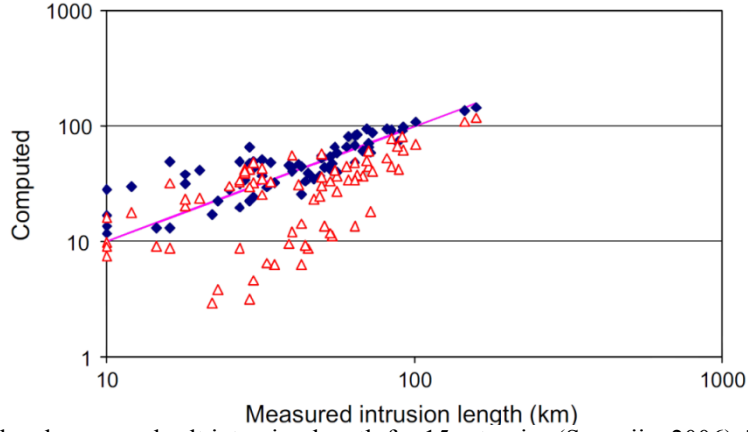


Fig. 3.11: Computed and measured salt intrusion length for 15 estuaries (Savenije, 2006). The red triangles are computed using the method of Brockway et al. (2005), whilst the blue diamonds have been computed using the method of Savenije (1993). The purple line is the line of perfect agreement.

An intrusion model that is not discussed by Savenije (2005) and Nguyen (2008) is the model of MacCready (2004). Using this model, it is possible to obtain length scales for salt intrusion that are related to salt transport by the exchange flow and diffusion. These length scales are defined as (MacCready, 2004)

$$L_e = \left( \frac{-\overline{P_D P_s} h^2 \alpha^2 S_0^2}{K_z |\bar{u}|} \right)^{1/3}, \quad L_K = \frac{K_x}{|\bar{u}|}, \quad (\text{Eq. 3.18})$$

in which

$$P_D = 1 - 9 \left( \frac{z}{-h} \right)^2 - 8 \left( \frac{z}{-h} \right)^3, \quad P_s = -\frac{1}{12} + \frac{1}{2} \left( \frac{z}{-h} \right)^2 - \frac{3}{4} \left( \frac{z}{-h} \right)^4 - \frac{2}{5} \left( \frac{z}{-h} \right)^5,$$

$$\alpha = \frac{g\beta h^3}{48N_z}.$$

Here,  $L_e$  is the length salt can be transported by the exchange flow (m),  $L_K$  is the length salt can be transported by diffusion (m),  $-\overline{P_D P_s}$  is equal to 19/360,  $h$  is the water depth (m),  $S_0$  is the oceanic salinity (psu),  $K_z$  is the vertical diffusion coefficient ( $\text{m}^2 \text{s}^{-1}$ ),  $K_x$  is the horizontal diffusion coefficient ( $\text{m}^2 \text{s}^{-1}$ ),  $|\bar{u}|$  is the depth-averaged absolute flow velocity ( $\text{m s}^{-1}$ ),  $g$  is the gravitational acceleration ( $\text{m s}^{-2}$ ),  $\beta$  ( $7.6 \cdot 10^{-4} \text{ psu}^{-1}$ ) is the coefficient of isohaline contraction,  $z$  is the vertical axis (m) and  $N_z$  is the turbulent eddy viscosity coefficient ( $\text{m}^2 \text{s}^{-1}$ ). At  $z = h$ , the bottom of the estuarine channel is located.

A limitation of the solutions and models discussed so far is that they have all been developed for single-channel estuaries. However, many estuaries consist of multiple branches. Well-known examples are the Mekong Delta in Vietnam, the Yangtze Delta in China and the Berau Delta in Indonesia. A multi-channel estuary is fundamentally different from a single-channel estuary because in a multi-channel estuary the different branches mutually interact. It is possible that the tidal wave enters through one channel and exits through the other channel or that salt is transferred between the two channels. Moreover, the two channels may have a different length, width, depth and freshwater discharge, which will lead to separate hydrodynamic behaviour in each branch. Even though many estuaries around the globe are characterised by multiple channels, these multi-channel estuaries have received to date only limited attention from the global scientific community. The next paragraph discusses a few of the scientific studies that deal with salt intrusion in multi-channel estuaries.



### 3.7 Salt intrusion in multi-channel estuaries

Nguyen & Savenije (2006) tested whether the theory of Savenije (2005) could be used to compute the salinity intrusion in the multi-channel Mekong Delta. The universal theory from Savenije (2005) is based on 15 estuaries all over the globe and only needs some basic estuarine properties, like topography, tide and freshwater discharge (Savenije, 1986; 1989; 1993). It is claimed that this theory can be applied to quantify the salinity intrusion in all alluvial estuaries. The drawback of this theory is that it has not been developed for multi-channel estuaries and for estuaries where the tidal wave is damped considerably due to a high freshwater discharge. The Mekong is a good example of a multi-channel estuary with a lot of tidal damping, which is why it was decided to test the theory on this estuary.

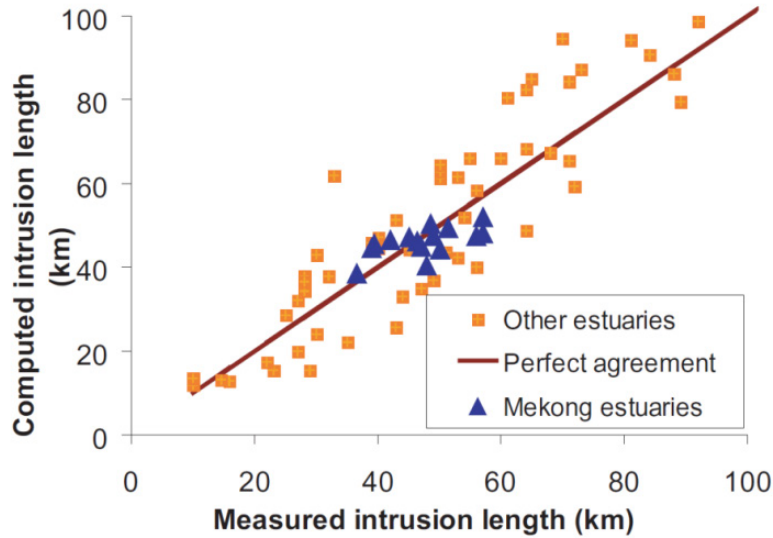


Fig. 3.12: The computed salt intrusion length using the modified model of Savenije (2005), as described by Nguyen & Savenije (2006). Shown are the results for the Mekong branches and other estuaries that are described by Savenije (2005).

Similar hydraulic, topographical and salinity characteristics were discovered in the different branches of the Mekong Delta, suggesting that the multi-channel estuary system functions as an entity and the paired branches can be considered as a single estuary branch. This adding of branches is done by adding the area and width of both branches. The salinity of the combined estuary is computed as the weighted mean between the areas of both branches. The equation for salt intrusion length at high water slack in the multi-channel Mekong Delta reads (Nguyen & Savenije, 2006)

$$L_{HWS} = a \ln \left( 1400 \frac{\langle h \rangle E_0 U_0 A_0}{\zeta a Q_{fresh} b} Ri_e^{0.5} + 1 \right), \quad (\text{Eq. 3.19})$$

where  $\langle h \rangle$  is the tidally averaged depth (m),  $E_0$  is the tidal excursion at the estuary mouth (m),  $U_0$  is the tidal velocity amplitude at the estuary mouth ( $\text{m s}^{-1}$ ),  $A_0$  is the area at the estuary mouth ( $\text{m}^2$ ),  $\zeta$  is the Van den Burgh's coefficient (which has a value between 0 and 1),  $a$  is the area convergence length (m),  $Q_{fresh}$  denotes river discharge ( $\text{m}^3 \text{s}^{-1}$ ),  $b$  is the width convergence length (m) and  $Ri_e$  is the estuarine Richardson number.

Applying this slightly altered version of the theory of Savenije (2005) to the Mekong Delta proved to be successful (Fig. 3.12). Even though the original theory is not developed for this kind of situations, slightly altering it and combining paired estuary branches leads to satisfactory results. However, more updated topographical data regarding the Mekong Delta is

needed to improve this study. Apart from that, the model is also sensitive to some estuarine properties which can be quite uncertain. This applies to the mean estuary depth and the freshwater discharge. Finally, it is also difficult to determine the average depth over a cross-section, particularly when both shallow and deep parts exist side by side and the estuary depth is not constant (Nguyen & Savenije, 2006).

To apply the theory of Savenije (2005) and Nguyen & Savenije (2006), two main boundary conditions are needed. These are the tidal characteristics at the estuary mouth and the fresh water discharge at the estuary head. Determining the freshwater discharge is difficult as detailed measurements during the entire tidal cycle are necessary. A system with multiple branches, such as the Mekong Delta, adds even more difficulty. To overcome this, Nguyen et al. (2008) investigated whether it was possible to use the theory of Savenije (2005) to calculate the freshwater discharge over the different branches of the Mekong Delta. This proved possible, but for this it is necessary to know the topography, tide and salinity distribution. However, the salinity model has some limitations when it is used to determine the discharge distribution in the Mekong Delta. The model is sensitive to errors in mean depth, width and boundary conditions. Apart from that, it is also necessary to obtain salinity measurements in each branch over the same period, which requires a lot of equipment, transport and human resources. Apart from that, Nguyen et al. (2008) computed the salinity model and discharge distribution under the assumption that the discharge is constant in the considered period. For the Mekong River, this is a justified assumption. However, this might not be the case for estuaries with a longer reaction time. Finally, the fresh water computation is only valid for partially to well-mixed estuaries with only limited stratification effects and where tidal action dominates over river flows (Nguyen et al., 2008).

Some years later, the theory of Savenije (2005) was also successfully applied to the Chinese Yangtze estuary (Zhang et al., 2011), resulting in a good fit between measured and computed salinity values. Also here, equal hydraulic, topographical and salt patterns were discovered in the different channels, strengthening the hypothesis that paired branches should be considered as a single estuary branch. However, more accurate bathymetry measurements and detailed observations are needed to improve the quality of this study. Wu et al. (2010) applied a numerical model to the Changjiang estuary (that forms part of the Yangtze Delta), whose results indicated both the importance of Stokes transport and the exchange of water masses between the different channels. Another study was performed by Gong et al. (2012), who applied a 3D numerical model to a part of the Chinese Pearl River Delta (Fig. 3.13). In this study, it was found that the different branches in this multi-channel estuary could act as either a salt source or a salt sink. The problem with these model studies is that they all deal with real estuaries, meaning that the studies are often as realistic as possible. As a result, all channels in the estuary are taken into account, leading to many bifurcations and confluences that make the resulting model grids very complex. At the same time, very complex boundary conditions are often chosen for the models, as they come closest to reality. For example, the numerical model study by Gong et al. (2012) uses an offshore boundary that is forced by 8 tidal constituents, whilst the numerical model study by Wu et al. (2010) uses an open ocean boundary that is forced by 16 tidal constituents. Such model studies may come close to reality, but it is nearly impossible to analyse the underlying mechanisms that play a role in an estuarine environment with such difficult boundary conditions. For example, it is possible that the many tidal constituents interact with each other, leading to strange salt patterns in the estuary. To overcome this, there is a need for more simple models, from which it is easier to analyse the underlying physical mechanisms.

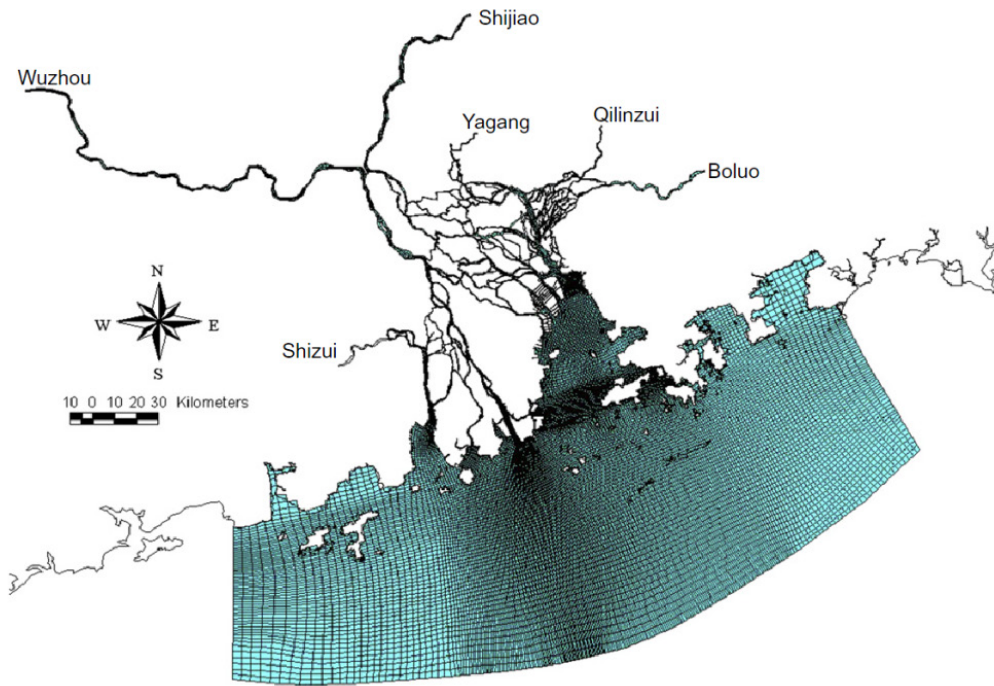


Fig. 3.13: Example of the model grid, used in the study by Gong et al. (2012). It is clear that this model grid comes very close to reality but that at the same time it is very complex with lots of bifurcations and confluences.

Until now, not many simple modelling studies have been carried out with regards to the hydrodynamics in estuarine tidal networks. Observations from the Berau delta in Indonesia suggest that the tidally averaged flow division at tidal junctions depends on the tidal range. Buschman et al. (2010) constructed a depth-averaged hydrodynamic model in Delft3D with idealised geometry, which mimics to some extent the Berau Delta in Indonesia. This model was used to learn more about the exact mechanisms which determine subtidal flow division at estuarine channel junctions. The model of Buschman et al. (2010) comprises of a tidal river of a few hundred kilometres long, which splits in two exponentially converging tidal channels. By changing the length, depth, e-folding length scale of the channel width, and hydraulic roughness in one of the two tidal channels, the effect of these changes on subtidal flow division was studied. The results indicated that when the depth, length, and e-folding length scale were varied in one channel, the tide increased the inequality in subtidal flow division at the tidal junction. At the same time, altering the hydraulic roughness in one channel resulted in tidal action decreasing the inequality in subtidal flow division at the tidal junction. The study by Sassi et al. (2011) investigated subtidal flow division for the Indonesian Mahakam Delta using a depth-averaged version of SLIM, the Second-generation Louvain-la-Neuve Ice-ocean Model. This study concluded that tides only affected subtidal flow division in the Mahakam Delta close to the sea. The same types of studies have already been conducted for river junctions (Wang et al., 1995; Kleinhans et al., 2008), but they did not focus on the downstream junctions, where tides also play a role.

### **3.8 Objectives of the present study**

The studies of Buschman et al. (2010) and Sassi et al. (2011) do not include the effect of salinity and use a depth-averaged (2DH) model instead of a 3D model to simulate the hydrodynamics in an estuarine tidal junction network. Analogously to a tidal wave, salt also intrudes upstream through the different branches from the seaward side. When investigating estuarine flow patterns, it is therefore important to also consider the effect of salt. When salt is included in a model study, it is essential to use a 3D model. The reason for this is that both cross-channel flow patterns and horizontal/vertical density differences are important for

studying salinity patterns. According to the knowledge of the author, no theoretical studies are available that investigate salinity intrusion in an estuarine channel network. Most studies focus on an existing estuary with rigid borders and extensive boundary conditions, making it difficult to clarify the underlying mechanisms. To close this gap, a new study has been carried out in the framework of this thesis, which focuses on salt intrusion using the 3D version of the model developed by Buschman et al. (2010). This study investigates the effect of varying the length of one of the downstream estuarine channels on salt intrusion and tidal propagation in the estuarine channel network. The main research question of this study will therefore be:

- What is the effect of varying the length of one downstream channel on salinity intrusion and tidal propagation in a two-channel estuarine tidal network?

To answer this main question, I will focus on the following sub-questions:

- What are the tidal water level and tidal velocity amplitudes in the different channels?
- What is the character of the tidal wave in the various channels?
- What are the physical mechanisms and processes that control salinity intrusion in partially-mixed and well-mixed estuaries?
- How is freshwater and salinity distributed over a well-mixed estuarine channel network when varying the length of one of the tidal channels?
- What is the relative role of cross-sectional advective and dispersive salt transport while varying the length of one of the downstream channels and what are the magnitudes of these different transport terms in the different channels?

### **3.9 Methodology**

This study will be conducted using an idealised 3D model (Delft3D, see Lesser et al., 2004). This model is widely used and is able to include the effects of salt-induced density on the hydrodynamics. In this study, an idealised setting will be used in which the domain is similar to that in Fig. 3.14. The domain is characterised by a constant depth throughout the grid, tidal forcing (single constituent at seaward boundary, identical for both channels), salinity and river discharge (no wind, waves and sediment). In order to include salinity, it is required to use the 3D version of Delft3D. This means that the model used by Buschman et al. (2010) needs to be modified and newly calibrated as they used the depth-averaged (2DH) version of Delft3D. Using the modified model, multiple simulations will be conducted that will focus on the salt dynamics at the tidal junction and the other parts of the estuary. By varying the length of channel 1, the influence of variations in channel length on the tidal and salinity patterns is investigated. The next chapter (Chapter 4) provides a detailed description of the model set-up, whilst the results of this study are extensively described in Chapter 5.

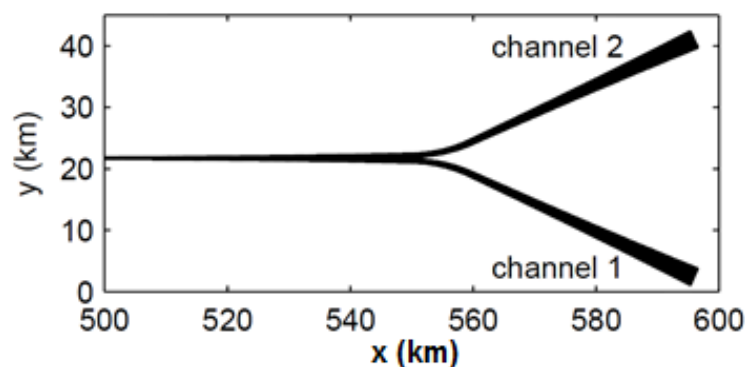


Fig. 3.14: Top view of the Delft3D grid used by Buschman et al., (2010), consisting of a river that splits in two equal branches. A similar kind of grid will be used in this thesis.

## 4. Model set-up

### 4.1 Model set-up

The initial model set-up used in this study is based on the model by Buschman et al. (2010), which in turn is based on the model study by Kleinhans et al. (2008). This model was built using the Delft3D modelling environment and solves the unsteady shallow water equations as described in Lesser et al. (2004). An extensive description of all the governing equations in Delft3D is provided in Lesser et al. (2004), Van der Wegen & Roelvink (2008) and the Delft3D Flow Manual (Deltares, 2014). There is an important difference between the model set-up of this study and that of Buschman et al. (2010). Since this study focuses on salinity intrusion, it was decided to use the 3D version of Delft3D instead of the depth-averaged (2DH) version of Delft3D. The reason for this is that both cross-channel flow patterns and horizontal/vertical density differences are important for studying salinity patterns. Additionally, it is also essential to take into account both horizontal and vertical density differences, to be able to obtain information about the stratification of the channels.

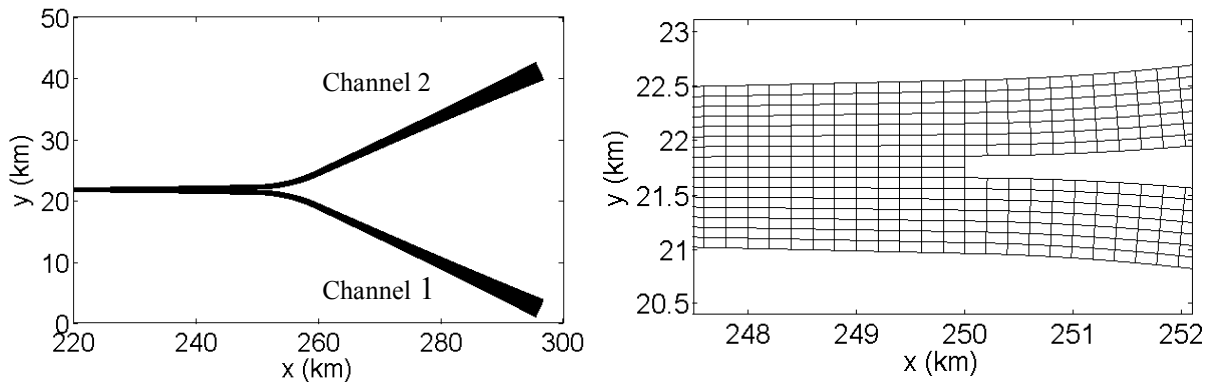


Fig. 4.1: Left = The seaward part of the model grid, in which the single river and the two channels that connect to sea are illustrated. Right = Detailed overview of the gridcells at the tidal junction. The two disappearing grid cells are clearly visible.

In the default setting of this study, the distance between the tidal junction and the sea is 50 km. The river in the model is 250 km long, so that tides can dampen out to a certain degree. In the upstream 200 km of the river, the width is set to 357 m. At a distance 200 km from the upstream river boundary, the channel width ( $B$ ) starts to increase according to the exponential formula

$$B = B_{up} e^{x/b}, \quad (\text{Eq. 4.1})$$

where  $b$  is the so called  $e$ -folding length for width (m) and  $x$  are the along-channel coordinates (defined positive seaward). In this case, the default setting of  $b$  is set at 33.3 km, which results in a width of 1.60 km at the tidal junction. Whilst the width of the grid cells varies throughout the grid, the grid cell length along the centre line of the three channels is set constant at 200 m. The river landward of the tidal junction has a width of 16 equally divided grid cells across the channel. At the tidal junction, this single channel splits in two equal channels of 50 km in length. Due to numerical issues with splitting the channel, two cell rows have to disappear seaward of the junction (Fig. 4.1; Kleinhans et al., 2008). Therefore, channel 1 and 2 are both 7 grid cells wide. By applying this method, only one-eighth of the cross-sectional area is lost due to grid cells being removed on the seaward side of the tidal junction. At the tidal junction, the grid cell length is twice as large as the grid cell width. This small ratio was chosen to

account for cross-channel flows that can occur just landward of the junction. The ratio increases when moving further inland.

Table 4.1: Default parameter settings for the Buschman et al. (2010) setup and the modelling setup of this thesis.

Variable	Buschman default settings	Thesis first default settings
Number of layers	1	10
Length of upstream channel	550 km	250 km
Length of downstream channels	50 km	50 km
Still water depth	5 m	5 m
Simulation time	23 days	1 month
Time step	30 s	30 s
Initial water level	5 m	0 m
Initial salinity in the grid	N/A	0 psu
River discharge	500 m <sup>3</sup> s <sup>-1</sup>	200 m <sup>3</sup> s <sup>-1</sup>
$M_2$ amplitude at sea	0.7 m	0.7 m
$S_2$ amplitude at sea	0.4 m	0 m
Salinity value at seaward boundary	N/A	34 psu
Salinity value at landward boundary	N/A	0 psu
Thatcher-Harleman time lag	N/A	0 min
Chézy coefficient	55 m <sup>1/2</sup> s <sup>-1</sup>	55 m <sup>1/2</sup> s <sup>-1</sup>
Horizontal eddy viscosity	10 m <sup>2</sup> s <sup>-1</sup>	10 m <sup>2</sup> s <sup>-1</sup>
Horizontal eddy diffusivity	N/A	10 m <sup>2</sup> s <sup>-1</sup>
Vertical eddy viscosity (background)	N/A	10 <sup>-6</sup> m <sup>2</sup> s <sup>-1</sup>
Vertical eddy diffusivity (background)	N/A	10 <sup>-6</sup> m <sup>2</sup> s <sup>-1</sup>
3D turbulence model	N/A	$k-\varepsilon$

In the initial model, 10 vertical layers were defined and the depth was set to 5 m. The model is situated at the equator, meaning that there is no Coriolis Effect. A time step of 30 s was used. Calculations of the Courant number showed that this time step was sufficiently small. The hydraulic roughness was expressed using a Chézy coefficient of 55 m<sup>1/2</sup> s<sup>-1</sup>, which is a value that is often used for hydraulic roughness in tidal channels (Buschman et al., 2010). The horizontal eddy viscosity and horizontal eddy diffusivity were both set to 10 m<sup>2</sup> s<sup>-1</sup>, whilst the vertical eddy viscosity and horizontal eddy diffusivity were set to 10<sup>-6</sup> m<sup>2</sup> s<sup>-1</sup>. The 3D turbulence model was set to  $k-\varepsilon$ . The model is forced with a constant river discharge of 200 m<sup>3</sup> s<sup>-1</sup> at the upstream boundary, whilst a  $M_2$  tidal amplitude of 0.7 m and equal phase is prescribed at both seaward boundaries (located at the end of both channels), with a constant salinity of 34 psu. The duration of the default model run was 1 month, to allow salt to intrude sufficiently in the network and to reach a partial equilibrium. An overview of the first default parameter settings compared to the default parameter settings of Buschman et al. (2010) and Buschman (2011) is given in Table 4.1.

#### **4.2 Model calibration**

Using the settings in Table 4.1, a first model run was performed to investigate the behaviour of the altered model. All simulations were performed with Delft3D Flow version 4.00.02. Firstly, plots of the water level throughout the grid domain were analysed. This revealed that the tide is perfectly harmonic at the seaward boundary, but it gets distorted when moving upstream. Apart from that, strange patterns start to emerge closer to the landward boundary. These sudden peaks (hereafter referred to as ‘wiggles’; Fig. 4.2) point to numerical instabilities and indicate that the results of the model run are possibly not correct. As soon as these wiggles appear in the water level plots, they also appear in the velocity plots and in the salinity plots. This means that the results of such a model run are not to be trusted.

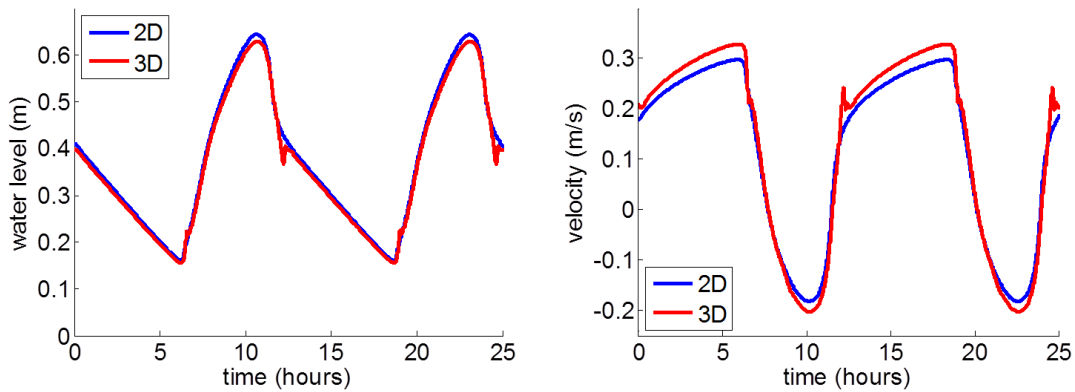


Fig. 4.2: Wiggles in the water level (left) and depth-averaged velocity (right) using the 3D version of Delft3D. For comparison, the results of the same simulation with the 2DH version of Delft3D are also plotted. The position is 80 km from the downstream boundary.

This implies that it is essential that these wiggles do not appear in the water level and the velocity results. Therefore, the first model calibration task was to find out how these wiggles could be prevented from occurring. This was done by running a number of different simulations with slightly altered parameter settings. Only one parameter was changed per simulation run, to be able to investigate in detail the effect on the model results. Firstly, the same simulation was conducted in the 2DH version of Delft3D, to see whether the problem had to do with the dimensions of the simulation. The result was that the wiggles did not occur in this simulation (Fig. 4.2), meaning that the problem occurs due to some setting in the 3D version that is not used in the 2DH version of Delft3D.

At first, attention was given to the boundaries in the 3D simulation. There are different ways in Delft3D to define a boundary. The default forcing type for a tidal boundary is astronomic, meaning that the flow conditions are prescribed using build-in tidal constituents, amplitudes and phases (Deltares, 2014). Apart from that, harmonic conditions can be imposed at a tidal boundary, meaning that the flow conditions are specified using user-defined frequencies, amplitudes and phases (Deltares, 2014). For each boundary, a so called reflection parameter also needs to be set. The higher the value of this parameter, the less reflective the open boundary gets for waves that arrive at the boundary from inside the model (Deltares, 2014). Since the wiggles are predominantly visible close to the landward river boundary, it was hypothesised that reflection of the tidal wave caused the formation of the wiggles. Increasing the reflection parameter should in that case lead to a reduction of the wiggles. However, both changing the forcing and the reflection parameter did not have the desired effect.

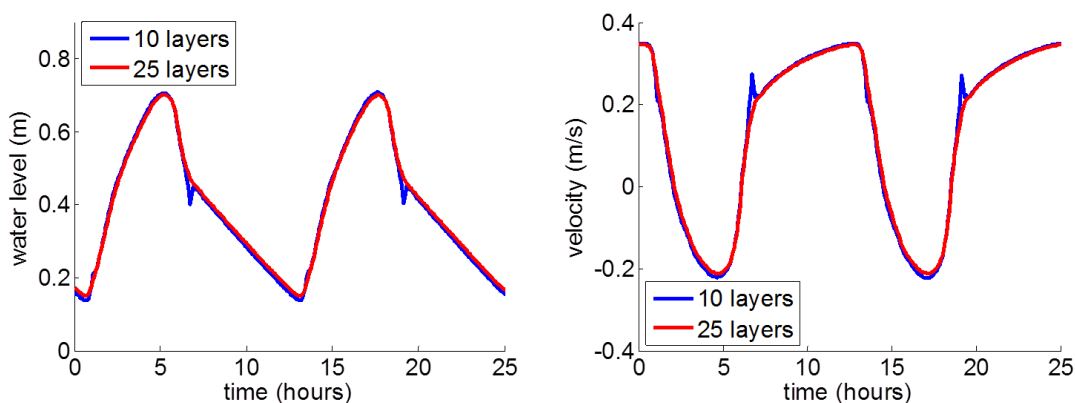


Fig. 4.3: Water level (left) and depth-averaged velocity (right) for a 3D simulation with 25 layers (in red). For comparison, the results of the same simulation with 10 layers (in blue) are also plotted. The position is 80 km from the downstream boundary.



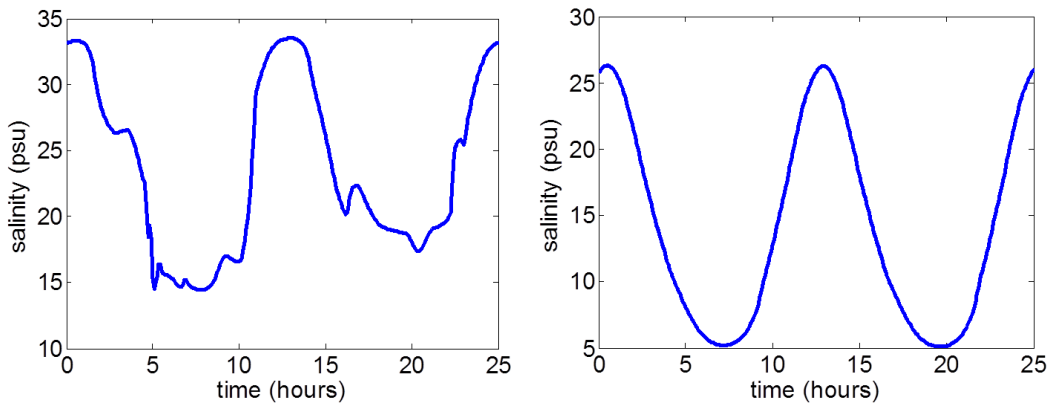


Fig. 4.4: Example of a salinity profile in a 25 layer model with the  $k-\varepsilon$  turbulence closure model (left) and the  $k-l$  turbulence closure model (right).

Next, it was decided to increase the number of vertical layers from 10 to 25. Many modelling studies (e.g. Simpson et al., 2001; Burchard & Hetland, 2010) often use at least 50-100 layers in the vertical since this drastically increases the accuracy. The downside is that it takes much longer to run these models. However, salt studies with Delft3D (such as Van Breemen, 2008) often only use 10 vertical layers. By increasing the number of vertical layers from 10 to 25, the vertical resolution is increased by 150%. Increasing the vertical resolution had a positive effect (Fig. 4.3), as the wiggles in water level and velocity disappeared completely.

### **4.3 Sensitivity to turbulence closure models**

The focus now shifted to the salinity profiles through time. It was soon found that both the simulations with 10 and 25 vertical layers still showed a lot of wiggles in the salinity profiles (Fig. 4.4, left). As a result, the focus shifted to the physical parameters in Delft3D, which could also affect the density patterns of the simulation. It was decided to alter the so called ‘Model for 3D turbulence’ and investigate what effect altering this parameter had on the model results. Delft3D-FLOW has four different turbulent closure models implemented to determine the vertical eddy viscosity and vertical eddy diffusivity. These models are:

- Constant coefficient.
- Algebraic Eddy viscosity closure Model (AEM).
- $k-l$  turbulence closure model.
- $k-\varepsilon$  turbulence closure model.

The difference between these turbulent closure models is the way they describe the turbulent kinetic energy  $k$ , the dissipation rate of turbulent kinetic energy  $\varepsilon$ , and/or the mixing length  $l$ . The first turbulence closure model is very simple and uses values for vertical eddy viscosity and diffusivity that are constant in space and time and are prescribed by the user himself. Note that a constant eddy viscosity results in parabolic vertical velocity profiles (laminar flow; see Deltares, 2014). The other three turbulence closure models are all based on the eddy viscosity concept of Kolmogorov (1942) and Prandtl (1945). In those cases, the eddy viscosity is linked to the characteristic velocity and length scale of the resolved flow. Moreover,  $k$  is determined using the turbulent energy balance. This equation describes the production of  $k$  due to velocity shear, destruction of  $k$  due to buoyancy and dissipation due to viscous terms. In its simplest form this equation becomes a balance between the production and buoyancy term. An extensive description of all turbulence closure models is given in the Delft3D flow manual (Deltares, 2014) and in Uittenbogaard et al. (1992). Below, a brief description of the remaining three models will be provided.



The algebraic eddy viscosity model (AEM) does not use transport equations for turbulence. Therefore, it is called a zero order closure scheme, which is in this case a combination of two algebraic formulations. The AEM model uses analytical (algebraic) formulas to calculate  $k$  and  $l$ . The turbulent kinetic energy  $k$  is defined as

$$k = \frac{\overline{u_t u_t}}{2}. \quad (\text{Eq. 4.2})$$

Here,  $u_t$  denotes turbulent fluctuations in along channel velocity and the bar denotes an average over the turbulent timescale. From Eq. 4.2, it follows that the velocity scale  $U_{sc}$  can be defined as  $U_{sc} = k^{1/2}$ . The friction velocities or velocity gradients determine the turbulent kinetic energy  $k$  and the mixing length  $l$  is calculated using a depth-function (Bakhmetev, 1932)

$$l = \kappa(h - z) \sqrt{1 - \frac{h-z}{(h+\eta)}}, \quad (\text{Eq. 4.3})$$

where  $\kappa$  is the Von Kármán constant ( $\approx 0.41$ ),  $z$  is the vertical coordinate (m, positive downward),  $h$  is the water depth (m) and  $\eta$  is the water level (m). The result is a logarithmic velocity profile in case the flow is homogeneous. When vertical density gradients are present, the turbulent exchanges are severely limited by buoyancy forces and  $l$  needs to be corrected. However, high gradients in velocity can lead to increased turbulent mixing which in turn may weaken the stratification. The stability of the stratification can be described by the interaction between gravitational forces and turbulent shear production. The measure for the stratification is given by the earlier mentioned gradient Richardson number ( $Ri$ ; Deltares, 2014).

The so called  $k$ - $l$  turbulence closure model is a first order turbulence closure scheme. In this model, the mixing length  $l$  is not calculated but prescribed analytically. The same formulation and damping functions are used as for the AEM turbulence, but a transport equation is added to determine the kinetic energy  $k$ . This transport equation includes an energy dissipation term, a buoyancy term and a production term. The full set of equations belonging to this closure model is available in Deltares (2014). Assumptions made in this model are that the production, buoyancy and dissipation terms dominate and that the horizontal length scales are far larger than the vertical length scales. In other words, this model is limited to relatively shallow water (Deltares, 2014).

The last turbulence closure model that is included in Delft3D is the so called  $k$ - $\varepsilon$  model, which is a second order turbulence closure model. Both the turbulence energy  $k$  and the dissipation rate of turbulent kinetic energy  $\varepsilon$  are calculated using a transport equation. Using the calculated results of  $k$  and  $\varepsilon$ , the turbulent velocity scale  $k^{1/2}$  and mixing length are determined, from which the vertical eddy viscosity and vertical eddy diffusivity are calculated. The mixing length  $l$  is computed from  $k$  and  $\varepsilon$  using

$$l = c_d \frac{k\sqrt{k}}{\varepsilon}. \quad (\text{Eq. 4.4})$$

Here,  $c_d$  denotes a constant relating mixing length, turbulent kinetic energy and dissipation in the  $k$ - $\varepsilon$  model. See Deltares (2014) for the full set of equations belonging to this closure model. Also the same assumptions are made as with the  $k$ - $l$  model. Thus the production, buoyancy and dissipation terms are the dominant terms and the horizontal length scales dominate over the vertical length scales (Deltares, 2014).

At first, all simulations were carried out by with the  $k-\varepsilon$  turbulence closure model, as this is the most advanced turbulence model available in Delft3D. But as the salinity profiles continued to show wiggles, the other turbulence models were also tested in some simulations. It soon became clear that using the  $k-l$  model led to hardly any wiggles in the salinity profile when it is applied to a case with 25 vertical layers (Fig. 4.4, right). Interestingly, applying this turbulence model to a case with 10 vertical layers also resulted in hardly any wiggles in the salt profiles. Also when the algebraic and constant turbulence models are applied to cases with 10 or 25 vertical layers, no wiggles appear in the salt profiles. After numerous attempts had failed in finding a  $k-\varepsilon$  model setting that did not result in the formation of wiggles in the salinity profiles, it was decided to no longer use this turbulence model. The  $k-l$  model is more sophisticated compared to the algebraic and constant turbulence model as it contains a correction term for stratification. Therefore it was decided to use the  $k-l$  turbulence model in the new simulations.

Moreover, it was decided to alter the Thatcher-Harleman time lags of both seaward boundaries. These time lags compensate for the effect that in a physical environment, the outflow concentration often differs from the boundary condition at inflow. As a result, there is an interruption in the concentration at the turn of the flow. Some time is needed before the concentration along the open boundary reaches the prescribed value again. To model this time lag in Delft3D, it is possible to define a Thatcher-Harleman boundary condition (Thatcher & Harleman, 1972). For these simulations, it was decided to set this value to 3 hours (180 min), which approaches half the period of the  $M_2$  tide.

#### **4.4 Finding the right boundary conditions**

After the correct physical settings had been found, attention shifted to determining the right boundary conditions. The boundary conditions should result in the estuary being partially to well-mixed and salt reaching the junction in sufficient quantities. The initial model set-up uses two symmetric downstream branches of 50 km in length. The results with the default model settings showed that salt intrudes approximately 15-20 km, which means that salt does not reach the tidal junction. Apart from that, the system was quite stratified (Fig. 4.5, left) with many wiggles. In order to increase the intrusion length and to get the system more mixed, it was decided to reduce the river discharge and to increase the tidal amplitude. The results of these simulations showed that salt could be forced to intrude up to 20-25 km inland. Most notable are the salinity profiles, which are clearly more mixed and show much less wiggles (Fig. 4.5, right). Another notable observation was that reducing the river discharge caused salt to intrude further upstream whilst increasing the tidal amplitude led to a slight decrease in intrusion length.

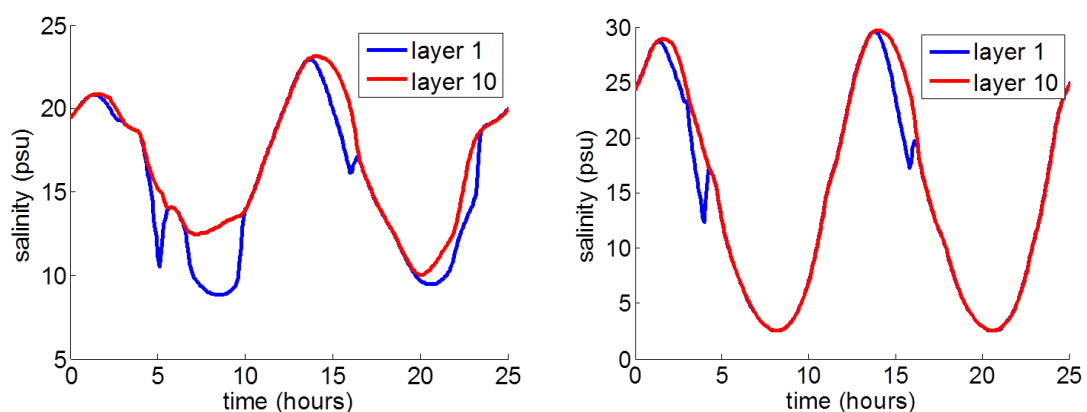


Fig. 4.5: Left = example of a salinity profile with the default settings. Right = example of a salinity profile with reduced discharge ( $100 \text{ m}^3 \text{ s}^{-1}$ ) and increased tidal amplitude (1.4 m).

The different simulations showed that modifying the amplitude and river discharge is not sufficient for salt to intrude up to the junction. As branches in an estuary with a length of 50 km are relatively long, it was decided to shorten the branches by 20 km. This way, salt could be forced to approach the junction more closely. Apart from that, following the theory of MacCready (2004), it was also decided to increase the water depth of the channels. Besides that, simulations were also performed with increased horizontal eddy diffusivity (mixing due to eddies). If the diffusivity is increased, this means that the mixing processes are increased, meaning that salt should intrude faster and further upstream. The simulation revealed that increasing the depth to 20 m caused salt to intrude up to 60 km upstream. Increasing the depth to 10 m causes salt to intrude 20 km upstream and if the horizontal eddy diffusivity was additionally increased to 100, the salt reached 45 km upstream. Note that even though the new settings caused salt to intrude further upstream, it also caused a substantial increase in stratification. This was evident in the salinity profiles, where wiggles started to emerge again, regardless of the used 3D turbulence model. It was suspected that these wiggles were a direct consequence of the increased stratification. It is known that Delft3D can have problems with simulating salinity intrusion in stratified conditions (e.g. De Goede, 2009) and the focus of this thesis is on partially to well-mixed estuaries. Therefore, it was decided to define the parameter settings in such a way that the salinity profiles remained partially to well-mixed. The resulting simulations indeed showed that as long as the difference in salinity between the upper and lower vertical layer is less than 5 psu, the wiggles in the salt profiles do not appear. After a few simulations with different values, it was decided to set the river discharge to  $100 \text{ m}^3/\text{s}$ , the  $M_2$  tidal amplitude to 1.4 m and the depth uniform to 10 m.

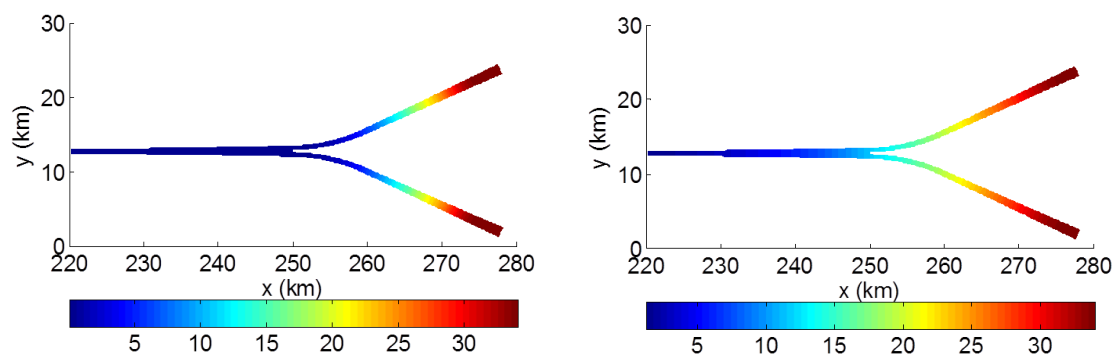


Fig. 4.6: Left = mean salt intrusion with  $100 \text{ m}^3 \text{ s}^{-1}$  river discharge, 1.4 m tidal amplitude and a depth of 10 m. Right = mean salt intrusion with the same conditions, but also with the horizontal diffusivity set to  $100 \text{ m}^2 \text{ s}^{-1}$ .

With the new parameter settings and two 30 km branches, the salt nearly reaches the tidal junction. By adjusting the horizontal eddy diffusivity, salt can be forced to intrude up to the junction, but in order to get reasonable salinity values this parameter had to be set to  $100 \text{ m}^2 \text{ s}^{-1}$  (Fig. 4.6). This is a very high value and therefore it was decided to shorten the two branches by another 10 km. This way, the horizontal eddy diffusivity could be set to  $30 \text{ m}^2 \text{ s}^{-1}$ , whilst the salt would still reach the junction in sufficient quantities. This resulted in new initial parameter settings, which are summarised in Table 4.2. Moreover, quite some time is needed for the salt to enter the estuary, especially when the initial setting is a completely fresh environment without any salt. In the new model settings it takes approximately 6 months to reach a salt equilibrium in the estuary with both branches 20 km long, provided that the initial conditions are completely fresh.

But still, there were some shortcomings in the model. The most notable is that salt is prescribed with a constant value at the end of the two branches. This is clearly visible in Fig. 4.6, where the downstream 10 km of both channels show a more or less high constant salinity.

In reality, salinity only reaches a constant value approximately 20-30 km offshore. In order to simulate these conditions in the model, it is essential to prescribe the salinity further offshore. To do this, a sea needs to be added to the existing grid which should contain the two downstream boundaries. There are two ways to do this, the first method is to generate a second grid and to combine this grid with the existing junction grid. This method proved to be unsuccessful due to numerical issues in connecting the grids with each other. The second method is to use a so called Domain Decomposition (DD; Deltares, 2014). In this technique, a model is divided in several smaller models or domains. The computations can then be carried out on these domains separately. The different models can still communicate with each other through internal boundaries (called DD-boundaries). This method allows for adding a second grid to an already existing grid and to link these grids to each other. Using this method, a sea of 20 km long and 13 km wide was added to the downstream end of both branches (Fig. 4.7). Salinity and tidal action is prescribed at the downstream end of the sea using an open boundary condition (dark blue lines in Fig. 4.7). With this final step, adequate model settings had been found to start the study on salinity intrusion with different channel lengths.

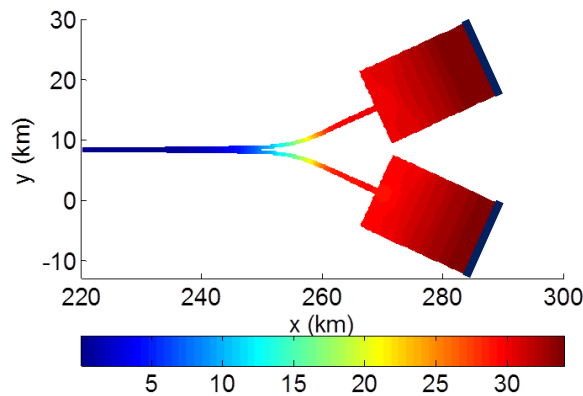


Fig. 4.7: Mean salinity in a DD simulation in which two equal seas are added to the downstream ends of the two branches. Model is run with the new initial model settings and salinity values are given in psu.

Table 4.2: Summary of the first (see Table 4.1) and final default settings. The final default settings were acquired by running multiple simulations to obtain the correct boundary conditions.

Variable	Thesis first default settings	Thesis final default settings
Number of layers	10	10
Length of upstream channel	250 km	250 km
Length of downstream channels	50 km	20 km
Still water depth	5 m	10 m
Simulation time	1 month	7 months – 1.5 year
Time step	30 s	30 s
Initial water level	0 m	0 m
Initial salinity	0 psu	0 psu
River discharge	200 m <sup>3</sup> s <sup>-1</sup>	100 m <sup>3</sup> s <sup>-1</sup>
$M_2$ amplitude at sea	0.7 m	1.4 m
Salinity value at sea	34 psu	34 psu
Thatcher-Harleman time lag	0 min	180 min
Chézy coefficient	55 m <sup>1/2</sup> s <sup>-1</sup>	55 m <sup>1/2</sup> s <sup>-1</sup>
Horizontal eddy viscosity	10 m <sup>2</sup> s <sup>-1</sup>	10 m <sup>2</sup> s <sup>-1</sup>
Horizontal eddy diffusivity	10 m <sup>2</sup> s <sup>-1</sup>	30 m <sup>2</sup> s <sup>-1</sup>
Vertical eddy viscosity	10 <sup>-6</sup> m <sup>2</sup> s <sup>-1</sup>	10 <sup>-6</sup> m <sup>2</sup> s <sup>-1</sup>
Vertical eddy diffusivity	10 <sup>-6</sup> m <sup>2</sup> s <sup>-1</sup>	10 <sup>-6</sup> m <sup>2</sup> s <sup>-1</sup>
3D turbulence model	$k-\varepsilon$	$k-l$

## 5. Modelling the effect of length differences

When the new model settings had been found, the real study on salinity intrusion could be initiated. This was done by performing simulations in which the length of channel 1 was gradually increased from 20 to 100 km, the intermediate steps being 25, 30, 35, 40, 45, 50, 60 and 80 km. Note that since the width and depth variations are the same along channels 1 and 2, the longer channel has a wider channel mouth. Each channel is connected to an identical sea grid with a size of 20 by 13 km using Domain Decomposition. The simulation time was 7 months for the 20-35 km simulations, 8 months for the 40 km simulation, 9 months for the 45 km simulation and 1.5 years for the 50-100 km simulations. These simulation times were chosen to ensure that all simulations reached sufficient equilibrium.

### 5.1 Delft3D model results

Delft3D stores the calculated model results in different types of files. Mostly, the so called history and map files are used for analysing the model results. In history files, the model results are stored at user-defined monitoring points and cross-sections. These monitoring points and cross-sections are defined prior to starting the model run. Model results are stored at an interval which has to be set by the user. In this model study, the history interval was set to 5 min. The map files basically store the same quantities as the history files, but the major difference is that this is done for the entire grid. This means that the map files can be used to produce contour plots of multiple locations in the grid or even the entire grid, whilst history files can only be used to produce 2D plots of stored quantities at a certain location in the grid. Table 5.1 provides an overview of some important quantities that are stored in the history files.

Table 5.1: An overview of the most important quantities that are stored in the present Delft3D model setting.

Quantity	Definition/symbol	Unit
Water level in station	$\eta$	m
Depth in station	$h$	m
U-velocity (velocity in x-direction) per layer in station	$u$	$\text{m s}^{-1}$
V-velocity (velocity in y-direction) per layer in station	$v$	$\text{m s}^{-1}$
W-velocity (velocity in z-direction) per layer in station	$w$	$\text{m s}^{-1}$
Salinity concentrations per layer in station	$S$	psu
3D vertical eddy viscosity in station	$K_z$	$\text{m}^2 \text{s}^{-1}$
3D vertical eddy diffusivity in station	$N_z$	$\text{m}^2 \text{s}^{-1}$
Richardson number in station	$Ri$	-
Density per layer in station	$\rho$	$\text{kg m}^{-3}$
Total discharge through cross-section	$Q_{cum} = \iiint u \, dy \, dz \, dt$	$\text{m}^3$
Monumentary discharge through cross-section	$Q_{inst} = \iint u \, dy \, dz$	$\text{m}^3 \text{s}^{-1}$
Cumulative advective transport through cross-section	$Q_{cum \, salt \, adv} = \iiint uS \, dy \, dz \, dt$	$\text{psu m}^3$
Cumulative dispersive transport through cross-section	$Q_{cum \, salt \, disp} = - \iint K_x (dS/dx) \, dy \, dz \, dt$	$\text{psu m}^3$

## 5.2 Harmonic analysis

The tidal pattern in the different model simulations can be examined by performing a so called harmonic analysis on certain tidal characteristics. By fitting a number of tidal constituents, it is possible to determine in what way the tidal wave is distorted. A tidal signal consisting of only one component can be written as

$$\eta(t) = R \sin(\omega t + \phi) . \quad (\text{Eq. 5.1})$$

Here  $\eta$  is the water level (m),  $R$  is the amplitude,  $\omega$  the angular frequency ( $\text{rad s}^{-1}$ ),  $t$  is time (s) and  $\phi$  the phase (rad). The angular frequency can be calculated for the  $M_2$  tide using

$$\omega_{M_2} = 2\pi/T_{M_2} = 2\pi/12\text{h } 25\text{min} = 1.4052 \cdot 10^{-4} \text{ rad s}^{-1} , \quad (\text{Eq. 5.2})$$

in which  $T$  is the period of the tidal constituent (s). When more constituents are present, Eq. 5.1 can be written as

$$\eta(t) = \text{MEAN} + \sum_n c_n \sin(\omega_n t) + d_n \cos(\omega_n t) . \quad (\text{Eq. 5.3})$$

Here, MEAN is the mean water level and  $c_n$  and  $d_n$  are amplitudes belonging to the tidal component with angular frequency  $\omega_n$ . This equation can also be written in the form

$$\eta(t) = \text{MEAN} + \sum_n R_n \sin(\omega_n t + \phi_n) . \quad (\text{Eq. 5.4})$$

Here,  $R_n$  is the total amplitude,  $t$  is the time of high water and  $\phi_n$  is the phase. The phase and total amplitude are defined as:

$$R_n = \sqrt{c_n^2 + d_n^2} , \quad \phi_n = \tan^{-1} \left( \frac{d_n}{c_n} \right) . \quad (\text{Eq. 5.5})$$

To determine the amplitudes and phases of the tidal constituents that are fitted, a best fit will be made of a user-defined function  $\eta(t)$  to the modelled water level  $O(t)$  by minimising the root mean square error between  $\eta(t)$  and  $O(t)$ . The RMSE is calculated as

$$\text{RMSE} = \sqrt{\frac{1}{M} \sum_{k=1}^M (\eta(t_k) - O(t_k))^2} . \quad (\text{Eq. 5.6})$$

Here,  $\eta(t_k)$  is calculated using Eq. 5.4,  $O(t_k)$  is the observed water level and  $t_k$  are the components of the time vector. The harmonic analysis is firstly conducted on the calculated water levels in the different simulations. To determine the phase of the tidal wave at high water (when  $\eta(t)$  has its maximum value), it is important to take into account that a sine function is fitted. A sine function reaches its max value at  $\pi/2$ . To obtain the time of high water, the calculated phase  $\phi_n$  needs to be subtracted from  $\pi/2$ , which then has to be divided by the angular frequency of the fitted tidal component (thus  $\eta(t_{HW}) = (\pi/2 - \phi_n)/\omega_n$ ).

Analogous to the water levels, it is also possible to carry out a harmonic analysis on the calculated velocities. This way, it is possible to obtain the velocity amplitudes and phases of the different tidal constituents. The procedure is nearly identical to the harmonic analysis of the water levels. The major difference is that instead of water levels, velocities are used as input. Another difference is that in our model, the coordinate system is defined positive from land to the sea. As a result, flood velocities are negative and ebb velocities are positive. When

determining the phase of the max flood tidal velocity (thus the largest negative value), this needs to be taken into account. A sine function reaches its max negative value at  $-\pi/2$ . To obtain the time of max flood tidal velocity, the calculated phase  $\phi_n$  needs to be subtracted from  $-\pi/2$ , which then has to be divided by the angular frequency of the fitted tidal component (thus  $U(t_{HW}) = (-\pi/2 - \phi_n)/\omega_n$ ).

A harmonic analysis can also be carried out on salinity values. Using this method, it is possible to obtain salinity amplitudes and phases of the different tidal constituents. Also this procedure is nearly identical to the harmonic analysis of the water levels, only here salinity values are used as input. Just like with the harmonic fit of the water level, the phase of the salinity is determined when the salinity reaches its maximum value. To obtain the time of max salinity, the calculated phase  $\phi_n$  needs to be subtracted from  $\pi/2$ , which then has to be divided by the angular frequency of the fitted tidal component.

For the harmonic analysis, a total of four tidal components were fitted to the water level and velocity data at different locations in the grid. These are the  $M_2$  (which is prescribed at the seaward boundary),  $O_1$ ,  $M_4$  and  $M_6$  components. The harmonic analysis showed that the  $M_2$  component is by far the most important tidal component in the grid for the water level, tidal velocities and salinity. As expected, the  $O_1$  tidal component is not present in the entire basin whilst the  $M_4$  and  $M_6$  components show negligible amplitudes. The phase of the water level, tidal velocities and salinity in the two channels downstream of the tidal junction is not the same. This becomes evident when analysing the fitted tidal characteristics of the two channels downstream of the tidal junction.

Fig. 5.1 and Fig. 5.2 show the calculated  $M_2$  water level amplitudes for both channels at different distances downstream from the tidal junction. It is clear that the water level amplitude at the mouth of both channels is not the same for different lengths of channel 1. This is a result of radiation damping (interaction of tide in estuary and tide at sea), which occurs because the tidal amplitude is prescribed not directly at the channel mouth but 20 km offshore. Another clear observation is that the tidal amplitude in channel 1 increases with increasing channel lengths. Only when the length of channel 1 is increased to over 60 km, different behaviour is observed near the tidal junction. The amplitudes of both the 80 and 100 km simulations decrease drastically near the tidal junction. On the other hand, the amplitudes of the 80 and 100 km simulations show a distinct peak approximately 30 km downstream of the tidal junction. This is the effect of resonance. The amplitudes in channel 2 show different behaviour. Most simulations show a small increase in tidal amplitude towards the tidal junction, only the 80 and 100 km simulations show a different pattern. In these simulations, the tidal amplitude shows a minimum around 8 km downstream of the tidal junction after which the amplitude increases again until reaching the tidal junction.

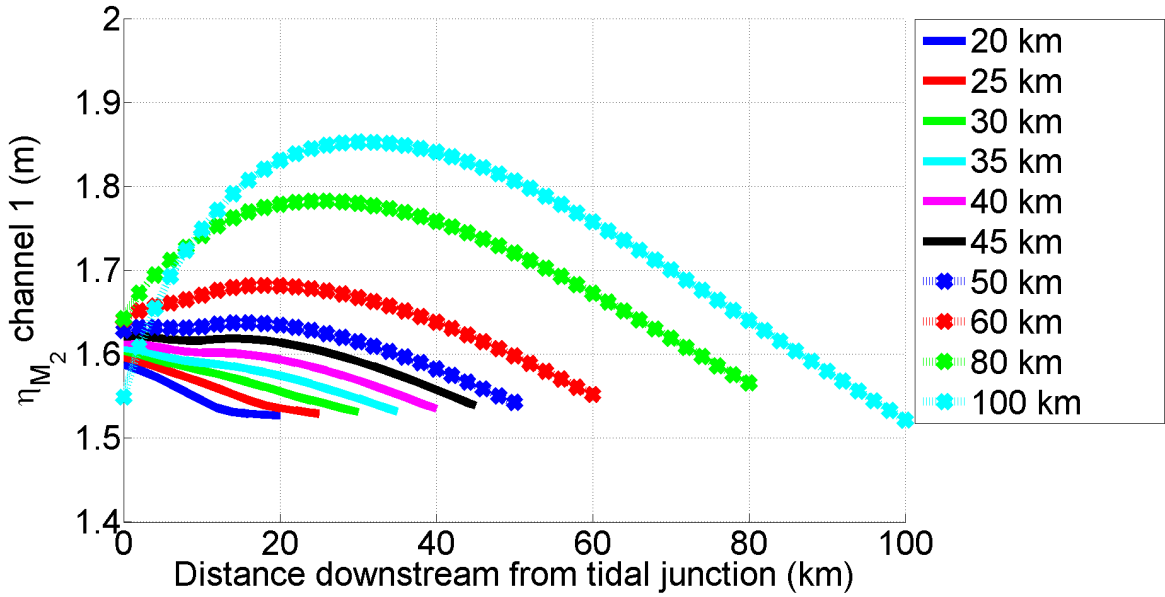


Fig. 5.1:  $M_2$  water level amplitudes ( $\eta_{M_2}$ ) for channel 1 at different locations downstream of the tidal junction. The colours denote the simulations with the different channel lengths.

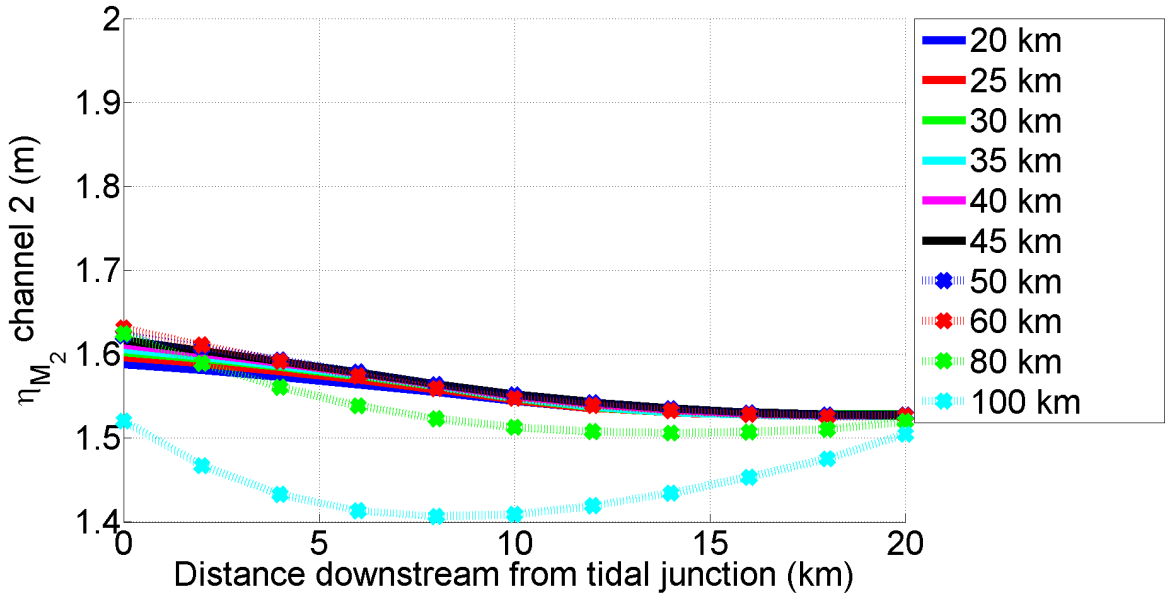


Fig. 5.2:  $M_2$  water level amplitudes ( $\eta_{M_2}$ ) for channel 2 at different locations downstream of the tidal junction. The colours denote the simulations with the different channel lengths.

To analyse the behaviour of the tidal wave, it is possible to compute the phase and investigate the phase difference between channel 1 and channel 2. Fig. 5.3 shows the  $M_2$  water level phase ( $\phi_{\eta_{M_2}}$ ) difference (in hours) between channel 1 and channel 2 for the different simulations in the first 20 km downstream of the tidal junction. It is evident that the phase difference downstream from the tidal junction increases if channel 1 gets longer. If both channels are similar in length, the phase difference at all locations is nearly zero. As soon as the difference in length between both channels increases, the phase difference downstream from the tidal junction also increases. At the tidal junction, the phase difference is nearly 0 for all lengths (Fig. 5.4). This means that there is hardly any spatial water level variation at the junction for the different channel lengths.



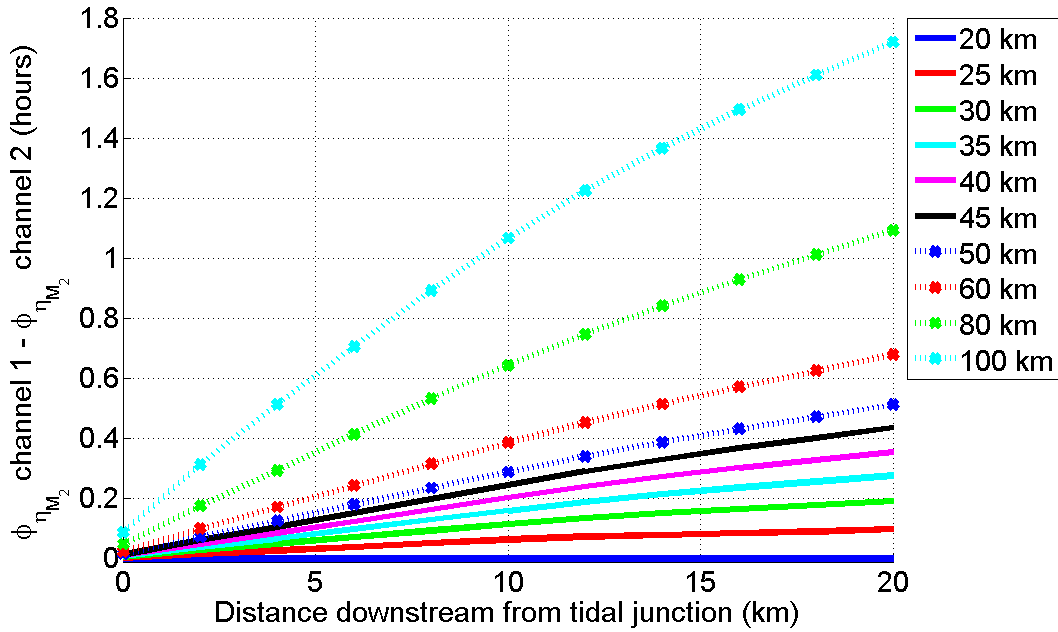


Fig. 5.3: Difference in  $M_2$  water level phase ( $\phi_{\eta_{M_2}}$ ) between channel 1 and channel 2 (in hours) plotted as a function of the distance downstream from the tidal junction. Colours indicate the different lengths of channel 1.

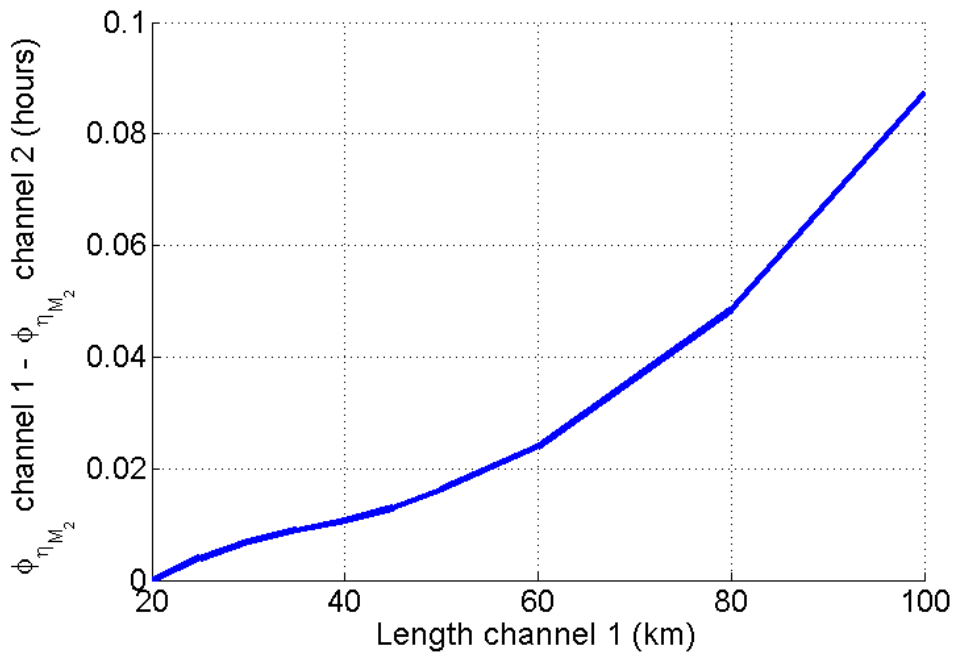


Fig. 5.4: Difference in  $M_2$  water level phase ( $\phi_{\eta_{M_2}}$ ) between channel 1 and channel 2 (in hours) at the tidal junction. Shown are the phase differences at the tidal junction for different lengths of channel 1.

Fig. 5.5 and Fig. 5.6 show the calculated cross-sectionally averaged  $U_{M_2}$  tidal velocity amplitudes for channel 1 and channel 2 at different distances downstream from the tidal junction. It is clear that the tidal velocity amplitude in channel 1 decreases with increasing channel lengths. Only when the length of channel 1 is increased to over 60 km, different behaviour is observed near the tidal junction. The tidal velocity amplitudes of both the 80 and 100 km simulations increase considerably towards the tidal junction but they show a trough around 20-30 km downstream of the tidal junction. This is not observed in channel 2. Here, all simulations show a monotonic increase in tidal velocity with increasing channel length. Also interesting is the distinct drop in velocity amplitude near the tidal junction for all channel lengths.

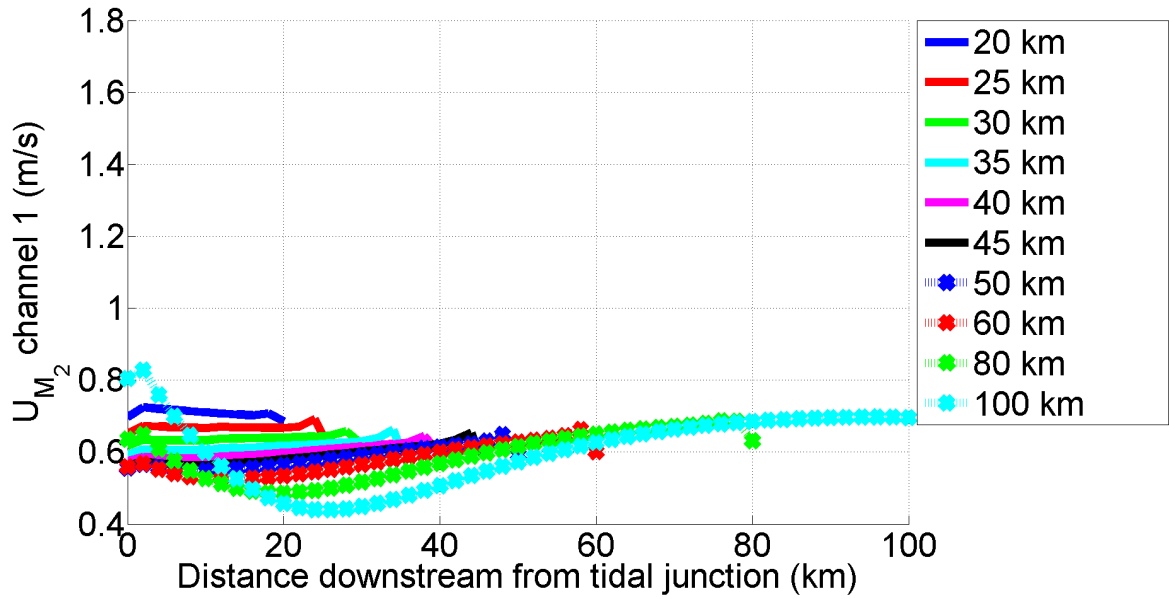


Fig. 5.5: Cross-sectionally averaged  $M_2$  velocity amplitudes ( $U_{M_2}$ ) at various locations downstream of the tidal junction for channel 1. The colours indicate the simulations with the various channel lengths.

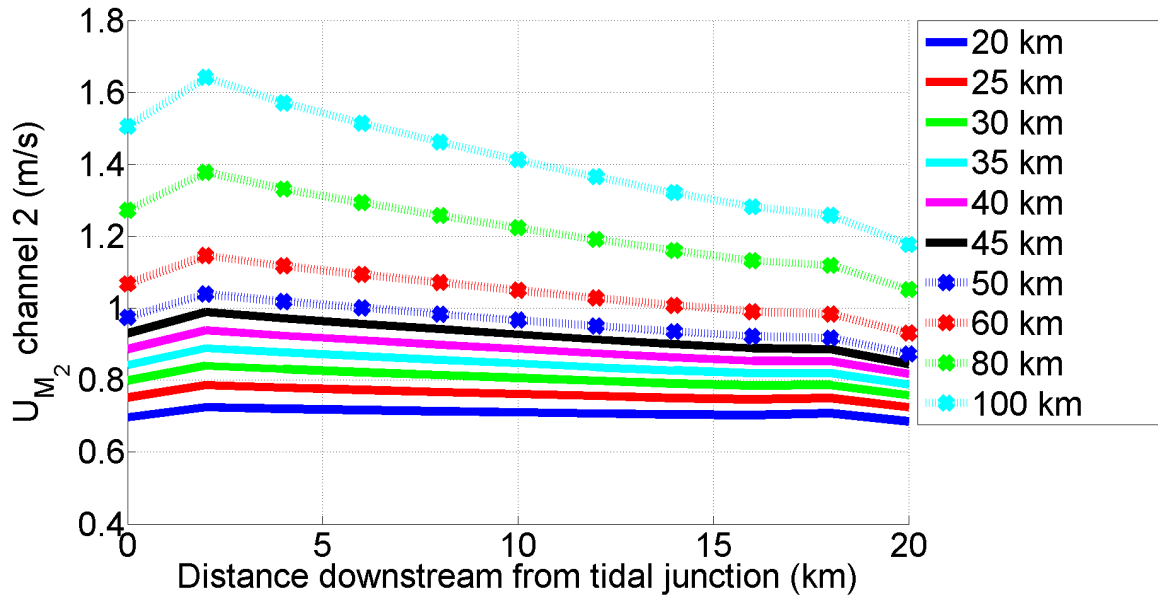


Fig. 5.6: Cross-sectionally averaged  $M_2$  velocity amplitudes ( $U_{M_2}$ ) at various locations downstream of the tidal junction for channel 2. The colours indicate the simulations with the various channel lengths.

A phase difference plot can also be produced for the fitted tidal velocities. Fig. 5.7 shows the  $M_2$  tidal velocity amplitude phase ( $\phi_{UM_2}$ ) difference between both channels (in hours) as a function of different locations downstream of the tidal junction. It is clear that in comparison with the differences in  $\phi_{\eta M_2}$  (Figure 5.3), the differences in  $\phi_{UM_2}$  at the tidal junction increase drastically with increasing channel length. This is further demonstrated in Fig. 5.8, which shows the difference in  $\phi_{UM_2}$  at the junction. Clearly, the difference in  $\phi_{UM_2}$  increases linearly with increasing channel length to arrive at over 4 hours for the 100 km simulation.

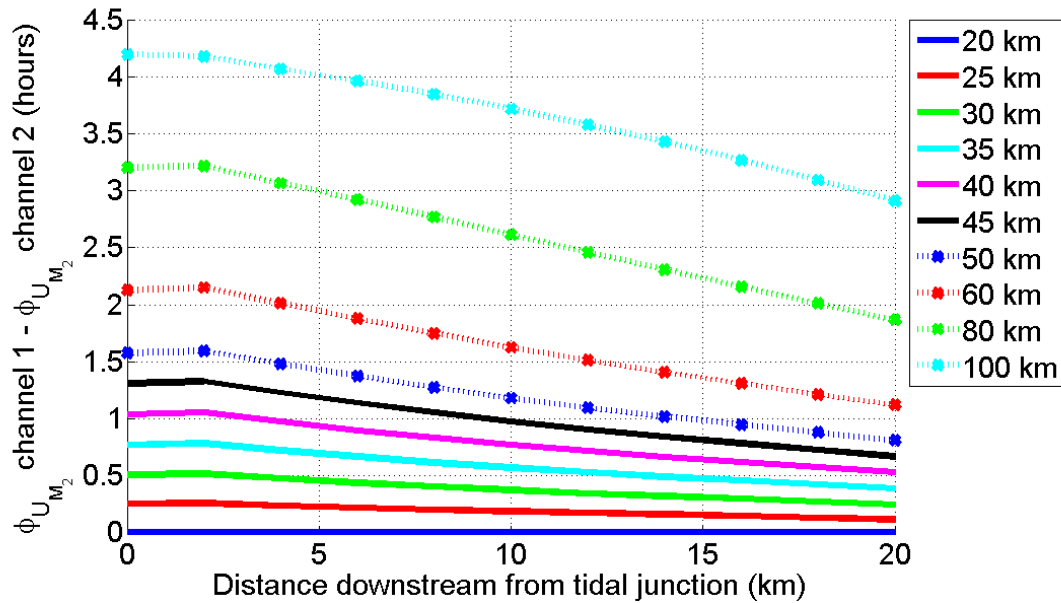


Fig. 5.7: Difference in  $M_2$  velocity phase ( $\phi_{UM_2}$ ) between channel 1 and channel 2 (in hours) plotted as a function of the distance downstream of the tidal junction. The colours indicate the different lengths of channel 1.

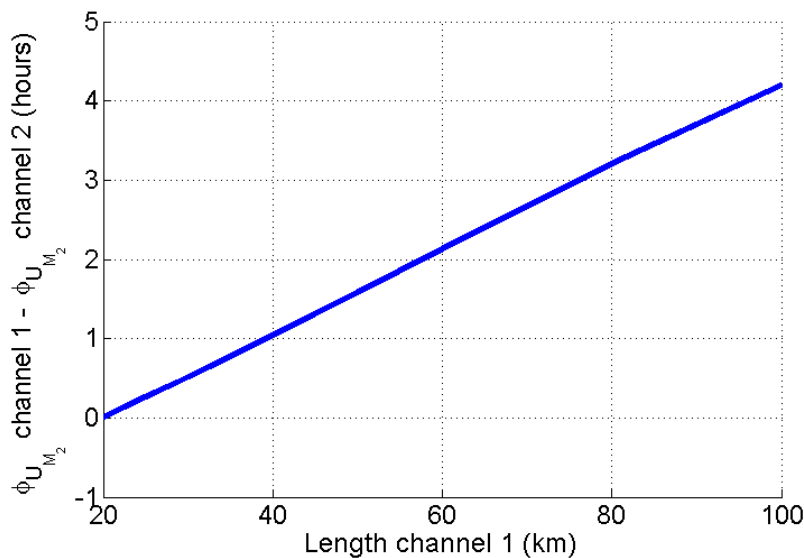


Fig. 5.8: Difference in  $M_2$  velocity phase ( $\phi_{UM_2}$ ) between channel 1 and channel 2 (in hours) at the tidal junction. Shown are the phase differences at the tidal junction for different lengths of channel 1.

To obtain more information about the character of the tidal wave inside the basin, the relative phase difference between the  $M_2$  tidal water level and  $M_2$  tidal velocity is calculated. In straight estuaries with no reflection (friction length scale  $\ll$  estuary length), the tidal wave will have a progressive character. This means that low or high tide occurs at different points in time along the estuary. For an ideal (frictionless) progressive wave, the phase lag between the tidal velocity and tidal water level will be either  $0^\circ$  or  $360^\circ$  (which is 0 or 12.5 hours for the  $M_2$  tide). In other words, the largest flood and ebb velocities will occur around high tide and low tide, whilst slack water occurs between high and low tide. When the tidal wave experiences friction or gets reflected, a standing wave will develop. In that case, high water in the basin occurs at every position in the basin at the same moment. The phase lag between tidal velocity and tidal water level will then be plus or minus ( $\pm$ )  $90^\circ$  (which is  $\pm 3.1$  hours for the  $M_2$  tide). When the phase difference is  $\pm 45^\circ$  ( $\pm 1.5$  hours for the  $M_2$  component), the wave is a propagating wave (friction length scale  $\ll$  channel length, tidal wavelength). In rare

cases, a tidal wave can still be propagating, despite the phase difference between water level and velocity being  $90^\circ$ . This only happens in long, shallow, funnel-shaped estuaries (Friedrichs, 2010).

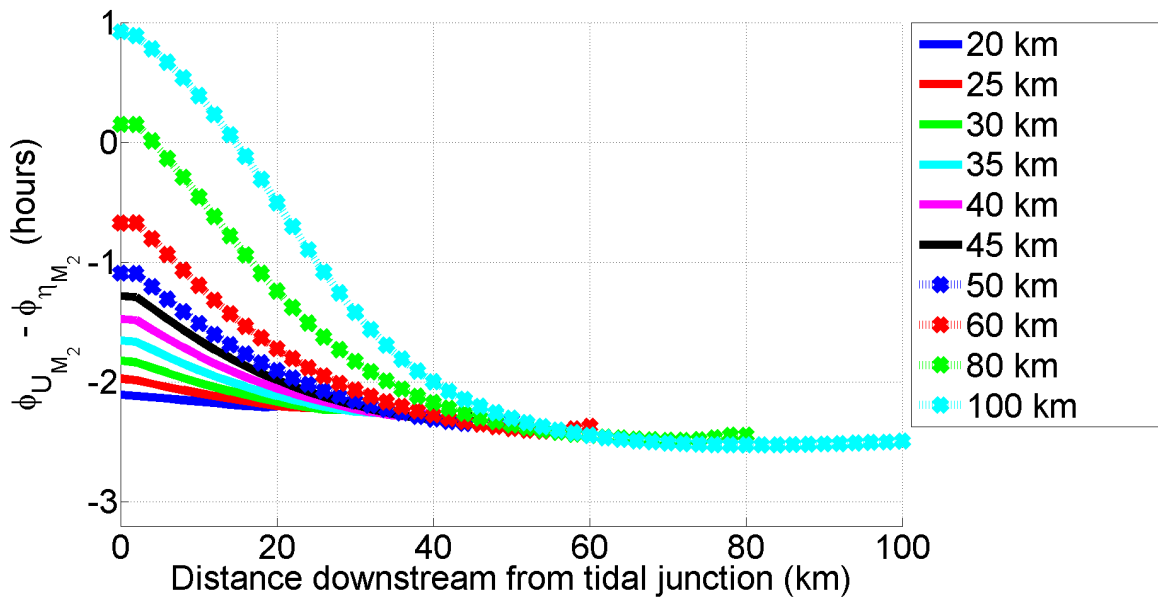


Fig. 5.9: Relative phase difference between  $\phi_{UM_2}$  and  $\phi_{\eta M_2}$  for channel 1 as a function of different locations downstream from the tidal junction. The colours indicate the simulations with different lengths of channel 1.

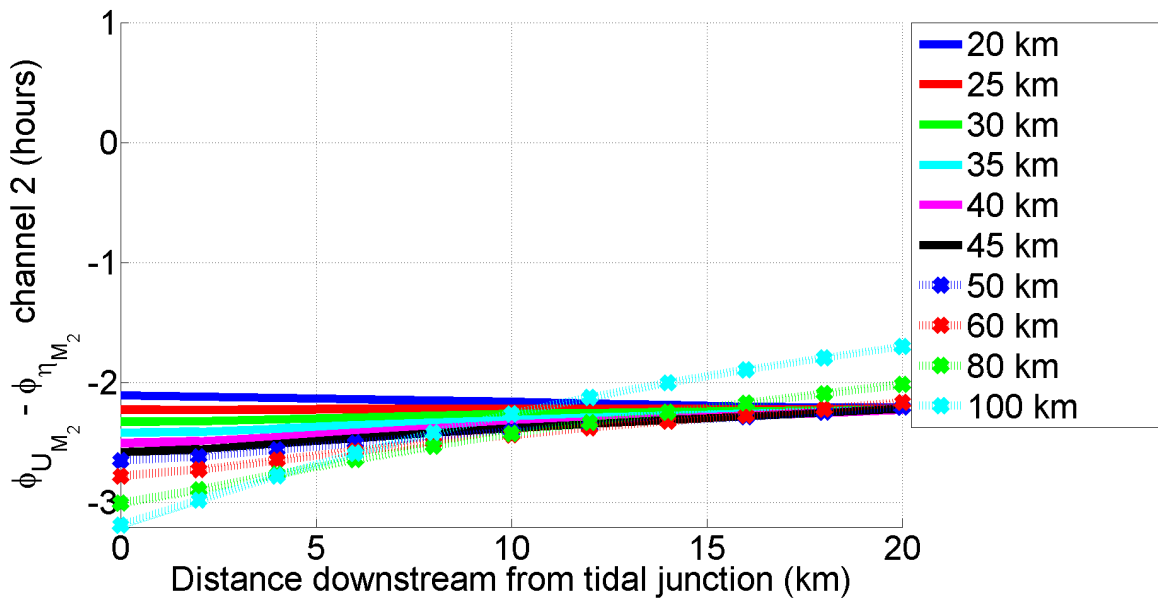


Fig. 5.10: Relative phase difference between  $\phi_{UM_2}$  and  $\phi_{\eta M_2}$  for channel 2 as a function of different locations downstream from the tidal junction. The colours indicate the simulations with different lengths of channel 1.

Fig. 5.9 and Fig. 5.10 show the relative phase differences in channel 1 and channel 2 at various locations downstream from the tidal junction. It is clear that the tidal wave in both channels has a different character. The character of the tidal wave in channel 1 changes drastically as soon as the length of channel 1 is increased. For the 100 km simulation, the relative phase difference in channel 1 approaches +1 hour at the tidal junction. In other words, the water level is at some point ahead of the tidal velocities. This indicates that wave comes from upstream, suggesting that the tidal wave from channel 2 enters channel 1. At the same time, the relative phase difference in channel 2 is -3 hours. The relative phase difference in channel 1 shows a propagating wave pattern that gets even more evident when channel 1 gets

longer. This is also observed in channel 2, where for small channel lengths, the relative phase difference is nearly constant. When the length of channel 1 is increased, a propagating wave develops (especially for the 80 and 100 km case).

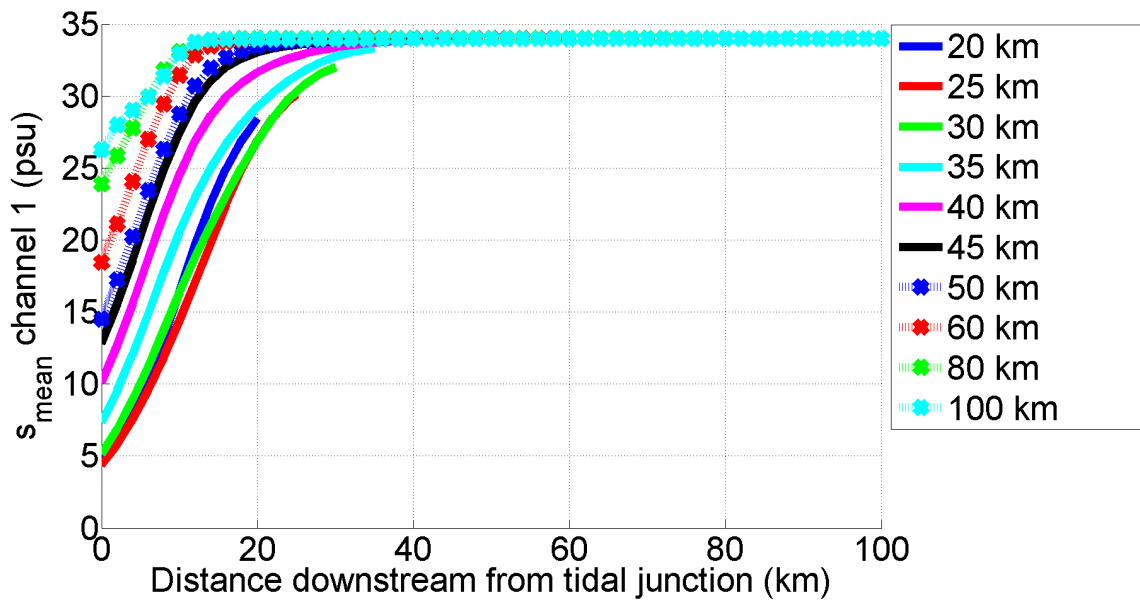


Fig. 5.11: Tidally- and cross-sectionally averaged salinity amplitude ( $s_{mean}$ ) at various locations downstream of the tidal junction for channel 1. The colours indicate the different lengths of channel 1.

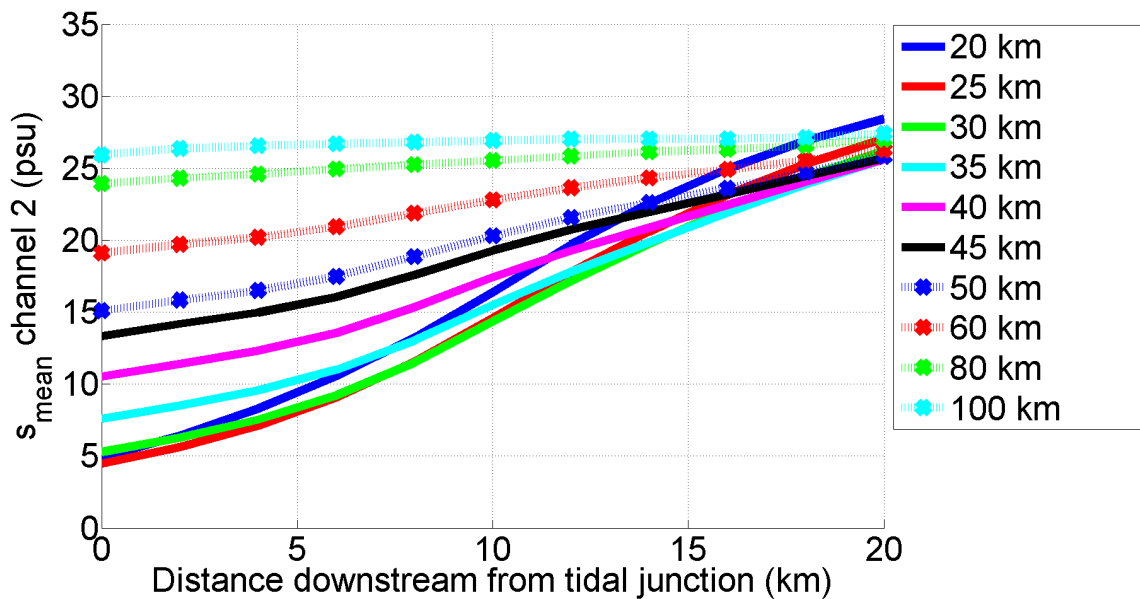


Fig. 5.12: Tidally- and cross-sectionally averaged salinity amplitude ( $s_{mean}$ ) at various locations downstream of the tidal junction in channel 2. The colours indicate the different lengths of channel 1.

Fig. 5.11 and Fig. 5.12 show the mean salinity amplitude (averaged over the cross-section and tidal period) in channel 1 and channel 2. A drastic increase in mean salinity is observed in both channels when the length of channel 1 is increased. However, substantial differences occur between both channels. For a longer channel 1 (above 40 km), the mean salinity in a section of channel 1 reaches the salinity prescribed at the seaward boundary (34 psu). The length of this section of constant salinity increases when the length of channel 1 is increased. For the case that channel 1 is 100 km long, only the 10 km just downstream of the junction show a mean salinity that is not equal to 34 psu. The mean salinity in channel 2 also increases considerably when the length of channel 1 is increased. However, the mean salinity never

reaches the salinity prescribed at sea (mean salinity is always below 30 psu for all lengths of channel 1). The largest increase in mean salinity is observed in the section closest to the tidal junction. The mean salinity at the mouth of channel 2 only changes slightly for different lengths of channel 1.

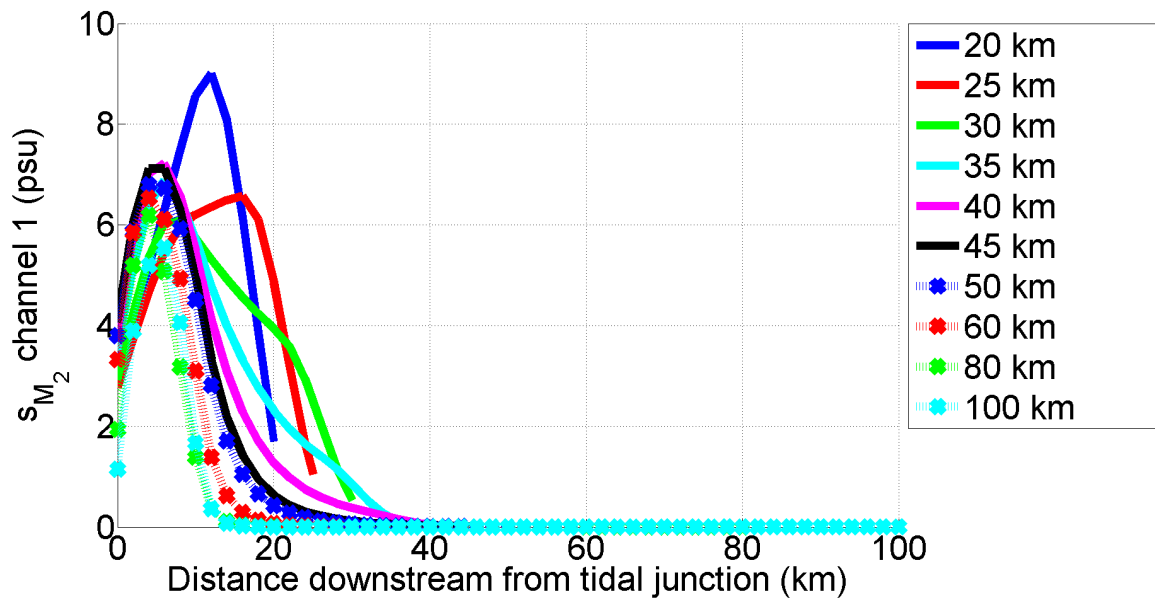


Fig. 5.13: Cross-sectionally averaged  $M_2$  tidal salinity amplitudes ( $s_{M_2}$ ) at various locations downstream of the tidal junction for channel 1. The colours indicate the simulations with the various channel lengths.

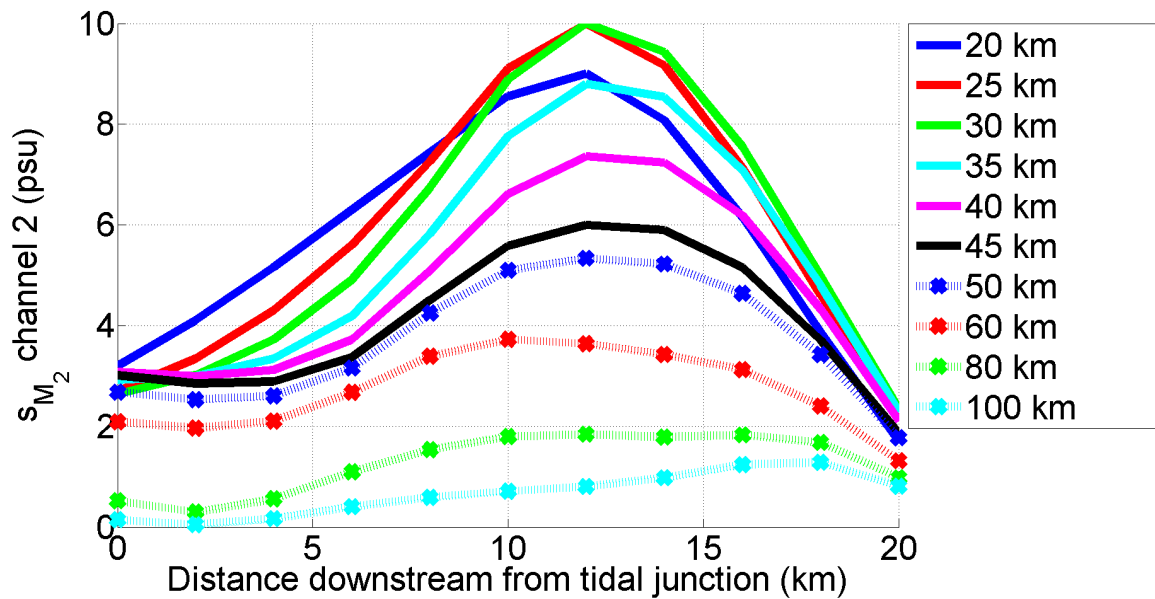


Fig. 5.14: Cross-sectionally averaged  $M_2$  tidal salinity amplitudes ( $s_{M_2}$ ) at various locations downstream of the tidal junction for channel 2. The colours indicate the simulations with the various channel lengths.

Fig. 5.13 and Fig. 5.14 show the cross-sectionally averaged  $M_2$  tidal salinity amplitude ( $s_{M_2}$ ) in channel 1 and channel 2. It is clear that in channel 1, the largest  $M_2$  salinity amplitude occurs for the smallest channel length (20 km). Moreover, the largest amplitude is reached in a distinct peak, which is located somewhere halfway between the junction and the sea. A steady decrease in  $M_2$  salinity amplitude is observed when increasing the length of channel 1. In a large part of the longer channels, the  $M_2$  salinity amplitude is close to zero. This suggests that there is no tidal salinity fluctuation in this part of the channel and salinity is therefore constant. This is consistent with the observations in Fig. 5.11, which shows a constant mean

salinity in a large part of channel 1 when the length of channel 1 exceeds 40 km. The  $M_2$  tidal salinity amplitudes in channel 2 show a different pattern. Still, the highest amplitudes are observed for the shorter channel lengths, but the largest amplitude is now observed for the 30 km case and not for the 20 km case. The largest amplitude is again observed more or less halfway the junction and the sea. When increasing the length of channel 1 to 35 km and beyond, the  $M_2$  tidal salinity amplitudes drop quickly, just like those in channel 1.

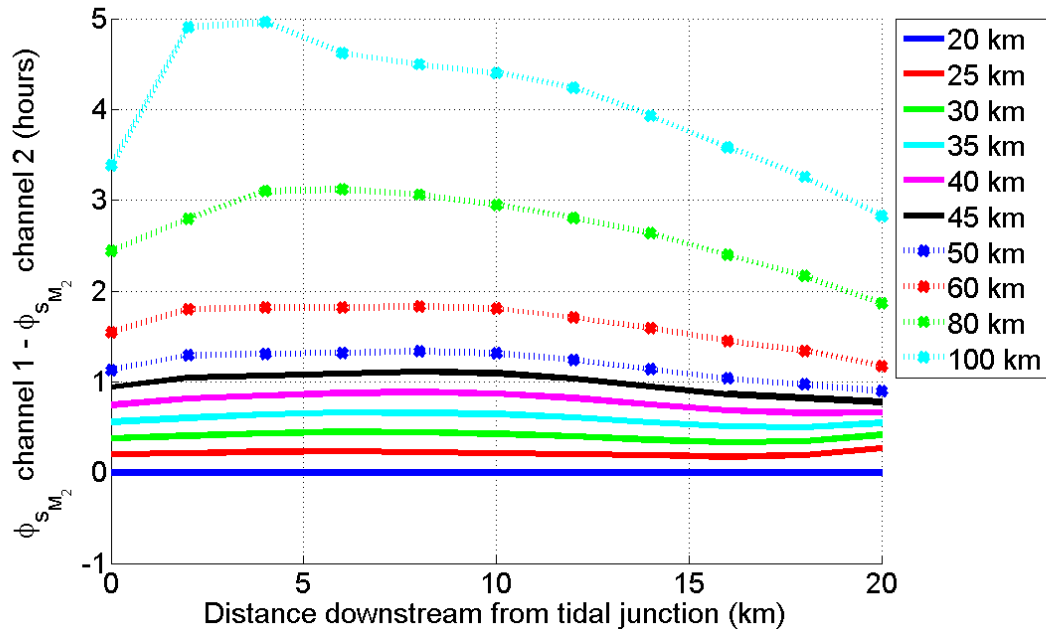


Fig. 5.15:  $M_2$  salinity phase ( $\phi_{sM_2}$ ) difference between channel 1 and channel 2 (in hours) plotted as a function of the distance downstream of the tidal junction. The colours indicate the different lengths of channel 1.

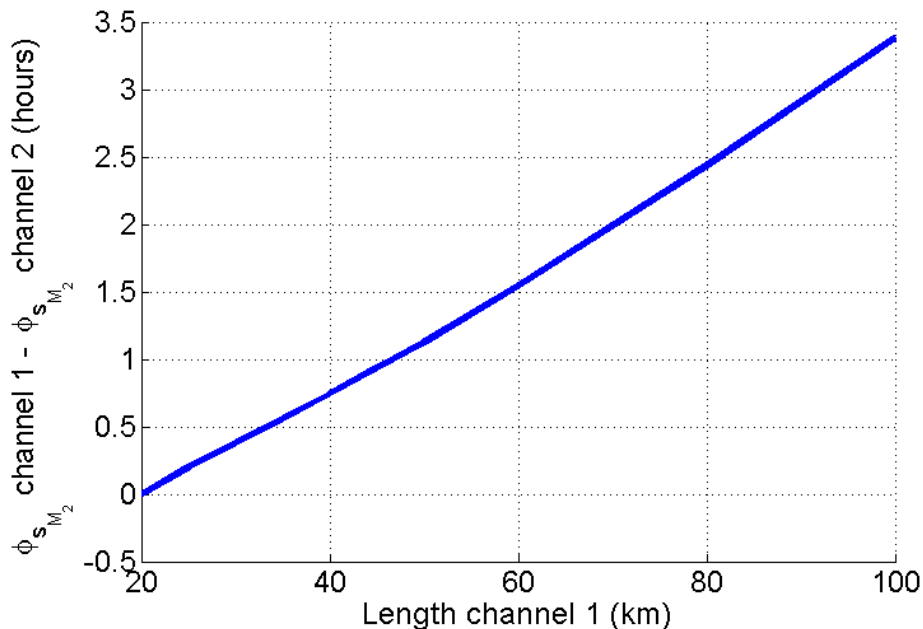


Fig. 5.16: Calculated salinity phase ( $\phi_{sM_2}$ ) differences (in hours) between channel 1 and channel 2 at the tidal junction. Shown are the phase differences at the tidal junction for different lengths of channel 1.

Fig. 5.15 shows the difference in  $\phi_{sM_2}$  (in hours) between both channels as a function of different locations downstream of the tidal junction. For small channel lengths, the phase difference is relatively constant along the channel. This changes when the length of channel 1

is larger than 50 km. In this case, the phase difference increases in the channel and shows a distinct peak. The largest phase difference is observed approximately 4 km downstream of the tidal junction for the 100 km simulation (5 hours). At the junction itself, the phase difference increases linearly (Figure 5.16). For the 100 km case, the salinity phase difference at the junction is nearly 3.5 hours.

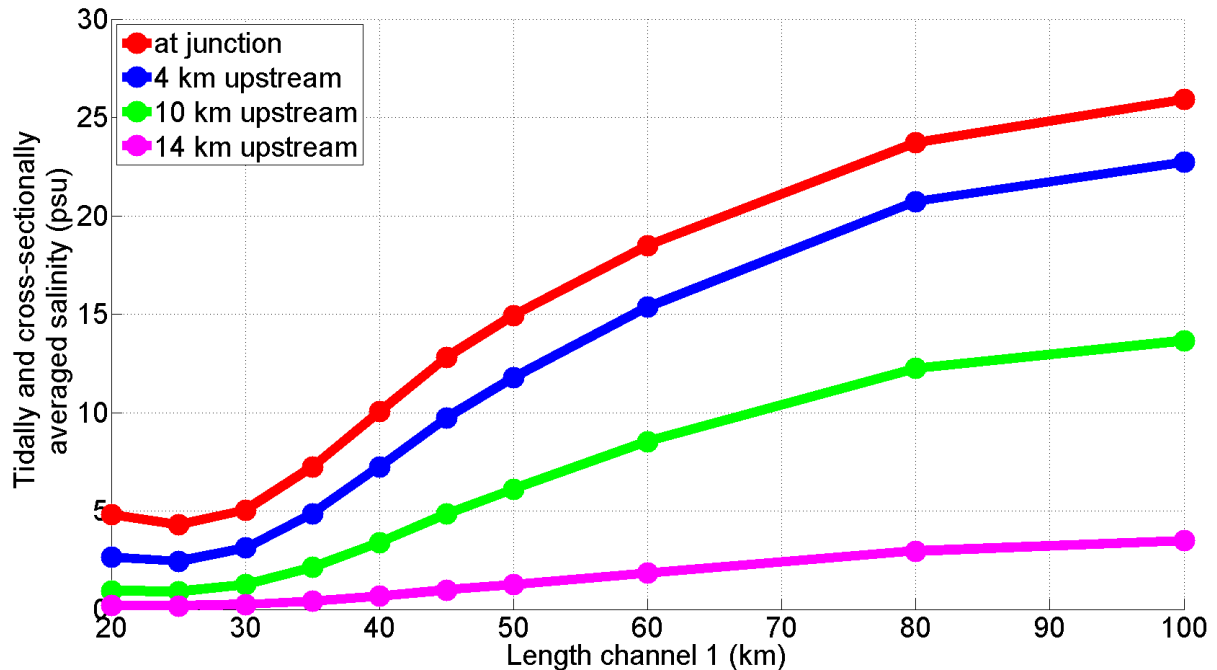


Fig. 5.17: Tidally and cross-sectionally averaged salinity versus the length of channel 1. Shown are the salinity values at four locations upstream of the junction.

### **5.3 Salinity distribution and intrusion length**

The tidally- and cross-sectionally averaged salinity values is denoted as  $\langle \bar{S} \rangle$ , where the  $\langle \rangle$  denote a tidal average, the overbar denotes a depth average and the underbar denotes a width-average. Fig. 5.17 shows  $\langle \bar{S} \rangle$  as a function of the length of channel 1 at a few locations upstream of the tidal junction. Clearly, the salinity values increase constantly when the length of channel 1 is increased. When computing the intrusion length upstream of the junction for the different simulations, the same pattern is observed (Fig. 5.18). Here, the intrusion length is defined as the distance between the tidal junction and the first location where the tidally- and cross-sectionally averaged salinity is less than 1 psu. The mean salinity is computed by averaging over width, depth and the tidal period. It is observed that the intrusion length increases drastically as soon as channel 1 becomes longer than channel 2. For example, when channel 1 has a length of 80 km, the intrusion length is more than two times as large compared to the case when channel 1 is 20 km long. When the length of channel 1 is increased to 100 km, the intrusion length becomes even larger. A small drop in intrusion length is observed when channel 1 is set to a length of 25 km. After that, the intrusion length increases constantly when the length of channel 1 is increased. It is evident that after 50 km, the intrusion length starts to level off and seems to approach a maximum value which is approximately 24 km.



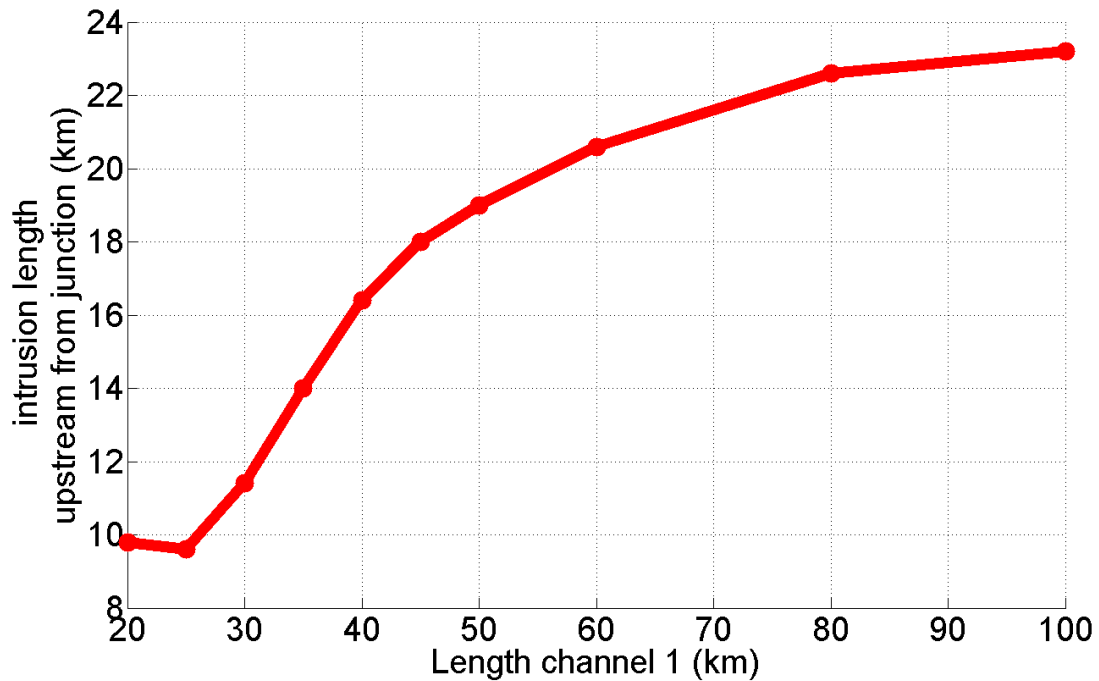


Fig. 5.18: Intrusion length, defined as the distance between the tidal junction and the location where the tidally- and cross-sectionally averaged salinity is less than 1 psu, versus the length of channel 1.

The salinity distribution in the different simulations has been investigated in different ways. First of all, contour plots of the tidally and width-averaged salinity were produced for the 50 km upstream of the tidal junction and both channels downstream of the tidal junction. The contour plot for the upstream part (Fig. 5.19), clearly shows that the tidally and width-averaged salinity increases for increasing channel lengths. This confirms the observations with regards to the intrusion length (Fig. 5.18), which also reveals an increase when channel 1 is longer. Another observation is that the salinity patterns mostly show a constant salinity for the entire depth. This is particularly the case in the simulations with a relative short channel 1. For the simulations with a longer channel 1 (particularly the 80 and 100 km case), the contours of constant salinity are no longer entirely vertical. However, the vertical density gradient is still very small, so it seems justified so say that the water column is still well-mixed.

The contour plot for channel 1 (Fig. 5.20) shows a different structure compared to the upstream contour plot. Most noticeably, the tidally and width-averaged salinity increases drastically for a larger length of channel 1 in the downstream part. For a longer channel 1 (when the length of channel 1 exceeds 40 km), the tidally and width-averaged salinity in a downstream part of channel 1 reaches the salinity prescribed at sea (34 psu). The distance over which the salinity in channel 1 is equal to the salinity prescribed at sea increases for a longer channel 1. For example, when channel 1 is 80 km long, only the first 10 km downstream of the tidal junction show a salinity value that is not equal to 34 psu. The same holds for the 100 km case. The vertical structure in all the simulations shows the same pattern as for the upstream part. For a shorter length of channel 1, the salinity contours are nearly vertical. For a longer channel 1 (starting at 40 km), a slight vertical density gradient is present. Still, the water column seems to be well-mixed.

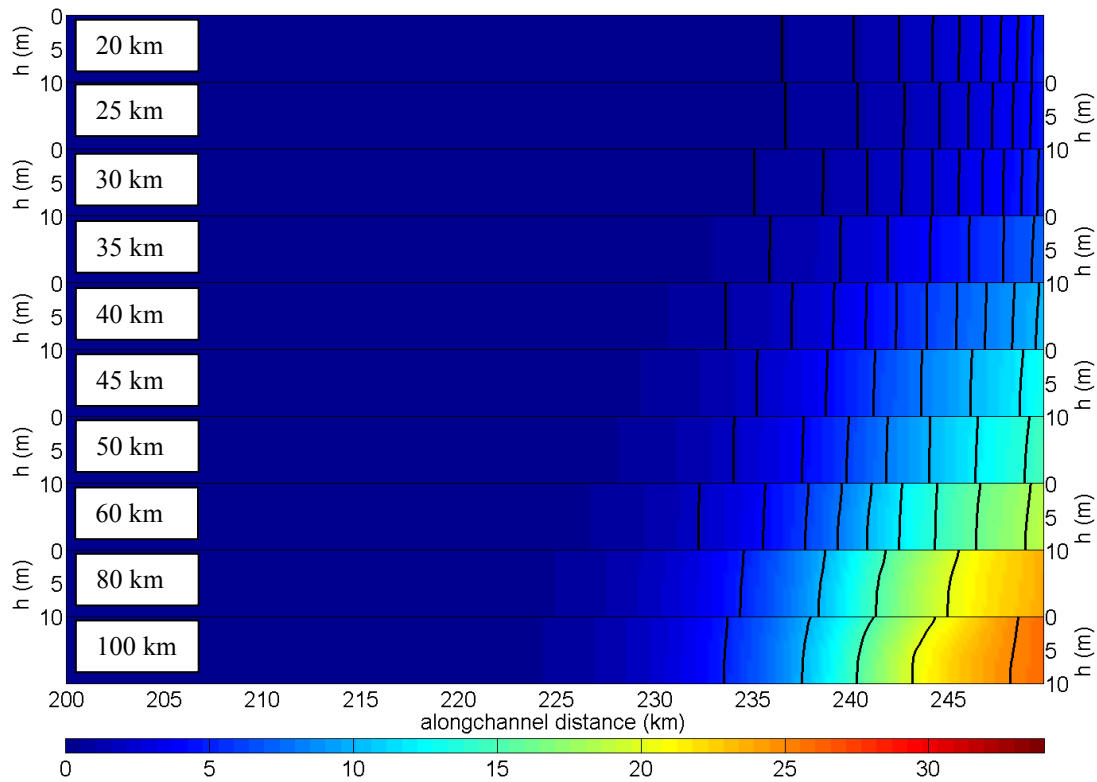


Fig. 5.19: Contour plot showing the tidally- and width-averaged salinity (psu) for all vertical layers. Here, the values for all simulations in the 50 km just upstream of the tidal junction are displayed. The upper panel shows the salinity structure for channel 1 = 20 km, whilst the panels below that show the salinity for the cases in which the length of channel 1 is increased stepwise to 100 km (lowest panel). The tidal junction is located at 250 km.

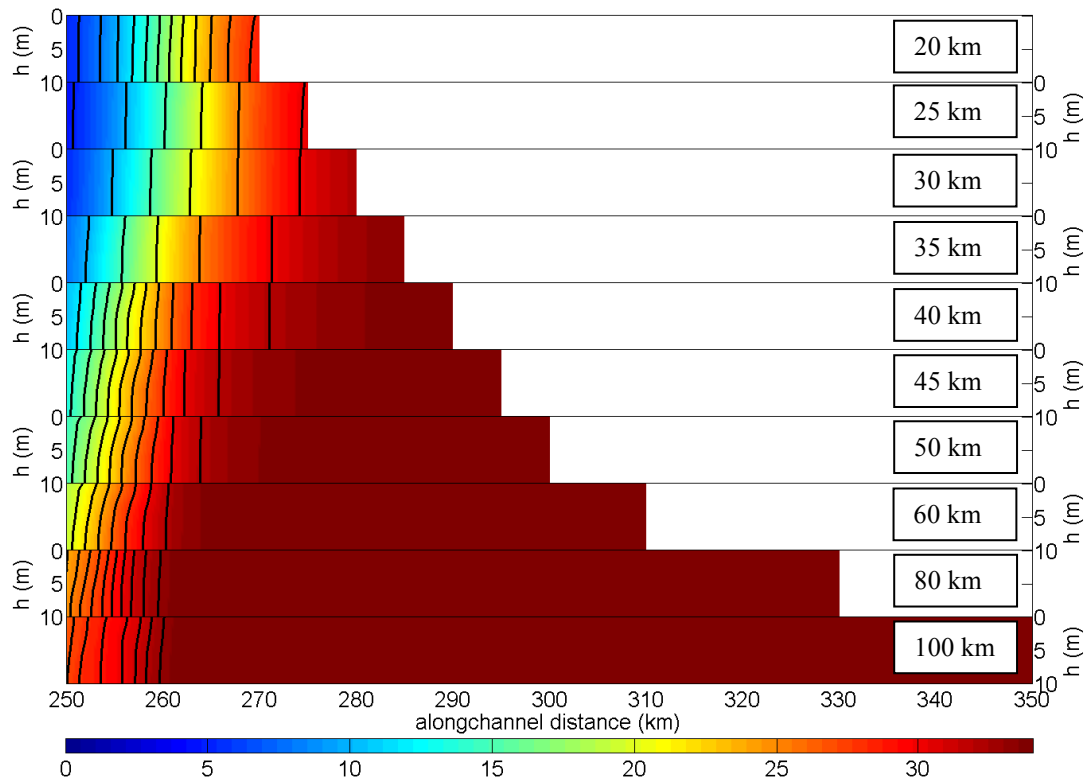


Fig. 5.20: Contour plot showing the tidally- and width-averaged salinity (psu) for all vertical layers. Here, the values for all simulations in channel 1 are displayed. The upper panel shows the salinity structure for channel 1 = 20 km, whilst the panels below that show the salinity for the cases in which the length of channel 1 is increased stepwise to 100 km (lowest panel). The tidal junction is located at 250 km.

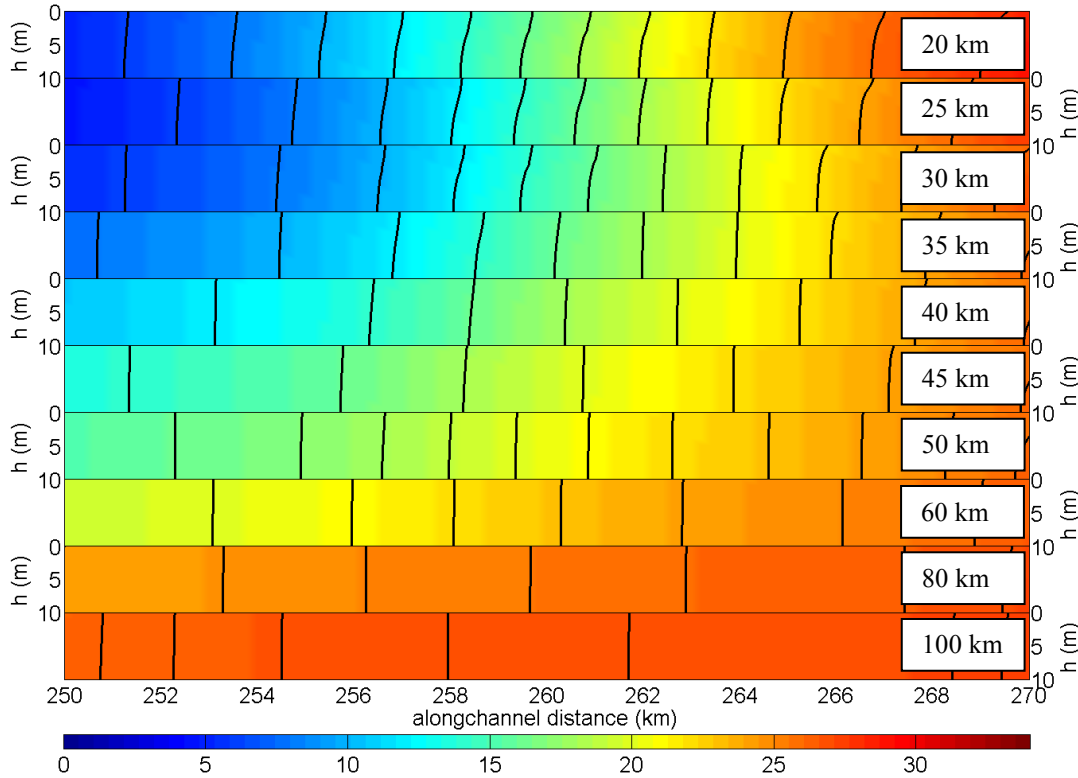


Fig. 5.21: Contour plot showing the tidally- and width-averaged salinity (psu) for all vertical layers. Here, the values for all simulations in channel 2 are displayed. The upper panel shows the salinity structure for channel 1 = 20 km, whilst the panels below that show the salinity structure for the cases in which the length of channel 1 is increased stepwise to 100 km (lowest panel). The tidal junction is located at 250 km.

The contour plot for channel 2 (Fig. 5.21), clearly shows that the tidally and width-averaged salinity values are completely different compared to that in channel 1. First of all, the salinity values in channel 2 are much lower compared to channel 1. Secondly, the salinity in the downstream part decreases when increasing the length of channel 1 from 20 to 35 km. Only if the length of channel 1 is increased to 40 km and beyond, the tidally and width-averaged salinity in channel 2 starts to increase. Thirdly, the vertical structure shows the opposite behaviour of that in the upstream part and channel 1. In channel 2, the salinity contours are nearly vertical for the cases that channel 1 is long (45 km and beyond). Interestingly, the salinity contours of channel 2 in the cases that channel 1 is short (between 20 and 45 km), show the presence of a slight vertical density gradient. This is contrary to the observations in the upstream part and channel 1. Still, there seems to be little stratification.

The degree of stratification can be examined in more detail by defining a stratification parameter. This parameter can be defined as (Hansen & Rattray, 1966; Dyer, 1997)

$$\sigma = \frac{\langle S_{bot} \rangle - \langle S_{top} \rangle}{\langle \bar{S} \rangle}, \quad (\text{Eq. 5.7})$$

in which  $\sigma$  is the stratification parameter (-),  $\langle S_{top} \rangle$  is the tidally and width-averaged salinity of the top layer (psu),  $\langle S_{bot} \rangle$  is the tidally and width-averaged salinity of the bottom layer (psu) and  $\langle \bar{S} \rangle$  is the tidally- and cross-sectionally averaged salinity (psu). It is generally accepted that when  $\sigma < 0.1$ , the water column is well-mixed (Savenije, 2012).

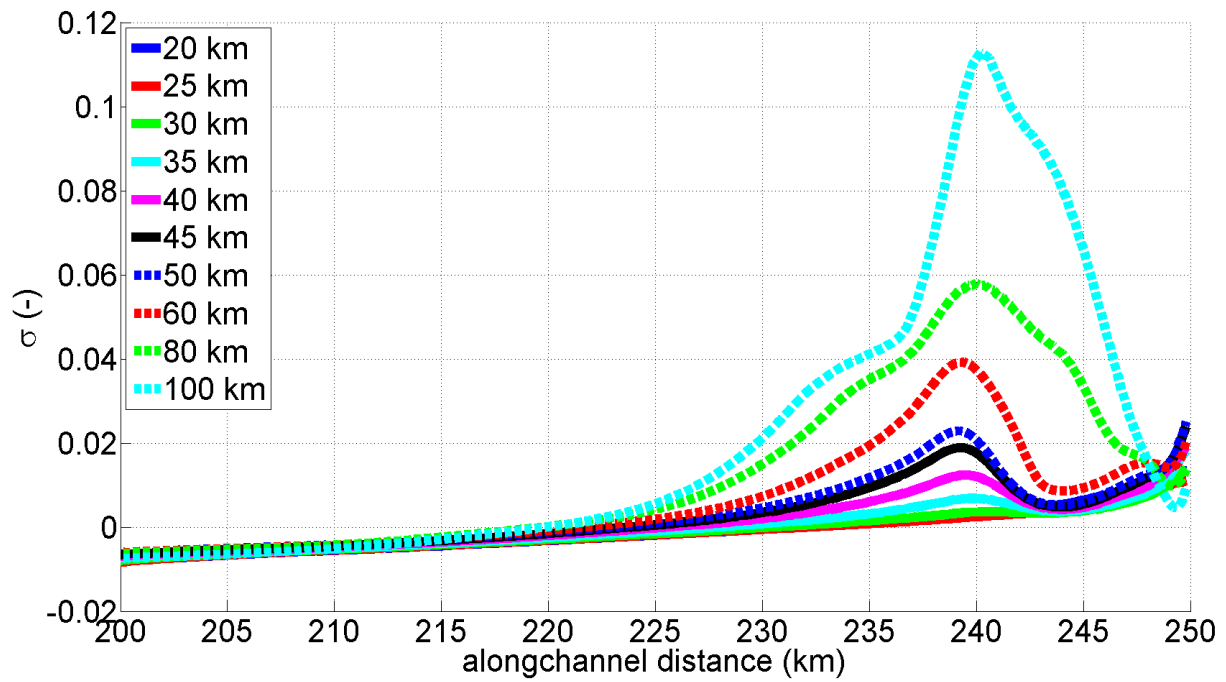


Fig. 5.22: Stratification parameter  $\sigma$  for all simulations in the 50 km section just upstream of the tidal junction. The colours denote the different lengths of channel 1. The tidal junction is located at 250 km.

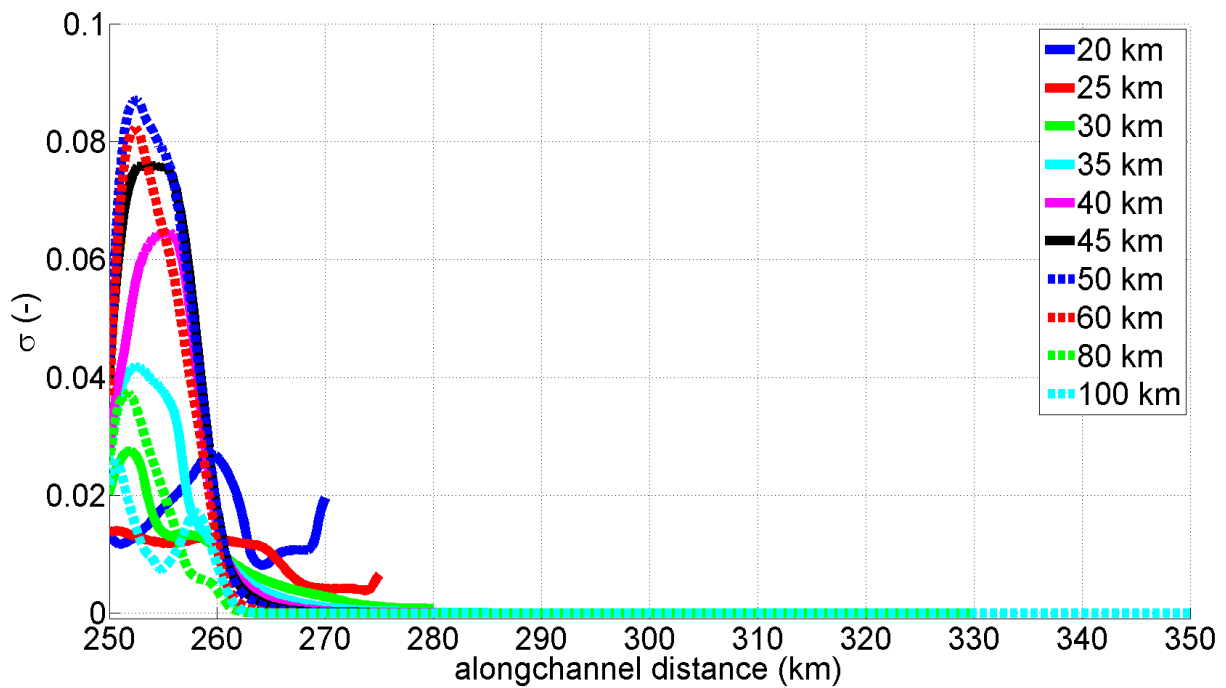


Fig. 5.23: Stratification parameter  $\sigma$  for all simulations in channel 1. The colours denote the different lengths of channel 1 and the tidal junction is located at 250 km.

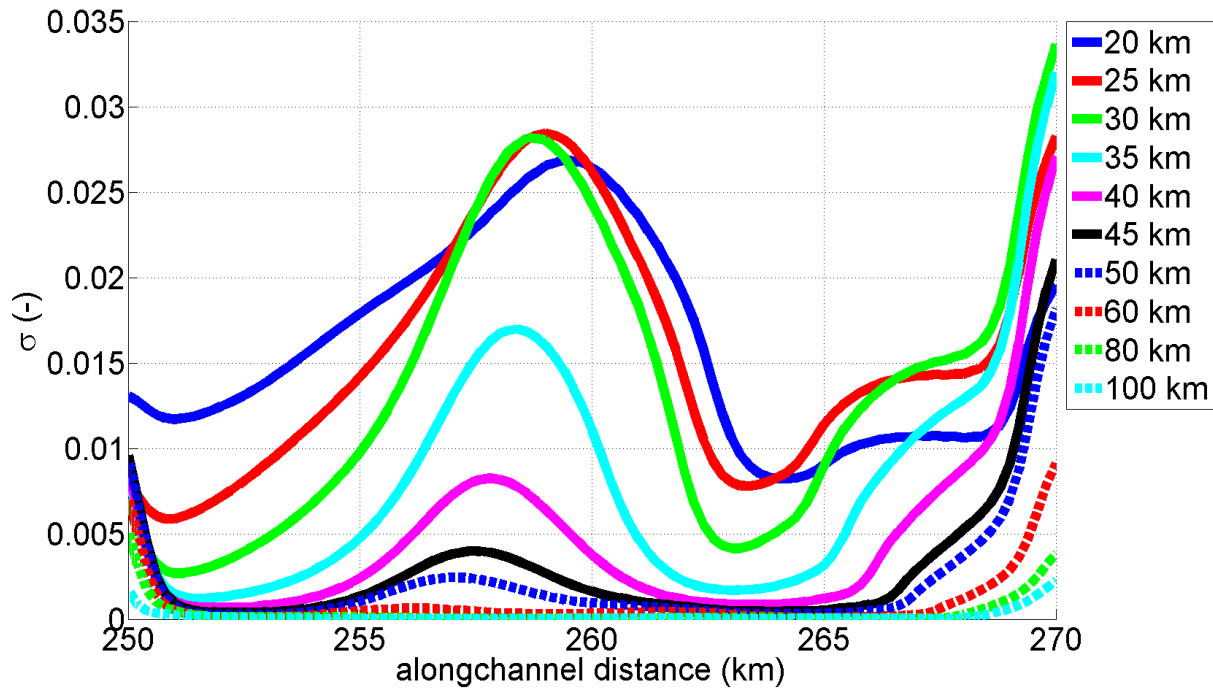


Fig. 5.24: Stratification parameter  $\sigma$  for all simulations in channel 2. The colours denote the different lengths of channel 1 and the tidal junction is located at 250 km.

The stratification pattern of the different simulations has been studied in the same way as the salinity distribution. The stratification pattern confirms the pattern shown in the along-channel contour plots. Fig. 5.22 shows the stratification parameter  $\sigma$  for all simulations in the 50 km section just upstream of the tidal junction. It is observed that  $\sigma$  is close to zero in the entire section for the cases when channel 1 is short (less than 40 km). For a longer channel 1,  $\sigma$  increases in the 20 km long section just upstream of the junction. The largest value ( $\sigma = 0.11$ ) is reached 10 km upstream of the tidal junction when channel 1 is 100 km long. This is in agreement with salinity contours that are plotted in Fig. 5.19. Here, the largest vertical salinity variation is also observed in the first 10 km upstream of the tidal junction for the case that channel 1 is 100 km long.

The stratification parameter  $\sigma$  for all the simulations in channel 1 (Fig. 5.23), shows that  $\sigma$  is largest near the tidal junction. If channel 1 equals 20 km,  $\sigma$  is largest 10 km downstream of the tidal junction. When channel 1 equals 25 km,  $\sigma$  is nearly 0 throughout the entire channel. After that,  $\sigma$  starts to increase (particularly near the tidal junction). It reaches a max value of approximately 0.09. The largest  $\sigma$  value is reached when channel 1 is 50-60 km long. If the length of channel 1 is further increased,  $\sigma$  decreases again. For the case that channel 1 is 100 km long,  $\sigma$  is again close to zero throughout the entire channel.

The stratification parameter  $\sigma$  for all the simulations in channel 2 is displayed in Fig. 5.24. The pattern is again different from that seen in the upstream section and channel 1. The largest  $\sigma$  values are now seen 8-9 km downstream of the tidal junction and at the channel mouth. The largest values for  $\sigma$  are observed when channel 1 is 20-30 km long. When the length of channel 1 exceeds 30 km,  $\sigma$  decreases steadily. For the cases that channel 1 is longer than 50 km,  $\sigma$  is close to zero in the entire channel. Only at the channel mouth,  $\sigma$  still increases slightly.

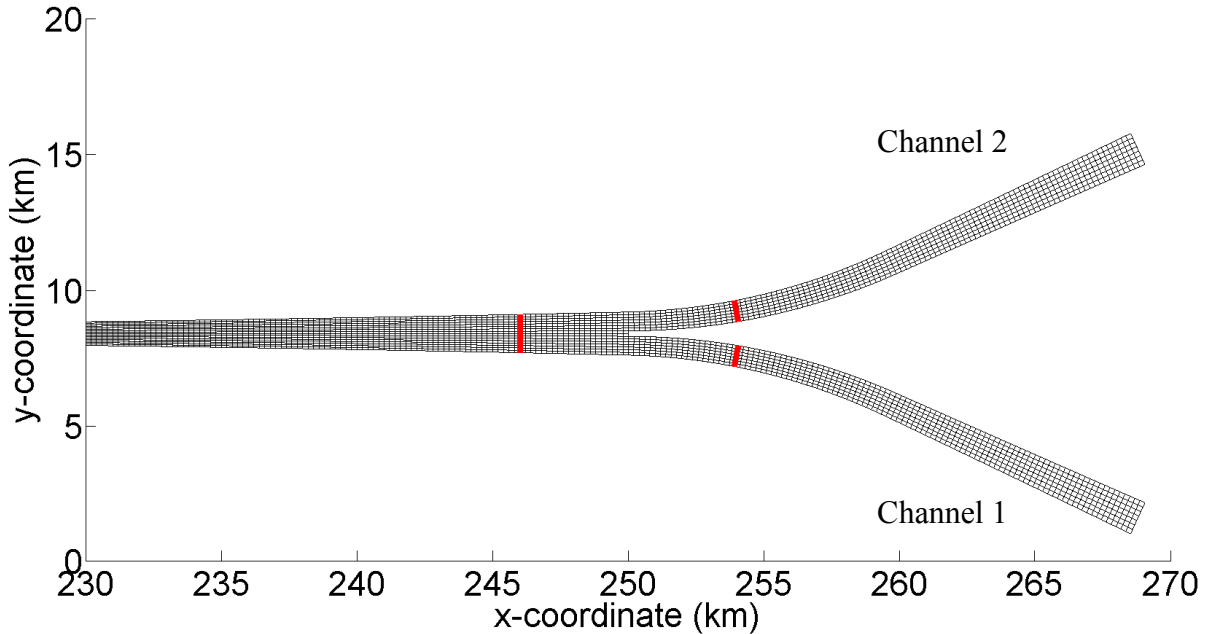


Fig. 5.25: Overview of the cross-sections in the grid (displayed in red), in this case for the 20 km version. In the simulations with a longer channel 1, the monitored cross-sections are situated at the same locations.

Apart from the previously illustrated along-channel salt profiles, it is also interesting to consider cross-sectional contour plots. A total of three cross-sections were defined in the grid (Fig. 5.25). In both channels seaward of the junction, a monitoring cross-section was defined 4 km downstream of the tidal junction. Apart from that, a monitoring cross-section was also defined 4 km upstream of the tidal junction. Fig. 5.26 shows contour plots of the tidally-averaged salinity  $\langle S \rangle$ , the tidally-averaged along-channel velocity  $\langle u \rangle$  and the  $U_{M2}$  amplitude for the cross-section located 4 km upstream of the tidal junction. On top of that, the tidally-averaged lateral velocity  $\langle v \rangle$  is plotted as vectors. The results are shown for the simulations in which channel 1 equals 20 km and 50 km. It is clear that the water column is well-mixed in the symmetric (20 km) simulation, as the salinity difference between the upper and lower layer is in the order of 0.025 psu. For the 20-50 km simulation, the salinity differences are larger (in the order of 0.5 psu). Here, a lateral salinity gradient is present, with the saltiest water located in the extension of branch 2.

The tidally-averaged along-channel velocity for the symmetric simulation shows a normal velocity profile, with the largest velocities located in the top of the water column and the lower velocities located near the bed. In the 20-50 km simulation, more or less the same pattern can be observed with larger velocities in the top of the water column and lower velocities near the bed. The only difference is that the velocities in the left part of the cross-section are larger compared to the right part of the cross-section. This seems to be related to the salinity of the water. Larger along-channel velocities are observed in water with lower salinity. The smallest velocities are observed in water with the highest salinity. The lateral velocity vectors indicate that there is hardly any lateral flow in the symmetric case, with flow velocities in the order  $0.1 \text{ mm s}^{-1}$ . However, for the 20-50 km simulation, the vertical velocities are in the order of  $1 \text{ cm s}^{-1}$ , and a lateral circulation can be distinguished. Finally, the tidal velocity amplitudes are largest in the top of the water column and lowest near the bed. As the largest flow velocities are located high up in the water column, this is a logical result.

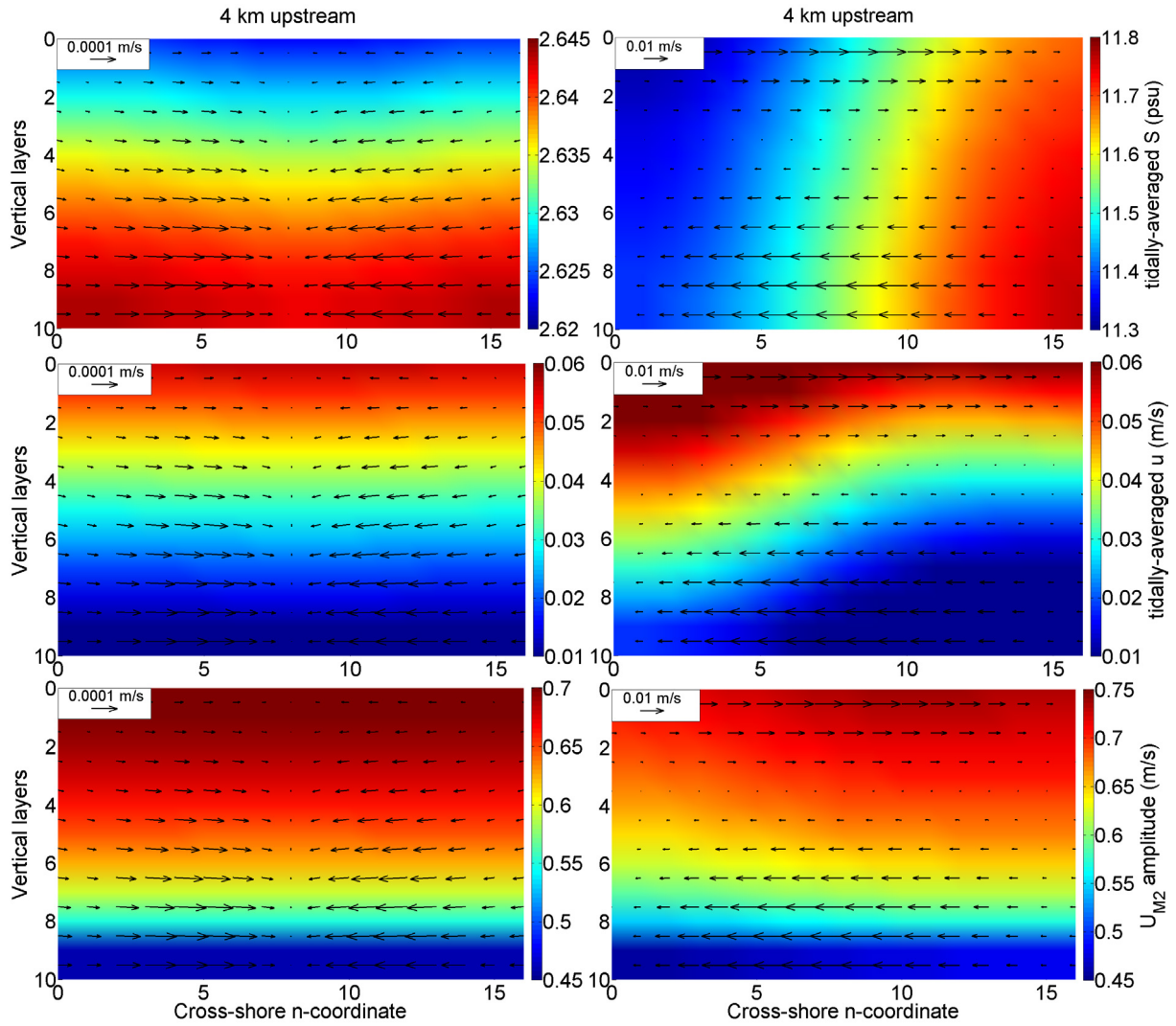


Fig. 5.26: Cross-sectional contour plots of the tidally-averaged salinity  $\langle S \rangle$  (top), tidally-averaged along-channel velocity  $\langle u \rangle$  (middle) and the  $U_{M2}$  amplitude (bottom) located 4 km upstream of the tidal junction. The arrows indicate the tidally-averaged lateral velocity  $\langle v \rangle$ . The left figures show the symmetric situation (both channels 20 km long), whilst the right figures show the situation with channel 1 being 50 km long. The cross-shore n-coordinates 1-7 are located in the continuation of channel 1 and n-coordinates 9-16 are located in the continuation of channel 2.

Fig. 5.27 shows contour plots of the tidally-averaged salinity  $\langle S \rangle$ , the tidally-averaged along-channel velocity  $\langle u \rangle$  and the  $U_{M2}$  amplitude for the two cross-sections located 4 km downstream of the tidal junction. On top of that, the tidally-averaged lateral velocity  $\langle v \rangle$  is plotted. Again, two different simulations are shown (20-20 and 20-50 km). In the symmetric case, both channels show the same pattern for all displayed variables. Regarding the salinity, the lowest salinity values are situated in the top of the water column. The largest salinity values are situated in the bottom of the water column. As saltier water is denser, this is a stable distribution. The salinity values for the 20-50 km simulation show that channel 1 has a far higher salinity value compared to channel 2. This is due to the fact that all freshwater discharge is concentrated in the shorter channel 2, resulting in hardly any resistance for salt intrusion in channel 1.



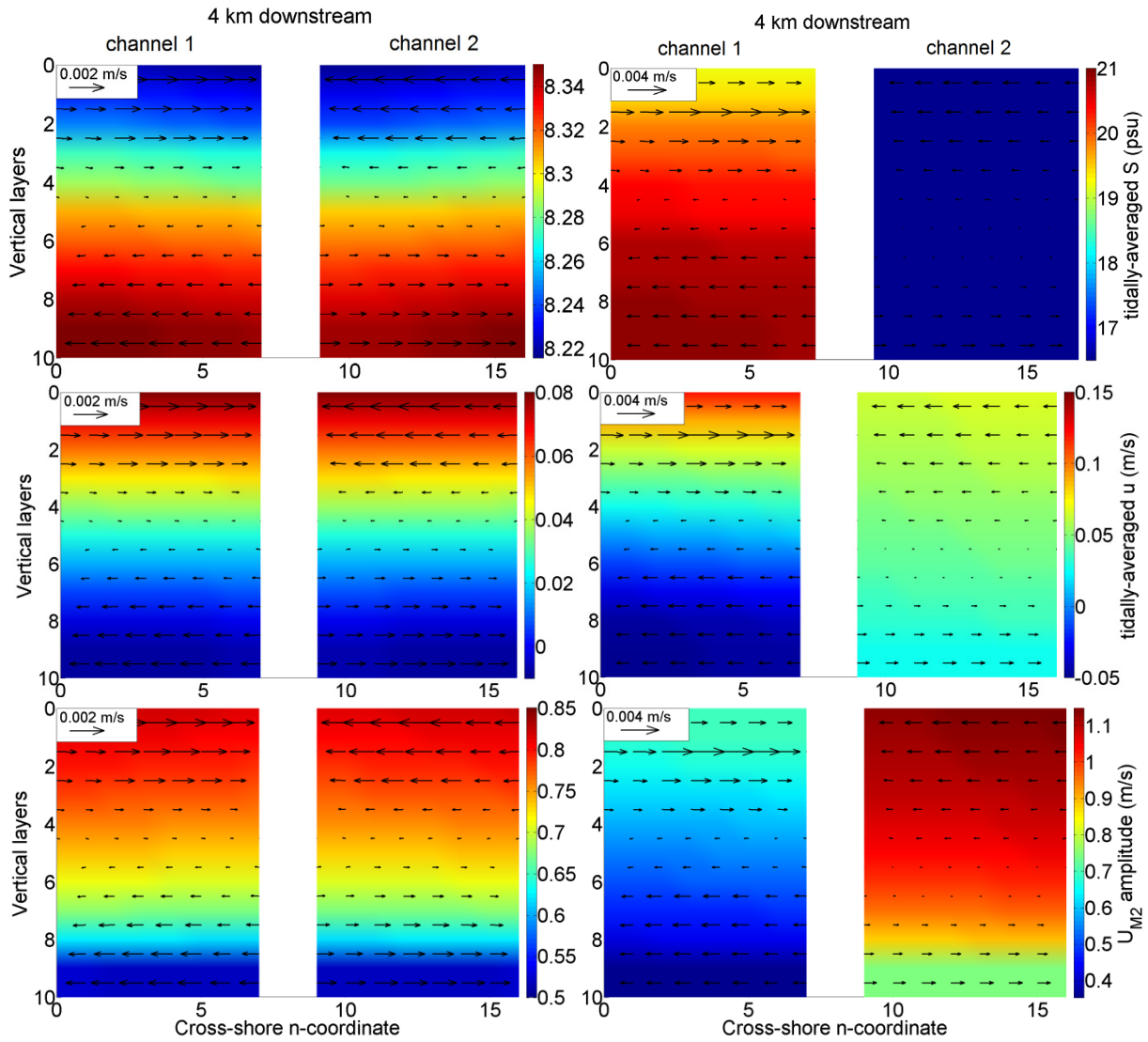


Fig. 5.27: Cross-sectional contour plots of the tidally-averaged salinity  $\langle S \rangle$  (top), tidally-averaged along-channel velocity  $\langle u \rangle$  (middle) and the  $U_{M2}$  amplitude (bottom) located 4 km downstream of the tidal junction. The arrows indicate the tidally-averaged lateral velocity  $\langle v \rangle$ . The left figures show the symmetric situation (both channels 20 km long), whilst the right figures show the situation with channel 1 being 50 km long. The n-coordinates 1-7 are located in channel 1 and n-coordinates 9-16 are located in channel 2.

Also in the downstream section, the tidally-averaged along-channel velocity for the symmetric simulation shows a normal velocity profile. The largest velocities are located in the top of the water column and the lower velocities are located near the bed. In the 20-50 km simulation, a similar pattern can be observed for channel 2. The tidally-averaged velocity for channel 1 is completely different compared to channel 2. Here, a two-layer system seems to be present. Near the bottom, a negative (thus upstream) along-channel velocity is present, which turns positive (thus downstream) higher up the water column. Averaged over the water column, the resulting along-channel velocity will be close to zero. Both channels also show a small lateral circulation pattern as appears from the velocity vectors. The tidal amplitudes in channel 1 are much lower than those in channel 2, but they show the same expected pattern. Lower amplitudes are observed near the bottom and larger amplitudes in the top of the water column.



## 5.4 Salt transport

To get a better understanding of the salinity patterns that have been shown in the previous section, a detailed analysis of the different transport terms was carried out. These transport terms were analysed at the same cross-sections (Fig 5.25) as those used to produce Fig. 5.26 and Fig. 5.27. As is shown in Table 5.1, Delft3D calculates a number of transport terms directly. Using these terms, it is possible to compute a number of other transport terms. Together, these transport terms quantify the contributions of different drivers for the total transport of water and salt for the various simulations. Firstly, a short description of the different transport terms will be given. After that, different transport terms will be analysed in detail.

The total (cumulative) discharge through the cross-sections (called  $Q_{cum}$ ) is defined as

$$Q_{cum} = \iiint_{t_0}^{t_0+T} u \, dy \, dz \, dt \quad (\text{in m}^3). \quad (\text{Eq. 5.8})$$

When taking the time-derivative of the total discharge, the instantaneous discharge through cross section (called  $Q_{inst}$ ) is obtained, which is defined as

$$Q_{inst} = \iint u \, dy \, dz \quad (\text{in m}^3/\text{s}). \quad (\text{Eq. 5.9})$$

Apart from water transport, Delft3D also computes the salt transport terms. These salt transport terms are separated in advective and dispersive terms. The cumulative advective salinity transport through the cross-sections ( $Q_{cum\_salt\_adv}$ ) is computed as

$$Q_{cum\_salt\_adv} = \iiint_{t_0}^{t_0+T} uS \, dy \, dz \, dt \quad (\text{in psu m}^3). \quad (\text{Eq. 5.10})$$

When taking the time-derivative of the cumulative advective salinity transport, the advective salinity transport through the cross-sections is obtained ( $Q_{salt\_adv}$ )

$$Q_{salt\_adv} = \iint uS \, dy \, dz \quad (\text{in psu m}^3/\text{s}). \quad (\text{Eq. 5.11})$$

Delft3D also computes the cumulative dispersive salinity transport through the cross-sections ( $Q_{cum\_salt\_disp}$ ), which is defined as

$$Q_{cum\_salt\_disp} = - \iiint K_x \frac{\partial S}{\partial x} \, dy \, dz \, dt \quad (\text{in psu m}^3). \quad (\text{Eq. 5.12})$$

Taking the time-derivative of the cumulative dispersive salt transport result in the dispersive salinity transport through the cross-sections ( $Q_{salt\_disp}$ )

$$Q_{salt\_disp} = - \iint K_x \frac{dS}{dx} \, dy \, dz \quad (\text{in psu m}^3/\text{s}). \quad (\text{Eq. 5.13})$$

It is also possible to write the salt transport terms as freshwater transport terms. This is possible for both the advective and the dispersive transport component. The advective freshwater transport through the cross-sections ( $Q_{fresh\_adv}$ ) can be defined as

$$Q_{fresh\_adv} = \iint uf \, dy \, dz, \quad \text{with} \quad f = 1 - \frac{S}{S_0}. \quad (\text{Eq. 5.14})$$

Another way to write this is

$$Q_{fresh\_adv} = Q_{inst} - (Q_{salt\_adv}/S_0) \quad (\text{in } \text{m}^3 \text{ s}^{-1}). \quad (\text{Eq. 5.15})$$

Applying the same method to the dispersive freshwater component is also possible. This leads to the dispersive freshwater transport through the cross-section ( $Q_{fresh\_adv}$ )

$$Q_{fresh\_disp} = - \iint K_x \frac{df}{dx} dy dz, \quad \text{with } f = 1 - \frac{S}{S_0}. \quad (\text{Eq. 5.16})$$

This can be written as

$$Q_{fresh\_disp} = \frac{1}{S_0} \iint K_x \frac{\partial S}{\partial x} dy dz, \quad (\text{Eq. 5.17})$$

which ultimately leads to:

$$Q_{fresh\_disp} = -Q_{salt\_disp}/S_0 \quad (\text{in } \text{m}^3 \text{ s}^{-1}). \quad (\text{Eq. 5.18})$$

In the above equations,  $u$  is the flow velocity ( $\text{m s}^{-1}$ ),  $x$  is the along-channel coordinate (m, positive when moving downstream),  $y$  is the cross-channel coordinate (m),  $z$  is the vertical coordinate (m, positive downwards),  $t$  is time (s),  $t_0$  is a reference time (s),  $T$  is the tidal period (s),  $S$  is the salinity (psu),  $f$  is the freshwater fraction (-),  $S_0$  is the salinity prescribed at the seaward boundaries (psu) and  $K_x$  is the longitudinal eddy diffusion coefficient ( $\text{m}^2 \text{ s}^{-1}$ ).

Fig. 5.28 shows the tidally-averaged  $Q_{salt\_adv}$  at three locations in the grid as a function of the length of channel 1. Shown are the values for the location 4 km upstream of the tidal junction (where only one channel exists) and for the locations in the two channels 4 km downstream of the tidal junction.

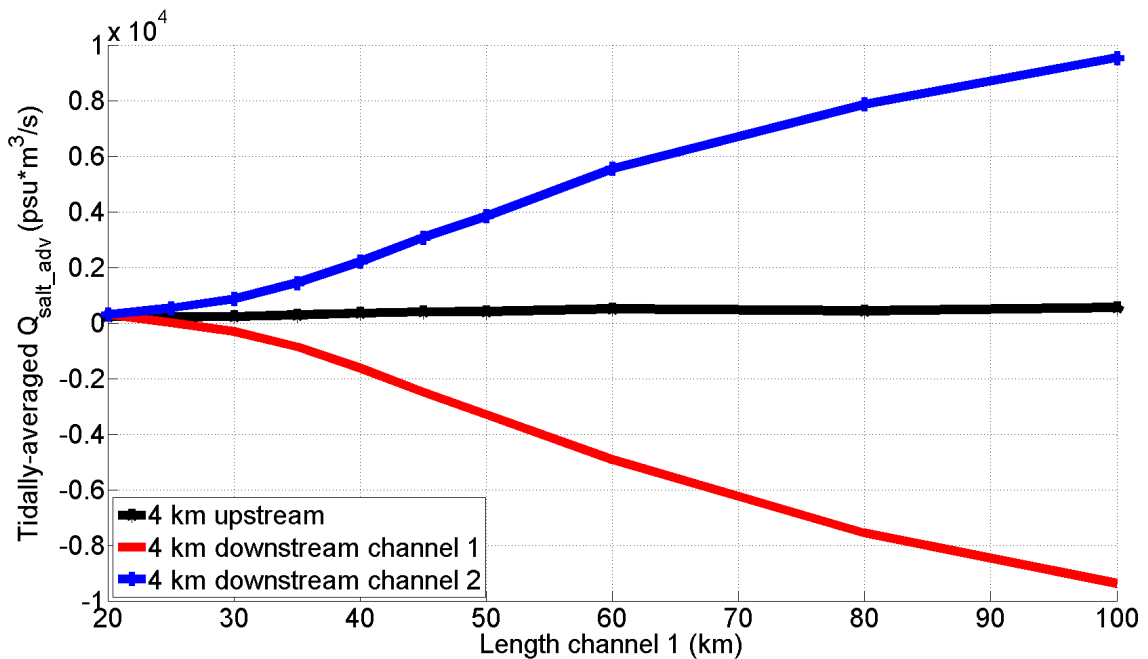


Fig. 5.28: Tidally-averaged, cross-sectional advective salt transport ( $Q_{salt\_adv}$ ) as a function of the length of channel 1. Shown are the transports at three identical locations for different lengths of channel 1. Positive numbers indicate seaward transport.

A detailed inspection of Fig. 5.28 indicates that the tidally-averaged, cross-sectional advective salt transport in channel 1 shows opposite behaviour to that in channel 2. The salt transport in channel 1 turns negative when the length of channel 1 reaches 30 km and becomes increasingly more negative when channel 1 gets longer. On the other hand, the salt transport in channel 2 (of which the channel length is kept constant at 20 km) remains positive and also increases steadily when the length of channel 1 increases. A negative transport in this case is directed upstream, whilst a positive transport is directed downstream. This means that the average advective salt transport in channel 1 is directed from the sea towards the tidal junction as soon as the length of channel 1 is larger than or equal to 25 km. Upstream of the tidal junction, it is also observed that with increasing the channel length, the average advective salt transport increases.

To get a better understanding of the advective salt transport, it is possible to investigate it in some more detail. This is useful, since different contributions make up the total cross-sectional advective salt transport. As explained earlier, the cross-sectional advective salt transport can be defined as (Fischer, 1976; Díez-Minguito et al. 2013)

$$Q_{salt\_adv} = \iint_h^\eta uS \, dy \, dz , \quad (\text{Eq. 5.19})$$

in which  $u$  is the flow velocity,  $S$  the salinity,  $h$  being the mean water column depth,  $\eta$  the sea surface elevation and  $\eta = \eta_{mean} + \eta'$ . To identify the most important salt transport mechanisms in rivers with low river-flow, the tidally averaged and cross-sectional integrated salt transport are often analysed (Fischer, 1976; Dyer, 1997). This can be done by decomposing the tidally averaged, cross-sectional advective salt transport  $\langle Q_{salt\_adv} \rangle$ , which leads to (Lewis & Lewis, 1983; Díez-Minguito et al. 2013)

$$\begin{aligned} \langle Q_{salt\_adv} \rangle = & \int \langle h \rangle \langle \bar{u} \rangle \langle \bar{S} \rangle \, dy + \int \langle \bar{S} \rangle \langle \tilde{\eta} \bar{u} \rangle \, dy + \int \langle \bar{u} \rangle \langle \tilde{\eta} \bar{S} \rangle \, dy + \int \langle h \rangle \langle \bar{u} \bar{S} \rangle \, dy \\ & \text{T1} \qquad \qquad \text{T2} \qquad \qquad \text{T3} \qquad \qquad \text{T4} \\ + \int \langle \tilde{\eta} \bar{u} \bar{S} \rangle \, dy + \int \langle h \rangle \langle \bar{u}_v \bar{S}_v \rangle \, dy + \int \langle h \rangle \langle \bar{u}_v \rangle \langle \bar{S}_v \rangle \, dy + \int \langle \tilde{\eta} \bar{u}_v \bar{S}_v \rangle \, dy . \end{aligned} \quad (\text{Eq. 5.20})$$

Here, for a generic variable  $\xi$ ,  $\langle \xi \rangle$  is the tidal average,  $\bar{\xi}$  is the depth averaged value over the local mean depth,  $\xi_v$  is the deviation with depth from the mean value over the entire depth, or  $\xi = \bar{\xi} + \xi_v$ . The tidal variation is denoted by  $\tilde{\xi}$ , or  $\xi = \langle \xi \rangle + \tilde{\xi}$ . Term T1 in Eq. 5.20 is the transport by mean currents, which is the salt transport as a result of the tidally and depth-averaged water flow (Fischer, 1976; Dyer, 1997). This term is largely a result of river flow but can also contain weather effects, the compensation for the tide-induced landward water transport (Ianniello, 1979) and local differences in the mean flow. Term T2 is the Stokes transport term, which is determined by the phase difference between water level and flow velocity. The tidal pumping terms T3, T4 and T5 are a result of correlating the tidal variations at depth with the depth-averaged salinity and currents. T6 is another tidal pumping term, which is a result of variations in the vertical salinity and current profiles. Term T7 is the contribution of the vertical gravitational circulation and other transport due to vertical shear, whilst T8 results due to correlating the elevation with the tidal variation of  $u$  and  $S$  from the depth-averaged values (Díez-Minguito et al. 2013). In a single channel system, T1 is directed seaward and T2 is directed landward. The sum of T1 and T2 is directed seaward. In a network system, this is not always the case.

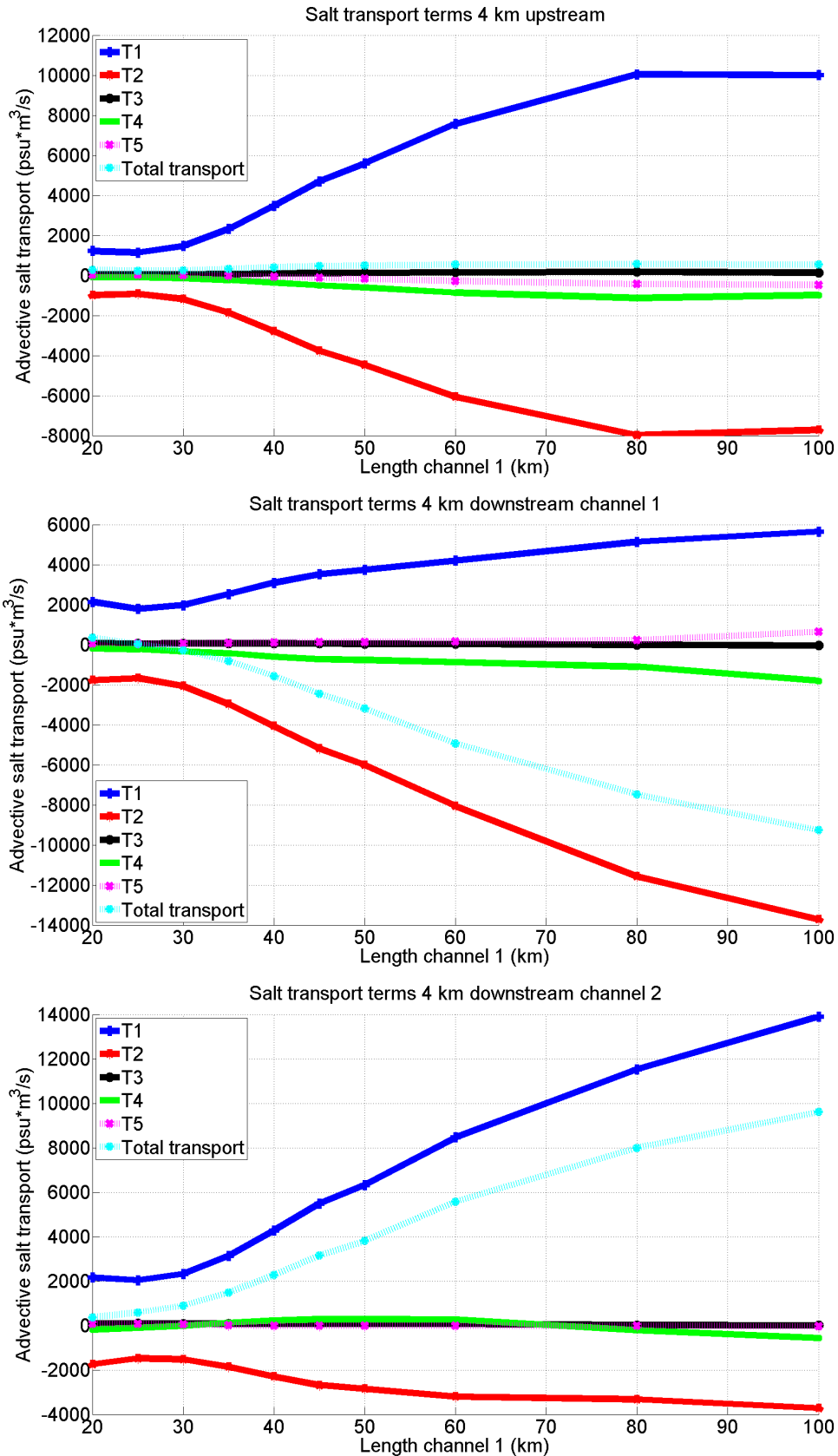


Fig. 5.29: Decomposition of the advective salt transport over the cross-section using the method of Díez-Minguito et al. (2013). Compared to the method of Díez-Minguito et al. (2013), the terms are additionally integrated over the channel width to be able to compare them with the total advective salt transport over the cross-section (as shown in Fig. 5.28). Shown are the terms 4 km upstream of the tidal junction and for both channels 4 km downstream of the tidal junction. The terms T6-T8 are not shown to their negligible magnitude.

Fig. 5.29 shows the cross-sectionally integrated terms T1-T5 of Díez-Minguito et al. (2013) at three different locations. The first subplot shows the transports 4 km upstream of the tidal junction and the other two subplots show the salt transports for both channels 4 km downstream of the tidal junction. Since terms T6-T8 are negligibly small, they are not shown in the figure.

The various salt transport terms upstream of the junction, clearly indicate that the transport by mean currents (T1) is large and always directed from the land to the sea. The Stokes transport (T2) is also large and directed upstream (hence the negative sign). The tidal pumping terms T4-T5 are also directed upstream, but they only become important when the length of channel 1 is increased. The total transport upstream of the junction is still directed seawards, as the downstream transport by mean currents is more important compared to the upstream Stokes transport and tidal pumping terms. The salt transport terms downstream of the tidal junction show different behaviour. For larger channel lengths, the transport by mean currents in channel 1 is much smaller compared to channel 2. At the same time, the Stokes transport in channel 1 is much larger compared to channel 2, which is why the total salt transport in channel 1 is directed upstream. In channel 2, the total salt transport is directed downstream. The tidal pumping terms in both channels are relatively small and mostly directed upstream. They fluctuate between +1000 and -2000  $\text{psu m}^3 \text{s}^{-1}$ .

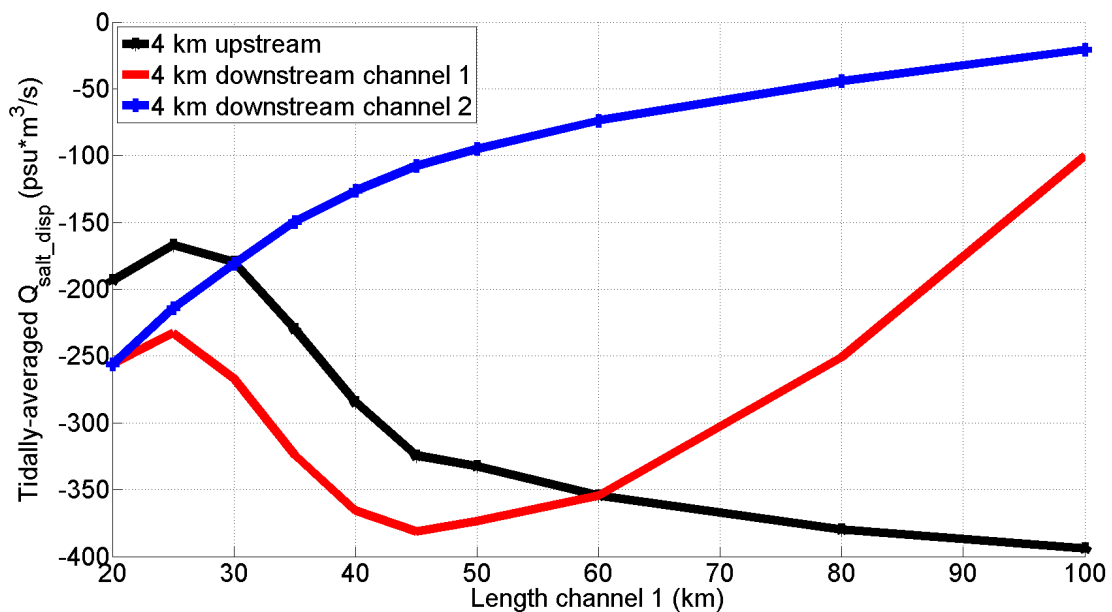


Fig. 5.30: Tidally-averaged, cross-sectional dispersive salt transports ( $Q_{\text{salt\_disp}}$ ) as a function of the length of channel 1. Shown are the discharges at three identical locations in the different model grids.

The tidally-averaged, cross-sectional dispersive salt transport is shown in Fig. 5.30. Note that the dispersive salt transport is always directed upstream (hence the negative values). The dispersive salt transport in channel 1 shows the same pattern as described earlier in the plots regarding advective salt transport. When the length of channel 1 is increased from 20 to 25 km, a slight drop in the dispersive transport is observed, after which it increases when the length of channel 1 is increased to 50 km. When the length of channel 1 is increased even more, the dispersive transport decreases again. The dispersive transport in channel 2 decreases steadily when the length of channel 1 is increased. The dispersive salt transport upstream of the tidal junction shows more or less the same pattern as the salt transport in channel 1 until channel 1 reaches a length 45 km. After that, the upstream dispersive salt transport increases to a larger negative value of nearly -400  $\text{psu m}^3 \text{s}^{-1}$  when channel 1 is 100 km long.

Interestingly, also upstream a slight decrease in dispersive salt transport is observed when the length of channel 1 is increased from 20 to 25 km.

Examining the tidally averaged  $Q_{fresh\_adv}$  (Fig. 5.31), shows that the tidally averaged, cross-sectional advective freshwater transport in channel 1 decreases rapidly with increasing channel length. At some point this transport even becomes negative. In channel 2, the transport increases steadily with a longer channel 1 and reaches  $100 \text{ m}^3/\text{s}$  for a long channel 1. This means that as soon as the two channels have different lengths, the freshwater transport is concentrated in the shorter channel 2. On the other hand, the average advective freshwater transport upstream of the tidal junction decreases slightly when channel 1 is increased to 50 km. After that, it remains more or less constant.

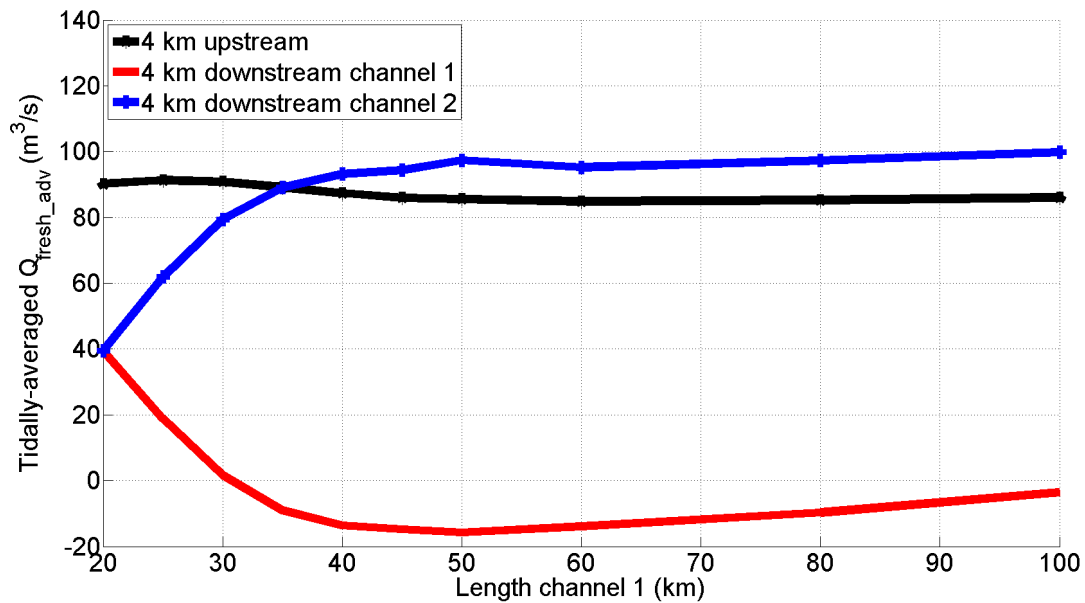


Fig. 5.31: Tidally-averaged, cross-sectional advective freshwater transport ( $Q_{fresh\_adv}$ ) as a function of the length of channel 1. The transport is shown at three identical locations in the different model grids.

The tidally averaged, cross-sectional dispersive freshwater transport  $Q_{fresh\_disp}$  (Fig. 5.32) is much smaller compared to the advective freshwater transport. For increasing channel lengths, the dispersive freshwater transport in channel 2 decreases monotonically to approximately  $0.5 \text{ m}^3 \text{ s}^{-1}$  when channel 1 is 100 km long. The pattern in channel 1 is somewhat different. First a slight drop in the dispersive freshwater transport is observed when the length of channel 1 is increased from 20 to 25 km. Next,  $Q_{fresh\_disp}$  increases again until the length of channel 1 reaches 45 km. After that,  $Q_{fresh\_disp}$  decreases steeply when the length of channel 1 is further increased. The pattern in  $Q_{fresh\_disp}$  as observed upstream of the tidal junction at first resembles the pattern that is observed downstream in channel 1. However, increasing the length of channel 1 to 50 km and beyond does not result in sudden decrease of  $Q_{fresh\_disp}$ . Instead, it increases at a constant rate to reach a maximum value of approximately  $11.5 \text{ m}^3 \text{ s}^{-1}$  when channel 1 is 100 km long.

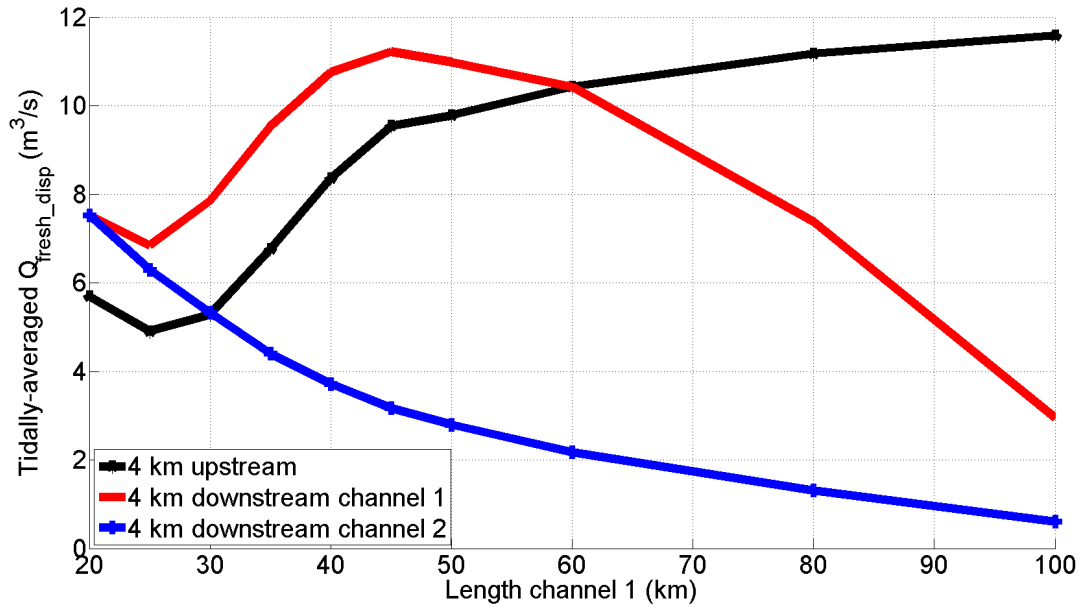


Fig. 5.32: Tidally-averaged, cross-sectional dispersive freshwater transport ( $Q_{fresh\_disp}$ ) as a function of the length of channel 1. The transport is shown at three identical locations in the different model grids.

The cross-sectional cumulative discharge for channels 1 and 2 clearly shows an even division over the two downstream channels (Fig. 5.33). When the channel length is increased, the instantaneous discharge in channel 1 becomes increasingly more negative. At the same time, the instantaneous discharge in channel 2 becomes more and more positive. Adding up the instantaneous discharge in channel 1 and channel 2 yields a positive discharge of 100 m<sup>3</sup>/s, which is equal to the instantaneous discharge that is observed in the upstream cross-section. Moreover, the value of 100 m<sup>3</sup> s<sup>-1</sup> is equal to the river discharge that is added at the upstream boundary.

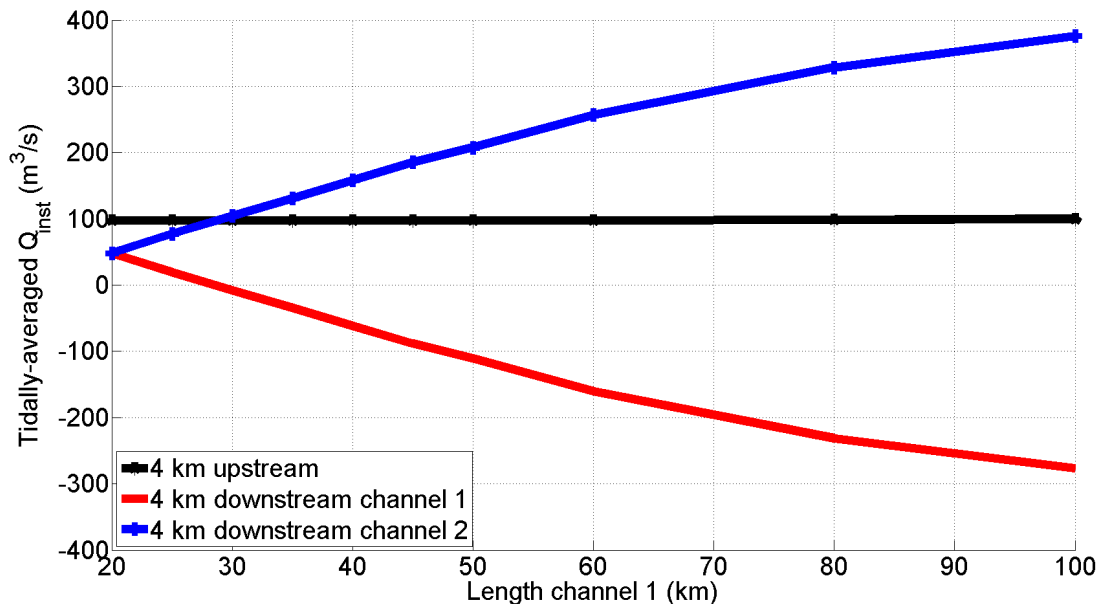


Fig. 5.33: Tidally-averaged, cross-sectional instantaneous discharge ( $Q_{inst}$ ) as a function of the length of channel 1. Shown are the discharges at three identical locations in the different model grids.

The cross-sectional advective freshwater transport can also be decomposed in different transport terms. A method often used is that of Uncles & Lewis (2001). The cross-sectional advective freshwater transport (Eq. 5.14) can also be written as

$$Q_{fresh\_adv} = \int h \overline{u f} dy . \quad (\text{Eq. 5.21})$$

Moreover, the total water flow rate per unit width is defined as

$$q_{tot\_adv} = h \bar{u} . \quad (\text{Eq. 5.22})$$

When the instantaneous transport rate of freshwater per unit width is averaged over a tidal cycle, the following relation is obtained

$$\langle Q_{fresh\_adv} \rangle = \int \underbrace{\langle q_{tot\_adv} \rangle}_{\text{TF1}} \langle \bar{f} \rangle dy + \int \underbrace{\langle \tilde{q}_{tot\_adv} \tilde{f} \rangle}_{\text{TF2}} dy + \int \underbrace{\langle \overline{h u_v f_v} \rangle}_{\text{TF3}} dy . \quad (\text{Eq. 5.23})$$

Here, for a generic variable  $\xi$ ,  $\langle \xi \rangle$  is the tidal average,  $\bar{\xi}$  is the depth averaged value over the local mean depth,  $\xi_v$  is the deviation with depth from the mean value over the entire depth, or  $\xi = \bar{\xi} + \xi_v$ . The tidal variation is denoted by  $\tilde{\xi}$ , or  $\xi = \langle \xi \rangle + \tilde{\xi}$ . Term TF1 is the transport due to the mean currents, TF2 is tidal pumping (Uncles & Jordan, 1979; Simpson et al., 2001) and TF3 is the vertical shear transport per unit width.

Fig. 5.34 shows the cross-sectionally integrated terms TF1-TF3 of Uncles & Lewis (2001) at the three different monitoring locations (4 km upstream of the tidal junction and 4 km downstream of the tidal junction for both channels). The advective freshwater transport terms upstream of the junction indicate that the advective freshwater transport due to mean currents (TF1) is always a large transport term. Also, the total advective freshwater transport is always directed towards the sea. If the length of channel 1 is increased, TF1 decreases constantly. At the same time, the tidal pumping term (TF2) increases until channel 1 is 80 km long, after which it decreases slightly. When channel 1 is 80 km long, TF1 and TF2 are equal. Interestingly, there is not much advective freshwater transport due to vertical shear upstream of the tidal junction (TF3). Only if the length of channel 1 is 100 km, TF3 contributes to some extent. Downstream of the tidal junction, term TF1 shows different behaviour. When the length of channel 1 exceeds 30 km, the total advective freshwater transport becomes negative (thus directed upstream). The same is observed for TF1, which turns negative if the length of channel 1 increases to 30 km. The transport by mean currents and the total advective freshwater transport show more or less the same pattern. The tidal pumping term TF2 is positive and becomes more important with increasing channel length. The advective freshwater transport due to vertical shear (TF3) is positive, starting at 0 and showing a peak around 60 km. Afterwards, it decreases again to 0 when channel 1 is 100 km long. For channel 2, the total advective freshwater transport is always positive. At first, term TF1 increases steadily with increasing channel length until the length of channel 1 is 50 km. After that, TF1 decreases to some extent. However, this is compensated by an increase in TF2. Term TF2 in channel 2 is directed upstream at first, showing a trough around 50 km. Afterwards, the tidal pumping term becomes positive and increases towards 100 km. The advective freshwater transport due to vertical shear (TF3) in channel 2 is negligibly small.



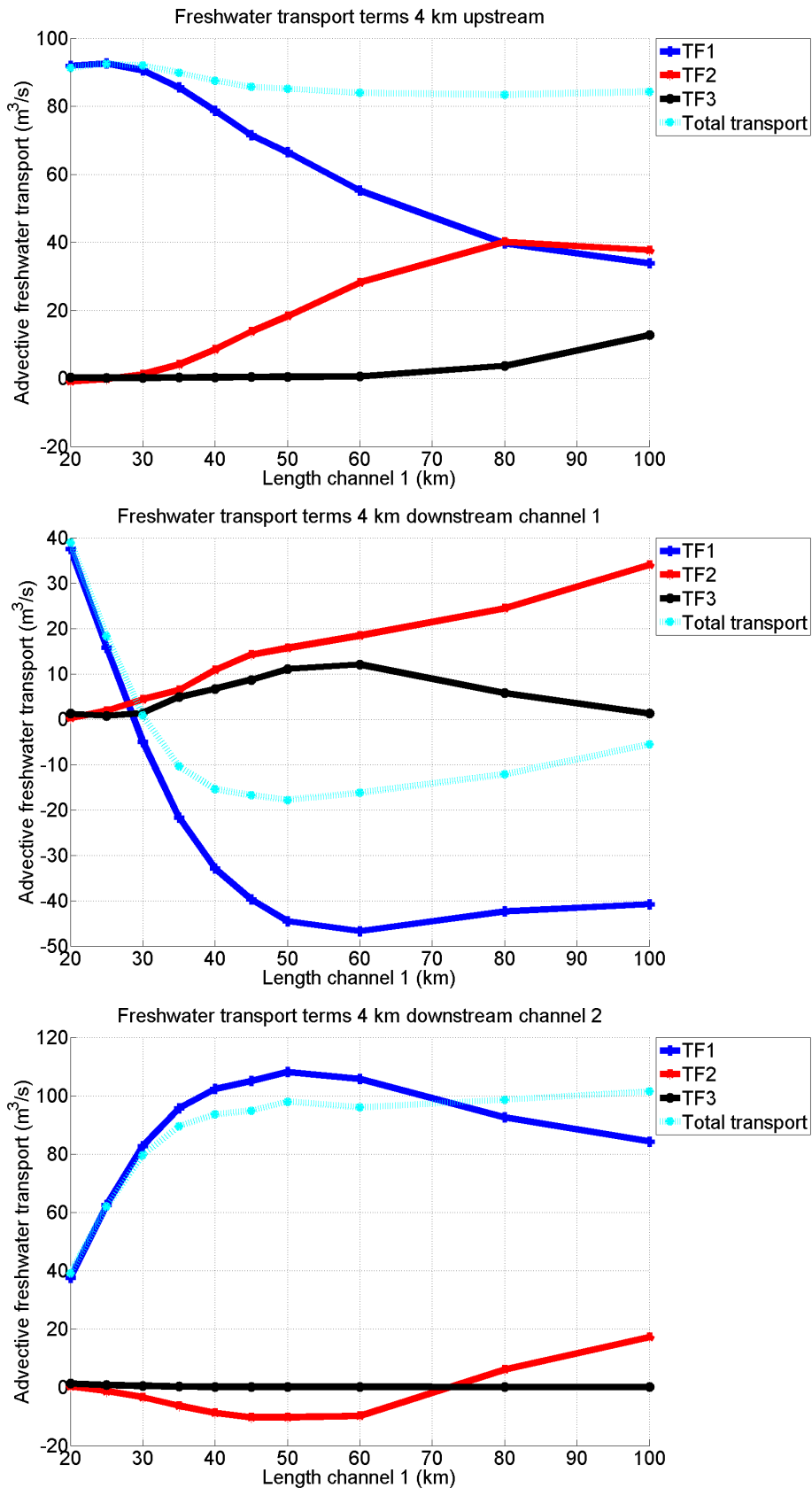


Fig. 5.34: Decomposition of the total advective freshwater transport over the cross-section in the terms of Uncles & Lewis (2001). Compared to the method of Uncles & Lewis (2001), the terms are additionally integrated over the channel width to be able to compare them with the total advective freshwater transport over the cross-section (as shown in Fig. 5.31). Shown are the terms 4 km upstream of the tidal junction and for both channels 4 km downstream of the tidal junction.

## 6. Discussion

In this chapter, the model results will be interpreted and, if possible, linked to previous research by pointing out the similarities and differences between this and earlier studies. The Delft3D model that is used in this study has originally been constructed to study the division of sediment and the morphodynamics at river bifurcations (Kleinhans et al., 2008). A few years later, the model was modified to study the subtidal flow division at an idealised tidal junction (Buschman et al., 2010). The major differences between these two studies is that the study by Kleinhans et al. (2008) used the 3D version of Delft3D and only considers river flow whilst the study by Buschman et al. (2010) used the depth-averaged (2DH) version but also takes into account tidal forcing. The model that is used in this study is a further development of the model by Buschman et al. (2010). The most notable additions to the present model are that the effect of salt is taken into account and that the 3D version of Delft3D is used. Apart from that, an identical sea is added to the end of both channels to have boundaries far away from the region of interest.

Using the modified model, the relative effect of increasing the length difference between the two branches on salt intrusion and tidal propagation was studied. The modelling work leads to counterintuitive results that do not agree well with previous research (such as an increase in intrusion length while increasing the channel length) but existing ideas are also confirmed (such as tides forcing an unequal subtidal flow division at the tidal junction).

### **6.1 Tidal patterns**

The study of Buschman et al. (2010) showed that as soon as one of the downstream channels is longer compared to the other, the tidal motion increases the unequal division of freshwater discharge on the tidal junction. Tidal energy from the short channel will also for a small part enter the longer channel at the tidal junction, thereby causing an increase in tidal amplitude in a short section of the longer channel. This tidal pattern causes freshwater discharge to be forced towards the shorter channel, which is a result of the larger subtidal water level gradient and smaller tidal amplitudes in this channel.

The modelling results from this thesis confirm these findings, albeit the situation is rather different, as tidal flow is now affected by density stratification. It is observed that the water level amplitudes for the cases that the length of channel 1 exceeds 50 km increase just downstream of the tidal junction. This tidal pattern then causes the freshwater discharge to be concentrated in the short channel (Fig. 5.31). At the same time that the water level amplitude in the longer channel is increased due to resonance, the water level amplitude in channel 2 shows a distinct drop between 5 and 10 km downstream of the tidal junction. This can be a result of the competition between friction and the channel convergence. The  $\eta_{M2}$  phase difference (Fig. 5.3) evidently shows that with a longer channel 1 the phase difference downstream of the tidal junction increases. This can be explained by the fact that the tidal wave in channel 1 has to travel a much larger distance to the tidal junction compared to the tidal wave in channel 2.

However, when examining tidal velocities in both channels (Fig. 5.5 and Fig. 5.6), it is clear that the phase speed in channel 2 is much larger compared to channel 1. Thus, the small phase differences in tidal water level at the tidal junction have another cause. When examining the phase difference of the tidal velocities between both channels (Fig. 5.7), the behaviour of the tidal wave near the junction becomes more apparent. The phase differences in tidal velocities

at the tidal junction reach over 4 hours at the tidal junction. As a result, opposite flow directions exist in channel 1 and channel 2 during certain periods. This means that water may enter via channel 1, reach the tidal junction, and flow back to the sea via channel 2. Thus, lateral exchange of water takes place at the junction, which can result in complicated flow patterns, such as vortices and lateral circulations. Moreover, it is also possible that the tidal wave that enters via channel 2 rounds the corner at the tidal junction and enters channel 1 from the opposite side. If tidal energy is transferred from the shorter to the longer channel, this should be the case. This way, it is possible to have two opposite tidal waves in the same channel.

The relative phase difference (Fig. 5.9 and Fig. 5.10) indicates that the tidal wave rounds the corner at the tidal junction. In the real world, it is normal that the flood velocities are ahead of the flood water level. As a result, the relative phase difference (as defined in this thesis), should be negative. However, this is not the case for the 80 and 100 km simulations in channel 1. Here, the flood water level is ahead of the flood velocities. This means that whilst the water level is already dropping for 1 hour, the tidal velocity is still increasing towards its maximum flood velocity. This pattern can only be explained if the tidal wave travels in the opposite direction (thus from the tidal junction towards the sea). At some point, the tidal wave from the seaward and the tidal wave from the landward side will meet in channel 1 and interact with each other. The result is that the water level amplitude is increased. This also gives an explanation for the higher tidal velocities that are observed near the tidal junction in both channel 1 and channel 2 for the case that channel 1 is 80 and 100 km long. Most probably, this is caused by the tide switching from channel 2 to channel 1. As a result, water is extracted from channel 2 and transported to channel 1 and higher flow velocities near the tidal junction will be the result.

The above description shows that the tidal wave in a tidal network shows very interesting behaviour. Particularly near bifurcations and confluences, interesting patterns are observed, such as a tidal wave rounding the corner and propagating back to sea through a different channel. Also opposite flow directions are observed during some simulations. Nevertheless, a much more detailed analysis of the tidal characteristics in the channel network can be done by using an analytical model instead of a numerical model. A model that seems to be well-suited for this is the analytical model used by Hill & Souza (2006). The downside of this model is that it assumes linear friction. Nevertheless, it would be interesting to compute the tidal characteristics in the network using this model and see what type of tidal wave comes out of this calculation.

## **6.2 Salinity distribution and salt balance**

The present research shows that in order to develop well-mixed conditions in the model grid, a low river discharge and a high tidal range is needed. This is in agreement with the theory of Pritchard (1955) and Cameron & Pritchard (1963), as described in Valle-Levinson (2010). A reduction in river flow also causes the water column to become more mixed and the salt to intrude further upstream. This is in agreement with all theories on salt intrusion (such as MacCready, 2004 and Savenije, 2005) and also been observed multiple times in the field (Prandle, 2004).

The along-channel tidally- and width-averaged contour plots indicate that with increasing channel length, the salinity increases and intrudes further upstream. Apart from that, the tidally and width-averaged salinity in channel 1 increases drastically when the length of channel 1 is increased. When the length of channel 1 exceeds 40 km, the tidally and width-

averaged salinity in the downstream part of channel 1 is equal to the salinity prescribed at the seaward boundary (34 psu). The length of this section with sea-salinity increases for a longer channel 1. The pattern in channel 2 is completely different. Most notably, the salinity values in channel 2 are lower compared to channel 1. These patterns indicate that with a longer channel 1, salt intrudes easier through channel 1. The most probable cause for this is that tidal pattern forces the freshwater discharge to concentrate itself in the shorter channel 2. This means that at some point the intruding salt in the longer channel 1 is hardly counteracted by the freshwater discharge and channel 1 will get a much higher salinity value.

The salt intrusion upstream of the tidal junction shows a remarkable dependence on channel length. A small drop in intrusion length of approximately 9 km is observed when the length of channel 1 is changed from 20 to 25 km. After that, the intrusion length increases constantly with channel 1 being increased step by step to 100 km. It reaches a maximum value of over 23 km upstream of the tidal junction. It seems counterintuitive that with an increasing channel length, salt intrudes further upstream. After all, the salt has to travel a larger distance so it seems more obvious that an increasing channel length leads to a decrease in intrusion length. The main explanation for this is the fact that freshwater discharge is concentrated in the shorter channel. Examining the different cross-sectional transports explains this even more.

The tidally-averaged  $Q_{salt\_adv}$  (Fig. 5.28), clearly shows that increasing the length of channel 1 results in negative cross-sectional advective salt transport in channel 1 (thus directed upstream). At the same time, the cross-sectional advective salt transport in channel 2 becomes increasingly more positive (directed downstream). In other words, a lot of salt is transported through channel 1 upstream to the tidal junction. Upstream of the tidal junction, the average salt transport also increases slightly when the length of channel 1 increases. This can be explained by examining Fig. 5.18, which shows that the salt intrudes further upstream with an increasing length of channel 1. This in turn will lead to larger salt transports upstream of the tidal junction. Why the slight drop in salt intrusion length at 25 km occurs is not entirely clear. It could be a result of the cross-sectional advective salt transport in channel 1 being nearly zero. As soon as the length of channel 1 is over 25 km, the salt intrusion length increases again. At the same time, the cross-sectional advective salt transport turns negative and increases substantially in size (thereby transporting salt to the junction). In steady-state conditions, the dispersive and advective terms need to balance (Dyer, 1997). Studying the tidally averaged values of  $Q_{salt\_adv}$  (Fig. 5.28) and  $Q_{salt\_disp}$  (Fig. 5.30), suggests that they balance. In that case, the simulations have reached the steady state.

To see whether the simulations have reached equilibrium, the salt balance in the estuary is analysed for the case that both downstream channels have equal lengths (20 km). To be sure that the simulation reached some kind of equilibrium, the simulation time was 1.5 years. It is easy to test whether the simulations are in equilibrium, since in that case the tidally averaged cross-sectional dispersive and advective salt transport should balance (sum should be zero). For a cross-section upstream of the tidal junction, this means that the following balance should apply

$$\langle Q_{salt\_adv} \rangle + \langle Q_{salt\_disp} \rangle = 0 . \quad (\text{Eq. 6.1})$$

For the cross-sections at the two downstream channel mouths, the balance would be

$$\langle Q_{salt\_adv} \rangle_{ch1} + \langle Q_{salt\_disp} \rangle_{ch1} + \langle Q_{salt\_adv} \rangle_{ch2} + \langle Q_{salt\_disp} \rangle_{ch2} = 0 . \quad (\text{Eq. 6.2})$$

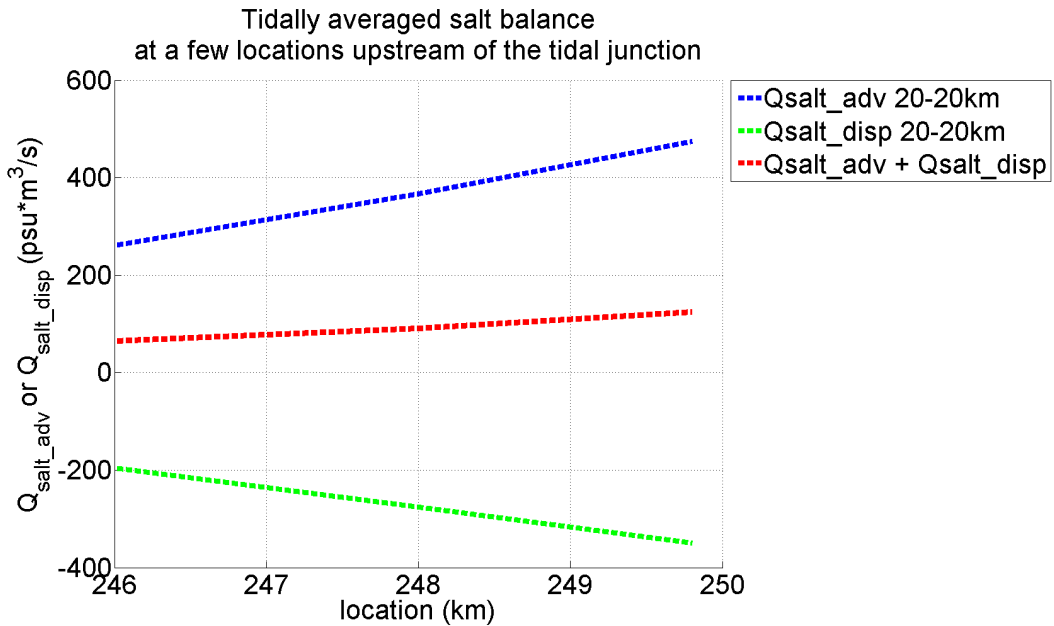


Fig. 6.1: Tidally averaged, cross-sectional advective and dispersive salt transport and the sum of both transports plotted at a few locations just upstream of the tidal junction. In this simulation, channel 1 and 2 are both 20 km long.

For now, the salt balance just upstream of the tidal junction will be investigated in more detail. The tidally averaged salt balance for a few cross-sections just upstream of the tidal junction (Fig. 6.1) indicates that the simulation is not in equilibrium. The cross-sectional advective salt transport is positive (downstream) and the cross-sectional dispersive salt transport is negative (upstream). However, the sum of both terms is not zero and also not constant in space. Interestingly, the sum of both terms gives a positive number, meaning that on average salt is transported downstream. This is a puzzling result, as an estuary that has not reached steady state yet, would be expected to import salt. If that is the case, this term has to be directed upstream (and thus negative).

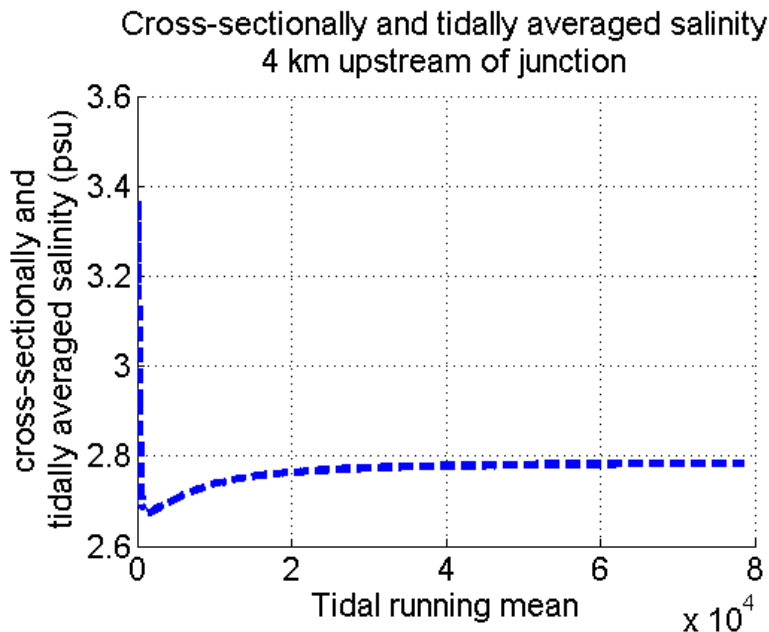


Fig. 6.2: The cross-sectionally and tidally-averaged salinity versus the tidal running mean (moving average). The results are displayed for the cross-section located 4 km upstream of the tidal junction. In this simulation, channel 1 and 2 are both 20 km long.

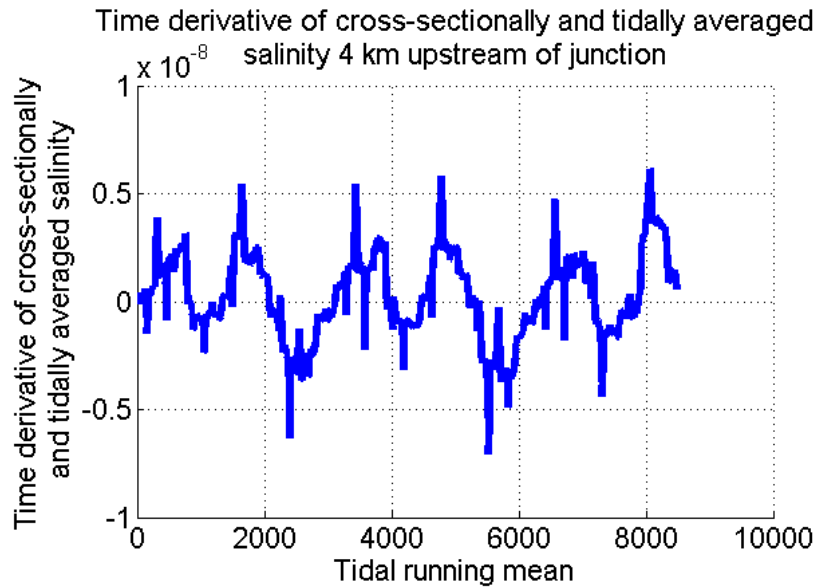


Fig. 6.3: Time-derivative of the cross-sectionally and tidally-averaged salinity plotted versus the tidal running mean (moving average). The cross-section is located 4 km upstream of the tidal junction. In this simulation, channel 1 and 2 are both 20 km long.

Another check to see whether the simulation is in equilibrium is to compute the tidally and cross-sectionally averaged salinity through time by using a tidal running mean (moving average). Fig. 6.2 shows the cross-sectionally and tidally averaged salinity  $\langle \bar{S} \rangle$  for the cross-section located 4 km upstream of the tidal junction. At first, the cross-sectionally and tidally averaged salinity changes quite rapidly but soon it seems to approach a value just below 2.8 psu. This suggests that the simulation has more or less reached equilibrium, since there is hardly any change in cross-sectionally and tidally averaged salinity over time. This is even more exemplified in Fig. 6.3, which shows the time derivative of the cross-sectionally and tidally averaged salinity ( $d\langle \bar{S} \rangle / dt$ ). As displayed in this figure,  $d\langle \bar{S} \rangle / dt$  is very small, strengthening the suspicion that the simulation has reached equilibrium.

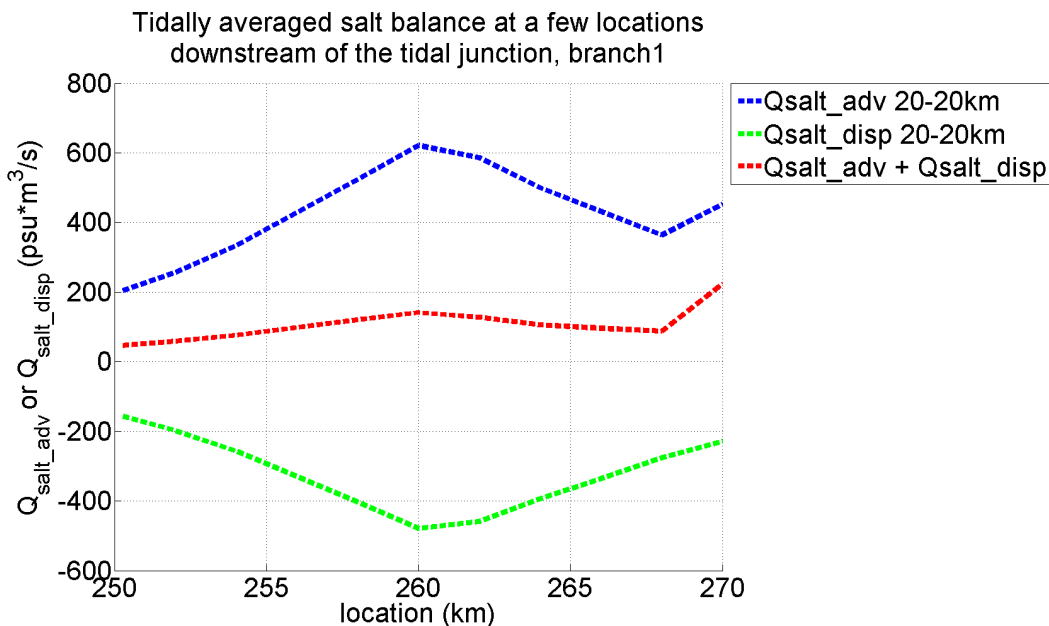


Fig. 6.4: Tidally averaged, cross-sectional advective and dispersive salt transport and the sum of both transports plotted downstream of the tidal junction. The patterns in the two downstream channels are identical, as both channels are 20 km long.

The salt balance for the channels downstream of the tidal junction is given in Fig. 6.4. Clearly, the salt balance in the downstream channels is also not valid here. More or less the same pattern is observed as in the upstream part. When adding up the tidally-averaged cross-sectional advective and dispersive salt transport, both channels show positive numbers that change through space. Therefore, these results indicate that the salt balance is not valid in the entire grid (no steady state conditions have been reached). However, a detailed analysis of the salinity values upstream of the junction indicates that steady state conditions do exist and the salt balance should therefore be valid.

Analysing the cross-sectional advective freshwater transport  $Q_{fresh\_adv}$  (Fig. 5.31) confirms the findings of Buschman et al. (2010), who stated that the freshwater discharge is concentrated in the shortest channel. This means that at some point the intruding salt in the longer channel 1 is hardly counteracted by the freshwater discharge. As a result, salt can easily intrude up to the tidal junction through this longer channel. The larger the length differences between the two channels, the larger this effect becomes. As a result, the salt intrudes further upstream when channel 1 gets longer. The average salt transport upstream of the junction increases because the salt intrudes further upstream when channel 1 is longer, thereby increasing the salt transport in that part of the estuary. When decomposing the freshwater transport according to Uncles & Lewis (2001), it turns out that the cross-sectional advective transport is most important component. The tidal pumping terms are particularly important upstream and in channel 1, whilst in channel 2 the transport by mean currents is dominant. The vertical shear transport is negligibly small, most probably because the water column is well-mixed.

The salt balance can also be rewritten as a freshwater balance. For this, the river discharge that is prescribed at the upstream boundary also needs to be taken into account ( $Q_{river} = 100 \text{ m}^3/\text{s}$ ). Therefore, the tidally averaged freshwater balance for a cross-section upstream of the tidal junction reads

$$\langle Q_{fresh\_adv} \rangle + \langle Q_{fresh\_disp} \rangle = Q_{river} . \quad (\text{Eq. 6.3})$$

For the cross-sections at the two downstream channel mouths, the freshwater balance reads

$$\langle Q_{fresh\_adv} \rangle_{ch1} + \langle Q_{fresh\_disp} \rangle_{ch1} + \langle Q_{fresh\_adv} \rangle_{ch2} + \langle Q_{fresh\_disp} \rangle_{ch2} = Q_{river} . \quad (\text{Eq. 6.4})$$

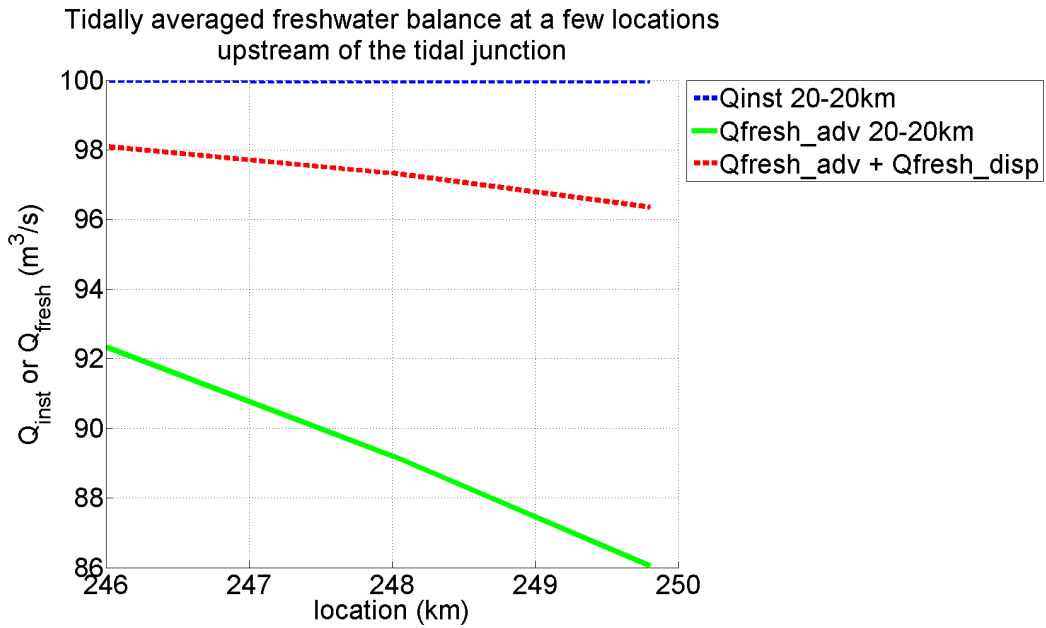


Fig. 6.5: Tidally averaged, cross-sectional advective and dispersive freshwater transport and the sum of both transports plotted upstream of the tidal junction. Channel 1 and 2 are both 20 km long.

The tidally averaged freshwater balance just upstream of the tidal junction (Fig. 6.5) and in both channels downstream of the tidal junction (Fig. 6.6) indicates that also this balance is not valid. Whilst the tidally-averaged instantaneous discharge  $Q_{inst}$  equals  $100 \text{ m}^3 \text{ s}^{-1}$  in the upstream part and  $50 \text{ m}^3 \text{ s}^{-1}$  in both downstream channels, this is not the case for the freshwater balance. Analogously to the salt balance, the freshwater balance does not have a constant value but varies through space.

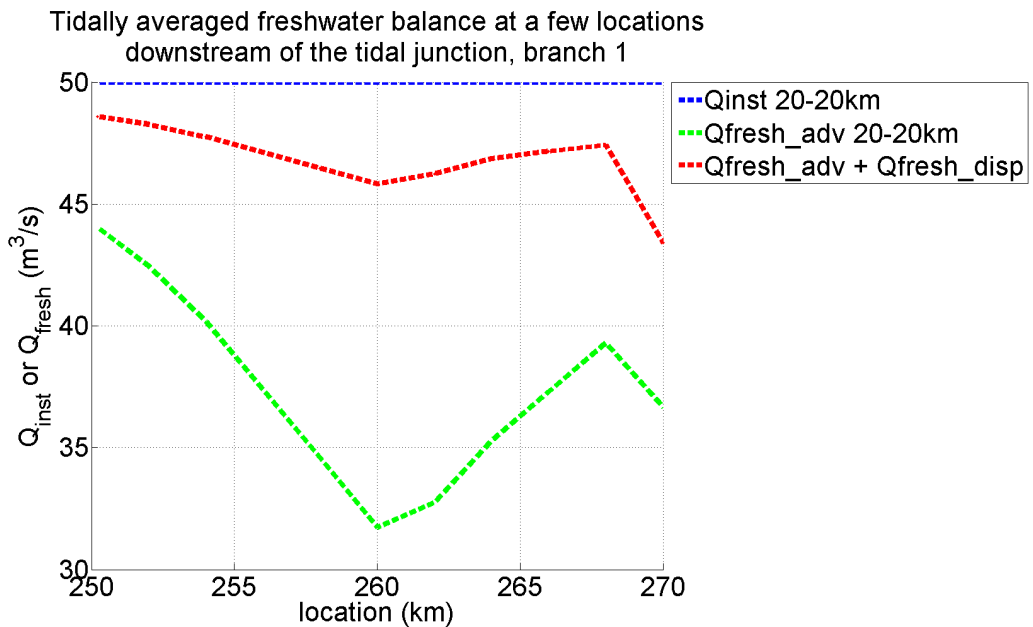


Fig. 6.6: Tidally averaged, cross-sectional advective and dispersive freshwater transport and the sum of both transports plotted downstream of the tidal junction. The patterns in the two downstream channels are identical, as both channels are 20 km long.



### **6.3 Quantifying salt intrusion length**

As described in sections 3.6 and 3.7, different theories exist that can be used to quantify the maximum distance salt intrudes in an estuary. The downside is that these theories are often only applicable to the estuary on which the theory has been calibrated and that their performance is therefore limited. In this section, we will compare the intrusion length as computed by different theories with the observed intrusion length in the Delft3D simulations. The focus will be on the performance of the theory of Savenije (1993; 2005), MacCready (2004), Brockway et al. (2005), Nguyen & Savenije (2006) and Gisen et al. (2015).

The drawback with most theories regarding salt intrusion is that they are based on single-channel estuaries. However, Nguyen & Savenije (2008) investigated whether the theory of Savenije (1993; 2005) could also be applied to multi-channel estuaries, such as the Mekong. They discovered that combining two paired branches as a single estuary branch lead to better results than considering every single branch as an individual estuary.

As described in section 5.3, the freshwater transport in channel 1 quickly turns negative for larger lengths of channel 1. As a result, the theories of Savenije (1993; 2005), Brockway et al. (2005), Nguyen & Savenije (2006) and Gisen et al. (2015) will not give reliable results since they need the freshwater discharge as input for parameters (such as the estuarine Richardson number). Therefore, it was decided to use the method of Nguyen & Savenije (2006), in which two branches are paired as a single estuary branch. Pairing two estuary branches is done by adding up the area and channel width of both branches. Moreover, the paired flow velocity, tidal velocity amplitude, tidal range, vertical eddy viscosity, vertical eddy diffusivity and tidal excursion are computed as the weighted mean between the cross-sectional areas of the two channel mouths. Apart from that, the intrusion length needs to be computed with respect to a certain point in the estuary. In normal cases, this is the estuary mouth but this is not convenient in an estuary where the length difference between the two channels can be 80 km. Therefore, the upstream salt intrusion length in the Delft3D simulations was computed with respect to the tidal junction (see Fig. 5.18).

When using the different theories to compute the salt intrusion length in the paired estuary branches, the combined (weighted mean) intrusion length is obtained. To be able to compare the computed salt intrusion lengths with the salt intrusion lengths as observed in Delft3D, the intrusion lengths upstream of the tidal junction as computed in Delft3D need to be converted to combined (weighted mean) intrusion lengths. For this, the paired downstream channel length is needed, which is computed as the weighted mean between the cross-sectional areas of the two channel mouths. The Delft3D combined intrusion length is then defined by adding the paired downstream channel length to the intrusion length upstream of the junction.

Fig. 6.7 shows the combined (weighted mean) intrusion length (observed from Delft3D modelling results and the different theories) plotted versus the length of channel 1. A direct comparison between the different theories and the Delft3D observations is given in Fig. 6.8. Examining both plots, it becomes apparent that none of the theories gives a good indication of the combined salt intrusion length that is observed in Delft3D. Most theories show the opposite pattern of that seen in the Delft3D observations (a decrease instead of an increase in intrusion length for a longer channel 1). The method of MacCready (2004) results in very low combined intrusion lengths of at most 2 km, which are way lower than observed in Delft3D. The 3 equations of Gisen et al. (2015) result in a combined intrusion length of approximately 20 km for all simulations which slightly decreases when the length of channel 1 is increased. Also the method of Savenije (1993; 2005) gives the largest combined intrusion lengths

(approximately 30 km) for the shortest length of channel 1. In that case, the computed combined intrusion length nearly equals the intrusion length as observed in Delft3D. When the length of channel 1 is increased, the combined intrusion length slowly decreases to approximately 20 km. The theories that come closest to the observed pattern in Delft3D are the method of Brockway et al. (2005) and Nguyen & Savenije (2006). The method of Brockway et al. (2005) underestimates the intrusion length for all simulations, but shows larger combined intrusion lengths for a longer channel 1. Also the method of Nguyen & Savenije (2006) shows larger combined intrusion lengths for a longer channel 1. Contrary to the method of Brockway et al. (2005), the method of Nguyen & Savenije (2006) mostly overestimates the intrusion length. Only for the case that channel 1 is 80 km long, the combined intrusion length as observed in Delft3D is nearly equal to the intrusion length as computed using the method of Nguyen & Savenije (2006).

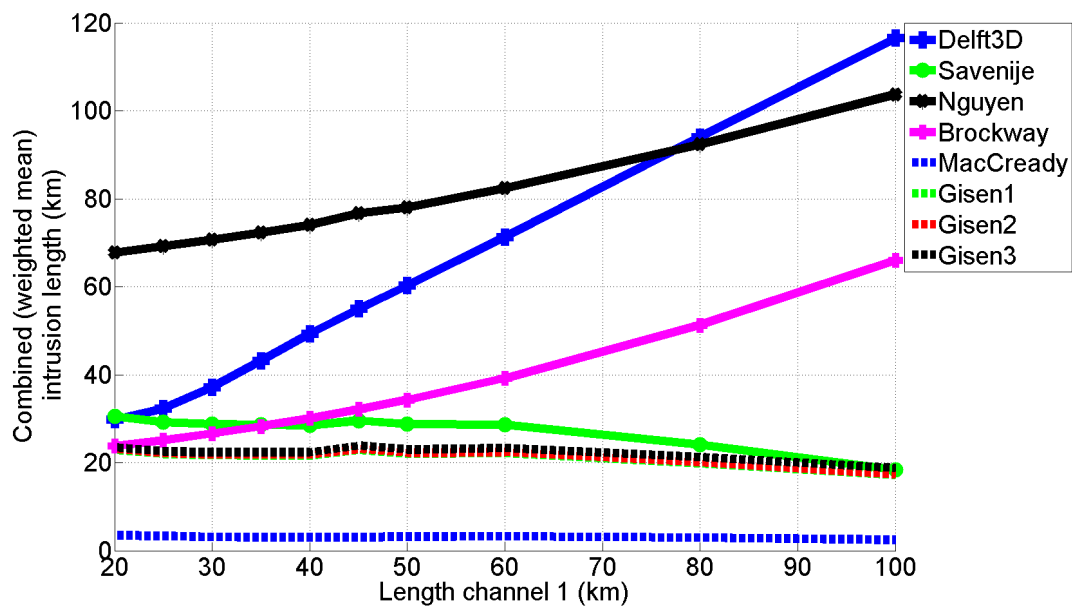


Fig. 6.7: Combined (weighted mean) intrusion length (computed using Delft3D modelling results and the theories) plotted versus the length of channel 1.

The above results show that the existing theories for computing salt intrusion length are not directly applicable to multi-channel estuaries with different channel lengths. From the five tested theories, only the theory of Brockway et al. (2006) and Nguyen & Savenije (2006) produce reasonable results. Still, the length difference between the Delft3D observations and these theories is quite large but both theories at least show the same pattern as the Delft3D observations. The theory of Savenije (1993; 2005) only gives a reasonable result for the case that channel 1 is 20 km long. A probable cause for this is that all these theories are based on one-dimensional approximations, particularly with regards to the horizontal diffusion parameter. The choice for this parameter is always a large point of discussion. The one-dimensional approximation may have more even influence in estuarine channel networks compared to single-channel estuaries. Particularly the 3D flow patterns that occur at the junction can probably not be described in detail using a one-dimensional approximation. Another point is that it is difficult to apply theories for single-channel theories on multi-channel estuaries. Up to now, this has only been done for multi-channel estuaries where the different branches have more or less equal lengths. Thus far, no standalone theory exists for computing salt intrusion in multi-channel estuaries with different channel lengths.

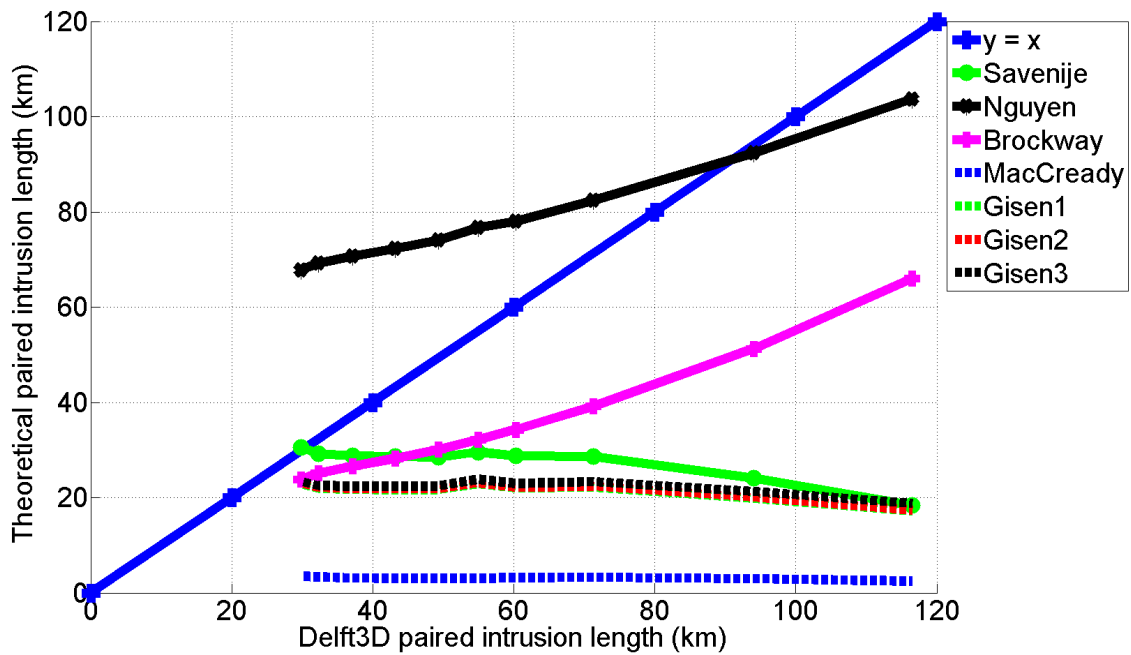


Fig. 6.8: Theoretical paired intrusion length (computed using the different theories) plotted versus the computed paired intrusion length (computed using the Delft3D modelling results).

#### **6.4 Model recommendations**

The present model gives reasonable results, but the assumptions and choices made during the model set-up can greatly influence model outcomes. In this model study, a total of 10 vertical layers have been used. However, many modelling studies (e.g. Simpson et al., 2001; Burchard & Hetland, 2010) use at least 50-100 vertical layers to increase the vertical resolution. The downside of increasing the vertical resolution is that the computation time is also increased drastically. For example, when increasing the number of vertical layers from 10 to 50, the simulation time also increases by a factor 5. Because of the drastic increase in computation time and the fact that other Delft3D model studies (such as Van Breemen, 2008) also use 10 vertical layers, it was decided to use the same amount of vertical layers in this study. Another choice was to keep all boundary conditions identical, even though the mouths of both channels are situated at a considerable distance from each other. Particularly with larger differences in channel lengths, this effect becomes significant. Apart from that, estuaries with large differences in length between the different channels are hardly seen in the real world (Nguyen & Savenije, 2006). If this would be the case, the tidal wave would have a different phase at the mouth of long channel. Moreover, the two seas at the end of the downstream channels are not connected. This will also affect the results (particularly with regards to tidal propagation in the two channels).

Another drawback of the model is that due to numerical issues, two gridcells need to disappear at the tidal junction. Even though the resulting decrease in cross-sectional area is relatively small (only 1/8th of the cross-sectional area is lost; Buschman et al., 2010), this is not consistent with reality. It would be better to develop a model in which no gridcells need to disappear at the junction. It was also observed that the tidal wave does not damp out completely in the river, meaning that the river should be made longer to let the tidal wave dampen out completely. Therefore, it is advised to increase the length of the river upstream of the tidal junction. Moreover, as already extensively discussed in chapter 3, the salinity profiles in Delft3D show wiggles with certain boundary conditions. This is especially the case in stratified conditions and while using the so called  $k-\varepsilon$  turbulence model. Even though this is the most sophisticated turbulence closure model that is available in Delft3D, simulations with

this turbulence model continuously show wiggles in the salinity profiles. Therefore, the simulations in this study were conducted using the  $k-l$  turbulence model. However, wiggles also appeared in the simulations as soon as the stratification was increased. Therefore, it is strongly advised to study salt intrusion with the present version of Delft3D in partially to well-mixed conditions only. In the future, it would be interesting to see whether newer versions of Delft3D still show wiggleless in the salinity profiles, especially in stratified conditions or when using the  $k-\varepsilon$  turbulence model. Apart from that, the salt balance in Delft3D needs more research. First of all, it is necessary to investigate whether Delft3D can reach a steady state with regards to salinity intrusion in an estuary. The method on how Delft3D calculates the cross-sectional dispersive and advective salt transport also needs to be studied in more detail. This is particularly important because the tidally-averaged cross-sectional transport terms indicate that steady state conditions have not been reached whilst at the same time the tidally- and cross-sectionally averaged salinity values indicate the opposite. Finally, to analyse the tidal characteristics in an estuarine channel network in more detail, it is advised to use an analytical model analogous to the model used by Hill & Souza (2006).

### **6.5 Suggestions for further research**

Since this research is still in its early stage, many aspects of salt intrusion in estuarine channel networks are still unknown. The present study focused on modelling salt intrusion in estuarine channel networks, while only adjusting the length differences between the two branches. However, there are many more variables that can be varied in the present model. A few suggestions are provided in the earlier mentioned papers of Kleinhans et al. (2008) and Buschman et al. (2010). The present model assumes a constant depth throughout the entire grid, but natural estuarine channels are characterised by both longitudinal and lateral variations in depth. Adding a variable bathymetry to the existing model will definitely provide additional insights in the dynamics of salt intrusion in estuarine channel networks. Particularly modifying the bathymetry in one channel and keeping it constant in the other channel (as in Buschman et al., 2010), would be an interesting option. Another option to investigate with the present model is to vary the  $e$ -folding length scale (increasing or decreasing the exponential width increase), or even to have no width increase at all. Also modifying the Chézy coefficient could be interesting to study the effect of modifying the bed roughness. Other modifications that are suggested to be implemented in future studies read as follows:

- Increase the vertical resolution of the model
- Alter the angle of bifurcation
- Situate the bifurcation in a bend
- Introduce differences in width between the downstream branches
- Vary the river discharge
- Impose different tidal components and phases at the mouth of both channels
- Different boundary conditions for each downstream channel
- Add sedimentation processes and sediment transport

So far, the present model demonstrated remarkable results while modelling salt intrusion in estuaries. Some issues remain, such as a relatively low vertical resolution, wiggles in the salinity profiles under certain circumstances and conflicting results with regards to the salt balance. These problems will hopefully be addressed in the future by modifying the present model and using newer versions of Delft3D. Concluding from the list above, it is clear that many aspects are still unknown and need more research. Thus, there are plenty of opportunities, to expand this investigation and to get to know even more about the fascinating dynamics of salinity intrusion in estuarine systems.

## 7. Conclusions

The main goal of this research was to investigate salt intrusion, tidal propagation and the related processes in a partially- to well-mixed estuarine channel network with various channel lengths. After carefully designing domain, turbulence parameterisation and boundary conditions, the Delft3D model proved to be well-suited to model salt intrusion in an estuarine channel network. The default model run consisted of a river with a length of 250 km which splits in two equal channels of 20 km long. The length of channel 1 was increased step-by-step to 100 km (intermediate steps being 25, 30, 35, 40, 45, 50, 60 and 80 km). All model runs were performed with the same ideal boundary conditions, being a constant river discharge of  $100 \text{ m}^3 \text{ s}^{-1}$  and a seaward boundary with a  $M_2$  tidal amplitude of 1.4 m. The salinity at the seaward boundary was set to 34 psu.

The harmonic analysis of the tidal characteristics showed large differences between the tidal water levels and tidal velocities. The water level amplitudes show a distinct amplification in channel 1 for an increased length of channel 1. The cause for this is the transfer of tidal energy from channel 2 to channel 1 at the tidal junction. This leads to a larger subtidal water level gradient and smaller water level amplitudes in channel 2, causing the freshwater discharge to be concentrated in the shorter channel. The transfer of tidal energy causes the tidal wave from channel 2 to round the corner at the tidal junction and to propagate from the tidal junction towards the sea. This is supported by the positive relative phase difference in a part of channel 1. At some point, the tidal wave from the seaward and the tidal wave from the landward side will meet in channel 1 and interact with each other and the water level amplitude will be amplified. Another indication for the tidal wave rounding the corner is that the tidal velocity phase difference between both channels at the junction increases linearly for increasing channel lengths. For the situation that channel 1 is 100 km long, the phase difference between the two channels is over 4 hours at the tidal junction. As a result, opposite flow directions exist in channel 1 and channel 2, meaning that water can enter via one channel, reach the tidal junction, and flow back to the sea via the other channel.

The salinity results indicate that with an increasing length of channel 1, salt intrudes further upstream. When channel 1 is 100 km long, the intrusion length is nearly 14 km longer compared to the symmetric simulation. The cause for this behaviour is that with a longer channel 1, the freshwater discharge is concentrated in the shorter channel 2. As a result, a lot of salt is transported upstream through the longer channel, causing an increase in salinity intrusion. Vertical stratification for all simulations is limited to values less than 10%, as a result of which all simulations fall within the category of the well-mixed estuaries. A detailed analysis of the cross-sectional advective salt transport revealed that transport by mean currents and Stokes transport are the most important advective salt transport mechanism in the simulations. For the advective freshwater transport, the most important terms are transport due to mean currents and tidal pumping.

This model study has led to remarkable results considering the tidal propagation and salt intrusion in multi-channel estuaries. Some issues remain, particularly the disagreement in the Delft3D model results on whether the simulation reached steady state or not. Nevertheless, the outcomes of this model study can provide useful information about the future development of multi-channel estuaries in the real world. Especially with the anticipated climate change, this study can provide a basic framework for further studies on salt intrusion and tidal propagation in multi-channel estuaries.

## 8. References

- Bakhmetev, B. A. (1932): Hydraulics of open channels, *Engineering Societies Monographs* McGraw-Hill, pp. 329.
- Brockway, R., Bowers, D., Hogue, A., Dove, V. & Vassele, V. (2006): A note on salt intrusion in funnel-shaped estuaries: application to the Incomati estuary, Mozambique. *Estuarine, Coastal and Shelf Science*, 66, pp. 1–5.
- Burchard, H. & Baumert, H. (1995): On the performance of a mixed-layer model based on the  $k-\epsilon$  turbulence closure. *Journal of Geophysical Research*, 100, pp. 8523–8540.
- Burchard, H., & Hetland, R. D. (2010): Quantifying the contributions of tidal straining and gravitational circulation to residual circulation in periodically stratified tidal estuaries. *Journal of Physical Oceanography*, 40(6), pp. 1243–1262.
- Buschman, F. A., Hoitink, A. J. F., Van Der Vegt, M. & Hoekstra, P. (2010): Subtidal flow division at a shallow tidal junction. *Water Resources Research*, 46(12), pp. 1–12.
- Buschman, F. A. (2011): Flow and sediment transport in an Indonesian tidal network. *Utrecht Studies in Earth Sciences*, 7, PhD thesis, pp. 140.
- Cameron, W. M. & Pritchard, D. W. (1963): Estuaries. In: *The Sea* (Ed. MN Hill), Vol. 2, Wiley, New York, pp. 306–324.
- Chant, R. J. (2010): Estuarine secondary circulation. In: Valle-Levinson, A. (2010): *Contemporary issues in estuarine physics*, Cambridge University Press, pp. 100–124.
- Davies, J. H. (1964): A morphogenetic approach to world shorelines. *Zeitschrift für Geomorphologie*, 8, pp. 127–142.
- Deltares (2014): Delft3D-FLOW User Manual: *3D/2D modelling suite for integral water solutions*, pp. 710, Deltares, Delft, The Netherlands.
- De Goede, E. D., 2009. Stratificatieproblemen in TRIWAQ en aanbevelingen voor het Volkerak-project. *Deltares memo*, 26 oktober 2009, pp. 11.
- Díez-Minguito, M., Contreras, E., Polo, M. J. & Losada, M. A. (2013): Spatio-temporal distribution, along-channel transport, and post-riverflood recovery of salinity in the Guadalquivir estuary (SW Spain). *Journal of Geophysical Research: Oceans*, 118(5), pp. 2267–2278.
- Dyer, K. R. (1997). Estuaries: a physical introduction, 2<sup>nd</sup> edition. *John Wiley & Sons*, pp. 195.
- Fischer, H. B. (1972): Mass transport mechanisms in partially stratified estuaries. *Journal of Fluid Mechanics* 53, pp. 672–687.
- Fischer, H. B. (1974): Discussion of 'Minimum length of salt intrusion in estuaries' by B.P. Rigter, 1973. *Journal of the Hydraulics Division*, 100(5), pp. 708–712.
- Fischer, H. B. (1976): Mixing and dispersion in estuaries. *Annual Review of Fluid Mechanics*, 8, pp. 107–133.
- Fischer, H. B., List, E. J., Koh, R. C. Y., Imberger, J. & Brooks, N. H. (1979): Mixing in inland and coastal waters. *Academic Press, New York*, pp. 483.
- Friedrichs, C. T. (2010): Barotropic tides in channelized estuaries. In: Valle-Levinson, A. (2010): *Contemporary issues in estuarine physics*, Cambridge University Press, pp. 27–61.
- Geyer, W. R. & MacCready, P. (2014): The estuarine circulation. *Annual Review of Fluid Mechanics*, 46(1), pp. 175–197.
- Gisen, J. I. A., Savenije, H. H. G. & Nijzink, R. C. (2015): Revised predictive equations for salt intrusion modelling in estuaries. *Hydrology and Earth System Sciences*, 19, pp. 2791–2803.

- Gong, W., Wang, Y. & Jia, J. (2012): The effect of interacting downstream branches on saltwater intrusion in the Modaomen Estuary, China. *Journal of Asian Earth Sciences*, 45, pp. 223–238.
- Hansen, D. V. & Rattray, M. Jr. (1966): New dimensions in estuary classification. *Limnology and Oceanography*, 11(3), pp. 319–326.
- Hill, A. E., & Souza, A. J. (2006). Tidal dynamics in channels: 2. Complex channel networks. *Journal of Geophysical Research: Oceans (1978–2012)*, 111(C11).
- Ianniello, J. P. (1979): Tidally induced residual currents in estuaries of variable breadth and depth, *Journal of Physical Oceanography*, 9(5), pp. 962–974.
- Jay, D. A. & Musiak, J. D. (1994): Particle trapping in estuarine tidal flows. *Journal of Geophysical Research*, 99, pp. 445–461.
- Kalkwijk, J. P. T. & Booij, R. (1986): Adaptation of secondary flow in nearly-horizontal flow. *Journal of Hydraulic Research*, 24(1), pp. 19–37.
- Kleinhans, M. G., Jagers, H. R. A., Mosselman, E. & Sloff, C. J. (2008): Bifurcation dynamics and avulsion duration in meandering rivers by one-dimensional and three dimensional models. *Water Resources Research*, 44(8), pp. 1–31.
- Kleinhans, M. G., Ferguson, R. I., Lane, S. N. & Hardy, R. J. (2013): Splitting rivers at their seams: bifurcations and avulsion. *Earth Surface Processes and Landforms*, 38(1), 47–61.
- Kolmogorov, A. N. (1942). Equations of turbulent motion in an incompressible fluid. In: *Doklady Akademii Nauk SSSR*, Vol. 30, pp. 299–303.
- Lesser, G. R., Roelvink, J. A., Van Kester, J. A. T. M. & Stelling, G. S. (2004): Development and validation of a three-dimensional morphological model. *Coastal Engineering*, 51(8), pp. 883–915.
- Lewis, R. E., & Lewis, J. O. (1983): The principal factors contributing to the flux of salt in a narrow, partially stratified estuary, *Estuarine, Coastal and Shelf Science*, 16(6), pp. 599–626.
- MacCready, P. (1998): Estuarine adjustment to changes in river flow and tidal mixing. *Journal of Physical Oceanography*, 29(4), pp. 708–726.
- MacCready, P. (2004): Toward a unified theory of tidally-averaged estuarine salinity structure. *Estuaries*, 27(4), pp. 561–570.
- MacCready, P., & Geyer, W.R. (2010): Advances in estuarine physics. *Annual Review of Marine Science*, 2, pp. 35–58.
- McCarthy, R. K. (1993). Residual currents in tidally dominated, well-mixed estuaries. *Tellus*, 45A, pp. 325–340.
- Nepf, H. M. & Geyer, W. R. (1996): Intra-tidal variations in stratification and mixing in the Hudson Estuary. *Journal of Geophysical Research*, 101, pp. 12079–12086.
- Nguyen, A. D. & Savenije, H. H. G. (2006). Salt intrusion in multi-channel estuaries: A case study in the Mekong Delta, Vietnam. *Hydrology and Earth System Sciences*, 10, pp. 743–754.
- Nguyen, A. D., Savenije, H. H. G., Pham, D. N. & Tang, D. T. (2008): Using salt intrusion measurements to determine the freshwater discharge distribution over the branches of a multi-channel estuary: The Mekong Delta case. *Estuarine, Coastal and Shelf Science*, 77(3), pp. 433–445.
- Nguyen, A. D. (2008): Salt Intrusion, Tides and Mixing in Multi-Channel Estuaries: *PhD thesis: UNESCO-IHE Institute, Delft*. CRC Press, pp. 153.
- Nichols, M. M. & Biggs, R. B. (1985): Estuaries. In: *Coastal Sedimentary Environments* (Ed. R.A. Davis), Springer-Verlag, New York, pp. 77–186.
- Nunes, R. A. & Simpson, J. H. (1985): Axial convergence in a well-mixed estuary. *Estuarine, Coastal and Shelf Science*, 20, pp. 637–649.

- Prandle, D. (2004): Saline intrusion in partially mixed estuaries. *Estuarine, Coastal and Shelf Sciences*, 59(3), pp. 385–397.
- Prandle, D. (2009): Estuaries: dynamics, mixing, sedimentation and morphology. *Cambridge University Press*, pp. 248.
- Prandtl, L. (1945): Über ein neues Formelsystem für die ausgebildete Turbulenz. *Nachrichten von der Akademie der Wissenschaften in Göttingen. Mathematisch-Physikalische Klasse*, pp. 6–19.
- Pritchard, D. W. (1952a): Estuarine hydrography. *Advances in Geophysics*. 1, pp. 243–280.
- Pritchard, D. W. (1952b): Salinity distribution and circulation in the Chesapeake Bay Estuaries system. *Journal of Marine Research*, 11, pp. 106–123.
- Pritchard, D. W. (1955): Estuarine circulation patterns. *Proceedings of the American Society of Civil Engineers*, 81(717), pp. 1–11.
- Pritchard, D. W. (1958): The equations of mass continuity and salt continuity in estuaries. *Journal of Marine Research*, 17, pp. 412–423.
- Rigter, B. P. (1973): Minimum length of salt intrusion in estuaries. *Journal of the Hydraulic Division, Proceedings of ASCE* 99, pp. 1475–1496.
- Sassi, M. G., Hoitink, A. J. F., De Brye, B., Vermeulen, B. & Deleersnijder, E. (2011): Tidal impact on the division of river discharge over distributary channels in the Mahakam Delta. *Ocean Dynamics*, 61(12), pp. 2211–2228.
- Savenije, H. H. G. (1986). A one-dimensional model for salinity intrusion in alluvial estuaries. *Journal of Hydrology*, 85, pp. 87–109.
- Savenije, H. H. G. (1993). Predictive model for salt intrusion in estuaries. *Journal of Hydrology*, 148, pp. 203–218.
- Savenije, H. H. G. (2005). Salinity and Tides in Alluvial Estuaries. *Elsevier, New York*, pp. 194.
- Savenije, H. H. G. (2006): Comment on “A note on salt intrusion in funnel-shaped estuaries: Application to the Incomati estuary, Mozambique” by Brockway et al. (2005). *Estuarine, Coastal and Shelf Science*, 68(3), pp. 703–706.
- Savenije, H. H. G. (2012). Salinity and Tides in Alluvial Estuaries. *Elsevier, New York*, pp. 173. Second Completely Revised Edition (2012)
- Simpson, J. H., Brown, J., Matthews, J. & Allen, G. (1990): Tidal straining, density currents, and stirring in the control of estuarine stratification. *Estuaries*, 13, pp. 125–132.
- Simpson, J. H., Vennel, R. & Souza, A. J. (2001): The salt fluxes in a tidally-energetic estuary. *Estuarine, Coastal and Shelf Science*, 52, pp. 131–142.
- Smith, R. (1976): Longitudinal dispersion of a buoyant contaminant in a shallow channel. *Journal of Fluid Mechanics*, 78, pp. 677–88
- Stokes, G. G. (1847): On the theory of oscillatory waves. *Transactions of the Cambridge Philosophical Society*, 8, pp. 441–455.
- Thatcher, M. L. & Harleman, D. R. F. (1972): A mathematical model for the prediction of unsteady salinity intrusion in estuaries. Report no. 144, *MIT School of Engineering Massachusetts Institute of Technology, Department of Civil Engineering*, pp. 232.
- Uittenbogaard, R. E., Van Kester, J. A. T. M. and Stelling, G. S. (1992): Implementation of Three turbulence models in 3D-TRISULA for rectangular grids. *Technical Report Z81, WL/Delft Hydraulics*, Delft, The Netherlands, pp. 242.
- Uncles, R. J. & Jordan, M. B. (1979): Residual fluxes of water and salt at two stations in the Severn Estuary. *Estuarine Coastal and Marine Science*, 9, pp. 287–302.
- Uncles, R. J., & Lewis, R. E. (2001): The transport of fresh water from river to coastal zone through a temperate estuary. *Journal of Sea Research*, 46(2), pp. 161–175.
- Valle-Levinson, A. (2010): Definition and classification of estuaries. In: Valle-Levinson, A. (2010): *Contemporary issues in estuarine physics*, Cambridge University Press, pp. 1–11.



- Van Breemen, M. T. J. (2008): Salt intrusion in the Selangor estuary in Malaysia: model study with Delft3D. *MSc thesis Twente University*, The Netherlands, pp. 127.
- Van den Burgh, P. (1972). Ontwikkeling van een methode voor het voorspellen van zoutverdelingen in estuaria, kanalen en zeeën. *Rijkswaterstaat Rapport*, pp. 10–72 (Dutch).
- Van der Wegen, M. & Roelvink, J. A. (2008), Long-term morphodynamic evolution of a tidal embayment using a two-dimensional, process-based model, *Journal of Geophysical Research*, 113, pp. 1–23.
- Van Os, A. G. & Abraham, G. (1990): Density currents and salt intrusion. *Lecture Notes for the Hydraulic Engineering course at IHE-Delft, Delft Hydraulics*, Delft, The Netherlands, pp. 173.
- Van Veen, J. (1950): Ebb and flood channel systems in the Netherlands tidal waters. *Journal of the Royal Dutch Geographical Society (KNAG)*, 67, pp. 303–325 (in Dutch, English summary). Republished, translated and annotated by Delft University of Technology, 2001.
- Wang, Z. B., De Vries, M., Fokkink, R. J., & Langerak, A. (1995): Stability of river bifurcations in 1D morphodynamic models. *Journal of Hydraulic Research*, 33(6), pp. 739–750.
- West, J. R. & Williams, D. J. A. (1972): An evaluation of mixing in the Tay Estuary. In: *Proceedings of 13th Coastal Engineering Conference*, ASCE, Washington DC, pp. 2153–2169.
- Wu, H., Zhu, J., & Choi, B. H. (2010): Links between saltwater intrusion and subtidal circulation in the Changjiang Estuary: A model-guided study. *Continental Shelf Research*, 30(17), pp. 1891–1905.
- Zhang, E., Savenije, H. H. G., Wu, H., Kong, Y. & Zhu, J. (2011): Analytical solution for salt intrusion in the Yangtze Estuary, China. *Estuarine, Coastal and Shelf Science*, 91(4), 492–501.